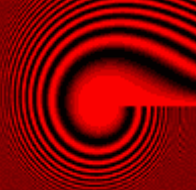
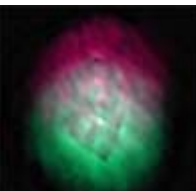
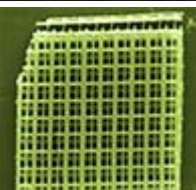
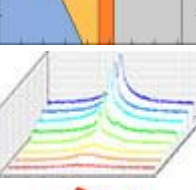
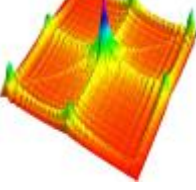


-  [Tuning field depth at high resolution by pupil engineering](#)
-  [Compressive tomography](#)
-  [Recent advances in holographic 3D particle tracking](#)
-  [Ultrafast laser processing of materials: a review](#)
-  [Optical vortex induction via light–matter...](#)
-  [Whispering gallery mode sensors: erratum](#)
-  [Laser feedback interferometry: a tutorial on the...](#)
-  [Recent advances in fundamentals and applications of random...](#)
-  [Transverse Anderson localization of light: a tutorial](#)

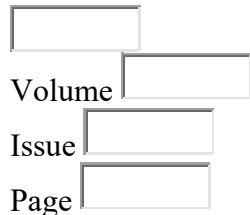
## Today's Top Downloads

1. [Optical methods for distance and displacement measurements](#)
2. [Structured-light 3D surface imaging: a tutorial](#)
3. [Cylindrical vector beams: from mathematical concepts to applications](#)
4. [Three-dimensional display technologies](#)
5. [Infrared fibers](#)

## Topics in Current Issue

- My Topics
- ([Login to access My Topics](#))
- [Imaging Systems](#) (2)
- [Microscopy](#) (1)
- [Ultrafast Optics](#) (1)

## Search this Journal



## [Submit a Paper](#)

## About this Journal

2014 Impact Factor:

10.111

Time to Publication:

152 days

---

ISSN:

1943-8206

Frequency:

Article-at-a-time publication; Quarterly issues

[Read more about this journal](#)

## Find Information For:

[Authors](#)

[Reviewers](#)

[Librarians](#)

**Topic Scope:** Coverage encompasses comprehensive review articles and multimedia tutorials appropriate for students, researchers, faculty, business professionals and engineers. Authoritative content covers advances in all areas of optics and photonics from fundamental science to engineering applications, including materials, devices, and systems. Submissions of long reviews and tutorials are invited only. Tutorials feature interactive components such as animation and video to maximize their reach.

# Advances in Optics and Photonics

## Tuning field depth at high resolution by pupil engineering

JORGE OJEDA-CASTAÑEDA<sup>1,\*</sup> AND CRISTINA M. GÓMEZ-SARABIA<sup>2</sup>

<sup>1</sup>Electronics Department, Engineering School, University of Guanajuato, Comunidad Palo Blanco, 36885 Salamanca, Gto., Mexico

<sup>2</sup>Digital Arts Department, Engineering School, University of Guanajuato, Comunidad Palo Blanco, 36885 Salamanca, Gto., Mexico

\*Corresponding author: jojedacas@ugto.mx

Received April 6, 2015; revised October 2, 2015; accepted October 5, 2015; published December 10, 2015  
(Doc. ID 237666)

We present a simple comprehensive treatment on the use of free-form optical elements, and of nonuniform optical windows, either for increasing focal depth [by regulating the width of the axial point spread function (PSF)] or for tuning the depth of field [by controlling the influence of focus error on the modulation transfer function (MTF)]. We employ the rising notation of pupil engineering, which incorporates techniques for controlling the spread of the axial PSF, as well as methods for governing the impact of focus errors on the MTF. Our discussion also includes the use of vortex lenses for designing nonconventional optical systems. © 2015 Optical Society of America

OCIS codes: (110.4850) Optical transfer functions; (110.4100) Modulation transfer function; (110.1758) Computational imaging; (110.6880) Three-dimensional image acquisition; (110.6915) Time imaging; (070.7425) Quasi-probability distribution functions

<http://dx.doi.org/10.1364/AOP.7.000814>

1. Introduction . . . . .	816
2. Engineering the Axial PSF . . . . .	817
2.1. Nonconventional Annularly Peaked Mask . . . . .	824
2.2. Quadratic Phase Delay in the $\zeta$ -Domain . . . . .	825
2.3. Moderate Axial Gaussian Apodizer . . . . .	826
2.4. Cubic Phase Delay in the $\zeta$ -Domain: Axial Bursts . . . . .	827
2.5. Dark Spot along the Optical Axis. . . . .	828
3. Influence of Focus Error on the OTF: Ambiguity Function . . . . .	830
4. Phase Conjugate Pairs. . . . .	846
4.1. Varifocal Lenses and Axial Scanners . . . . .	848
4.2. Quartic Phase Masks for a Tunable Cubic Phase Mask . . . . .	849
4.3. Tunable Sinusoidal Phase Mask . . . . .	850
4.4. Tunable Gaussian Mask . . . . .	852
4.5. Vortex Pairs: Phase Masks with Circular Symmetry . . . . .	855
5. Nonconventional Zoom Systems . . . . .	858
6. Conclusions . . . . .	863

Appendix A . . . . .	865
Appendix B . . . . .	866
Funding . . . . .	867
Acknowledgment . . . . .	867
References . . . . .	867

# Tuning field depth at high resolution by pupil engineering

JORGE OJEDA-CASTAÑEDA AND CRISTINA M. GÓMEZ-SARABIA

## 1. INTRODUCTION

Over the past three decades, many remarkable advances have been made for improving the quality of modern imaging devices. Indeed, there is a vigorous research trend of novel imaging systems that incorporate nonconventional free-form optical elements, nonuniform optical windows, and novel computing imaging techniques.

To describe some of the above achievements, we have made the following choices. We have decided to present a consistent technical analysis, based on scalar diffraction theory, rather than presenting a state-of-the-art technique for either digital recording or digital processing. Furthermore, aiming for a simple narrative, we use several schematic representations of optical systems and of phase-space descriptions. However, we have refrained of presenting sets of fancy digitally processed images.

We have selected, in chronological order, 99 papers that from our viewpoint have helped to conceptualize new schemes for acquiring images or for overcoming the classical limits on image quality [1–99]. Many of these papers are scattered in the technical literature, and several of them have not been incorporated into later publications that form part of our present review. We believe that this initial set of references will help readers to expand, or indeed to explore, other aspects of our current discussion. Needless to say, our current discussion relies heavily on our previous publications. For the sake of completeness of our presentation, many of these results are included here. However, we have reduced to a minimum reference duplications while still preserving citations in numerical order.

To build the proper scenario for our discussion, we cite classical publications describing tolerance criteria of image quality [100–103]. Then, we refer to contributions that challenge the *status quo* for designing imaging devices and for setting image quality criteria [48,93,104–122].

Before embarking on our technical discussion, we note that the various selected topics have not been identified with a single name. Indeed, to our knowledge, no attempts have been made toward relating and summarizing the various developments, when using free-form elements, as well as the use of nonuniform windows for gathering images, which will be later digitally processed for reducing the influence of focus error. For describing the use of nonuniform windows, the most commonly used notation is *optical apodization*. However, apodization was coined by Pierre Jaquinot for denoting the reduction of the sidelobes of the impulse response in optical spectroscopy [123–125]. As a secondary effect, the apodization masks broaden the central lobe of the point spread function (PSF). Some experts may not be aware of the following analogy. If one considers the axial PSF of an optical system, then reducing the sidelobes and widening the central lobe is useful for broadening the axial impulse response and, therefore, for extending focal depth [126–130].

Furthermore, it is still not so well known that there is a strong analogy between the use of masks that reduce the impact of focus error on the MTF [131–137] and the use of the ambiguity function and the Wigner distribution in image quality [138–144]. We

believe that these analogies may be useful for exchanging profitable information between different applications [145–157].

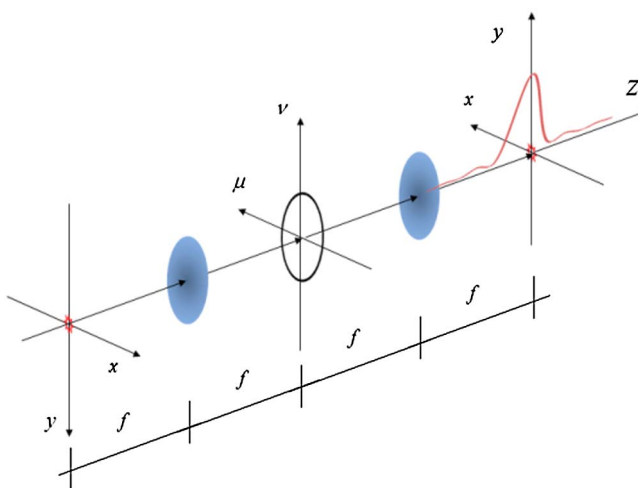
In what follows we present a simple, comprehensive treatment of the basic principles and some applications that describe the use free-form elements and nonuniform optical windows for reducing the influence of focus error, at full pupil aperture or, if you will, with high resolution. We employ the rising notation of pupil engineering, which is intended to incorporate previous notation, such as tailoring the PSF or shaping the MTF. As part of our discussion, we describe the use of a vortex pair, as varifocal lenses, for proposing novel, nonconventional optical systems.

To our end, in Section 2, we revisit the McCutchen theorem [158–176] for reducing sidelobes and for broadening the axial irradiance response. In Section 3, we link the evaluation of the out-of-focus optical transfer function (OTF) with the ambiguity function of the pupil aperture. We express the influence of focus error on the OTF as a Taylor series expansion. We employ symmetry arguments on the generalized pupil function for indicating that one can reduce by one-half the number of terms in the Taylor series expansion. In Section 4, we show that the symmetry considerations lead to the use of pairs of free-form refractive elements for implementing varifocal lenses. In this direction, the initial proposal can be traced back to the use of cylindrical lenses as suggested by Kitajima [177,178]. Improved versions for generating varifocal lenses were proposed simultaneously and independently by Lohmann [179–182] and by Alvarez [183–186]. We note that other authors have also described other applications when using this type of lens [187–192]. In Section 5, we discuss the use of a pair of vortex lenses for designing nonconventional optical systems. And in Section 6, we summarize our contribution.

## 2. ENGINEERING THE AXIAL PSF

In Fig. 1 we display the optical setup used for extending the axial irradiance distribution in an afocal optical system. If one uses scalar diffraction within the paraxial regime, one can evaluate the complex amplitude distribution of the 3D impulse response as follows:

**Figure 1**



Schematics of a telecentric optical system, which is used typically as an optical processor. At the Fraunhofer plane, one can place radially symmetric masks for spreading the irradiance distribution along the optical axis.

$$u(r, \theta, z) = \int_{\rho=0}^{\Omega} \int_{\varphi=0}^{2\pi} U(\rho, \varphi) \exp[-i\pi\lambda z\rho^2 + i2\pi r\rho \cos(\theta - \varphi)] \rho d\rho d\varphi. \quad (1)$$

In Eq. (1) we denote as  $(r, \theta, z)$  the cylindrical coordinates in the image space, in the pupil aperture we use polar coordinates  $(\rho, \varphi)$ , and the Cartesian coordinates in the pupil aperture are  $(\mu, \nu)$ . Hence,  $\rho = \sqrt{(\mu^2 + \nu^2)}$  is the radial spatial frequency. Its maximum value is the cut-off spatial frequency  $\Omega$ . Finally, we denote as  $U(\rho, \varphi)$  the complex amplitude transmittance over the pupil aperture.

By setting  $r = 0$  in Eq. (1), one can obtain the complex amplitude distribution along the optical axis or, if you will, the axial PSF:

$$u(0, \theta, z) = 2\pi \int_{\rho=0}^{\Omega} \left\{ \frac{1}{2\pi} \int_{\varphi=0}^{2\pi} U(\rho, \varphi) d\varphi \right\} \exp[-i\pi\lambda z\rho^2] \rho d\rho. \quad (2)$$

If one expresses the integral between curly brackets as an angular average, or zero-order circular harmonic  $\langle U(\rho) \rangle$ , then Eq. (2) becomes

$$u(0, \theta, z) = 2\pi \int_{\rho=0}^{\Omega} \langle U(\rho) \rangle \exp[-i\pi\lambda z\rho^2] \rho d\rho. \quad (3)$$

Now, it is convenient to rewrite Eq. (3) by using the following change of variables:

$$W = \frac{W_{2,0}}{\lambda} = -\frac{\lambda\Omega^2}{2}z; \quad q(W) = u(0, \theta, z). \quad (4a)$$

$$\zeta = \left( \frac{\rho}{\Omega} \right)^2 - \frac{1}{2}; \quad S(\zeta) = \langle U(\rho) \rangle = \frac{1}{2\pi} \int_{\varphi=0}^{2\pi} U(\rho, \varphi) d\varphi. \quad (4b)$$

In Eq. (4) we use as shorthand notation the letter  $W = W_{2,0}/\lambda$ , where  $W_{2,0}$  is the wavefront coefficient for focus error, and  $\lambda$  is the wavelength of the optical radiation. The change of variable in Eq. (4a) expresses a longitudinal displacement (along the optical axis) in terms of the wavefront aberration coefficient  $W_{2,0}$ . The angular average in Eq. (4b) is also known as the zero-order circular harmonic.

We also note that the change of variable in Eq. (4b) usefully describes a geometrical transformation for mapping the radial domain,  $0 \leq \rho \leq \Omega$ , into the dimensionless domain  $-1/2 \leq \zeta \leq 1/2$ . In Fig. 2 we illustrate the steps associated with the geometrical transformation in Eq. (4), which maps the circular function into the rectangular function. In addition, we note that the above mapping transforms a spherical wavefront into a plane wave; or, if you will, it transforms a lens into a prism. Other interesting cases are summarized in Table 1.

By substituting Eq. (4) into Eq. (3), one obtains the following remarkably simple, yet useful, result, which can be traced back to McCutchen, as was pointed out in the introduction. The axial complex amplitude distribution is proportional to the 1D Fourier transform of the pupil aperture  $S(\zeta)$ . That is,

$$s(W) = \pi\Omega^2 \int_{\zeta=-0.5}^{0.5} S(\zeta) \exp[i2\pi W\zeta] d\zeta. \quad (5)$$

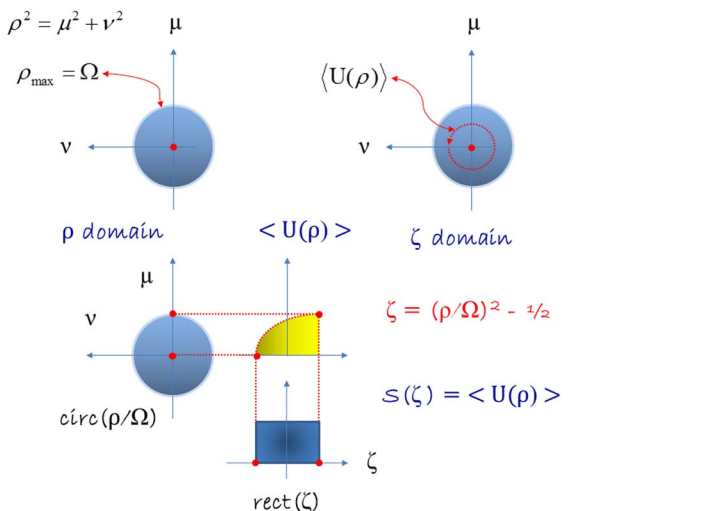
Hence, the Strehl ratio for focus errors is

$$I_s(W) = \frac{|s(W)|^2}{|s(0)|^2} = \frac{\left| \int_{-0.5}^{0.5} S(\zeta) \exp(i2\pi W\zeta) d\zeta \right|^2}{\left| \int_{-0.5}^{0.5} S(\zeta) d\zeta \right|^2}. \quad (6)$$

Some experts may not be aware of the following analogy. If one selects a mask  $S(\zeta)$ —from the set of classical apodizers that are used in spectroscopy—then the irradiance impulse response  $I_s(W)$  has a wide central lobe, and it has reduced secondary lobes. Therefore, we have suggested use of a classical apodizer in the  $\zeta$ -domain for generating in the  $\rho$ -domain radial masks,  $R(\rho)$ , which are able to expand the depth of focus by broadening the axial impulse response [126]. Later on, other authors used different conceptual frames for arriving at similar conclusions [193–196]. In Fig. 3 we illustrate the above remarkable result by describing the following ideally narrow, annular aperture:

$$U(\rho, \varphi) = \delta\left(\rho - \frac{\Omega}{\sqrt{2}}\right); \quad S(\zeta) = \delta(\zeta). \quad (7)$$

**Figure 2**



Pictographic description of an angular average operation on a pupil mask. After this operation, the resultant complex amplitude transmittance is the function  $\langle U(\rho) \rangle$ , which is known as the zero-order circular harmonic. It varies only with the radial variable, denoted as the  $\rho$ -domain. Next, we illustrate the geometrical transformation for mapping  $\langle U(\rho) \rangle$  into  $S(\zeta)$ . The support of  $S(\zeta)$  defines the  $\zeta$ -domain, where  $\zeta$  is a dimensionless variable.

**Table 1. Examples That Illustrate the Use of the Mapping in Eq. (4) to Relate Complex Amplitude Distributions in the  $\rho$ -Domain with Complex Amplitude Distributions in the  $\zeta$ -Domain**

$\rho$ -Domain	$\zeta$ -Domain
$R(\rho)$	$S(\zeta)$
circular aperture	rectangular aperture
narrow annular aperture	narrow slit
lens	prism
axial impulse response	Fourier transform of $S(\zeta)$
impact of spherical aberration	Fresnel transform of $S(\zeta)$

This ideal pupil aperture produces an axial impulse response that is equal to a constant. Hence, we obtained an infinitely extended focal depth. For proposing a physically viable description, in what follows we represent the Dirac delta in Eq. (7) as the superposition of a set of orthonormal functions.

This approach can be traced back to Frieden, who used a similar approach for describing superresolution [197]. Later on, one of us used the same mathematical model for proposing methods that extend the spread of the axial irradiance distribution [198,199].

To our end, we synthesize Dirac's delta in the  $\zeta$ -domain by using a finite number, say  $N$ , of functions that belong to a complete, orthonormal set of functions. See, for example, Appendix A. In mathematical terms,

$$\delta(\zeta) \approx \sum_{n=0}^N \Phi_n^*(0) \Phi_n(\zeta). \quad (8)$$

Of course, in the  $\rho$ -domain, the complex amplitude transmittance of the pupil mask is described by the radial function

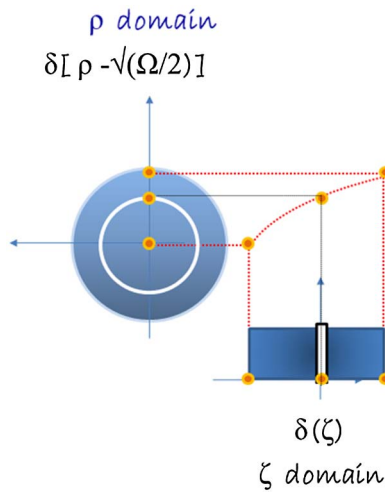
$$\delta\left(\rho - \frac{\Omega}{\sqrt{2}}\right) \approx \sum_{n=0}^N \Phi_n^*(0) \Phi_n\left[\left(\frac{\rho}{\Omega}\right)^2 - \left(\frac{1}{2}\right)\right]. \quad (9)$$

By substituting Eq. (8) into Eq. (9), we obtain

$$I_S(W) = \left| \sum_{n=0}^N \Phi_n^*(0) \int_{-0.5}^{0.5} \Phi_n(\zeta) \exp(i2\pi W\zeta) d\zeta \right|^2. \quad (10)$$

In what follows, we recognize that, for a given set of orthonormal functions (in the space domain), there is another set of orthonormal functions (in the frequency domain). Both set of orthonormal functions are related by a Fourier transform. In other words, these two sets of functions are Fourier transform pairs:

**Figure 3**



Visualization of the geometrical transformation in Eq. (4), for mapping a narrow annular aperture, in the  $\rho$ -domain, into a narrow slit in the  $\zeta$ -domain.

$$\varphi_n(W) = \int_{-0.5}^{0.5} \Phi_n(\zeta) \exp(i2\pi W\zeta) d\zeta. \quad (11)$$

Then, by using this result, the Strehl ratio versus focus error is

$$I_S(W) = \frac{\left| \sum_{n=0}^N \Phi_n^*(0) \varphi_n(W) \right|^2}{\left| \sum_{n=0}^N \Phi_n^*(0) \varphi_n(0) \right|^2}. \quad (12)$$

It is apparent from Eq. (12) that the normalized irradiance distribution along the optical axis can, in principle, be extended at will by increasing the number of terms  $N$ . In Fig. 4 we display this latter behavior, if  $\Phi_n(\mu)$  are the Chebyshev polynomials of the first kind and order  $m$ , and, consequently,  $\varphi_n(W)$  are the Bessel functions of the first kind and integer order  $m$ .

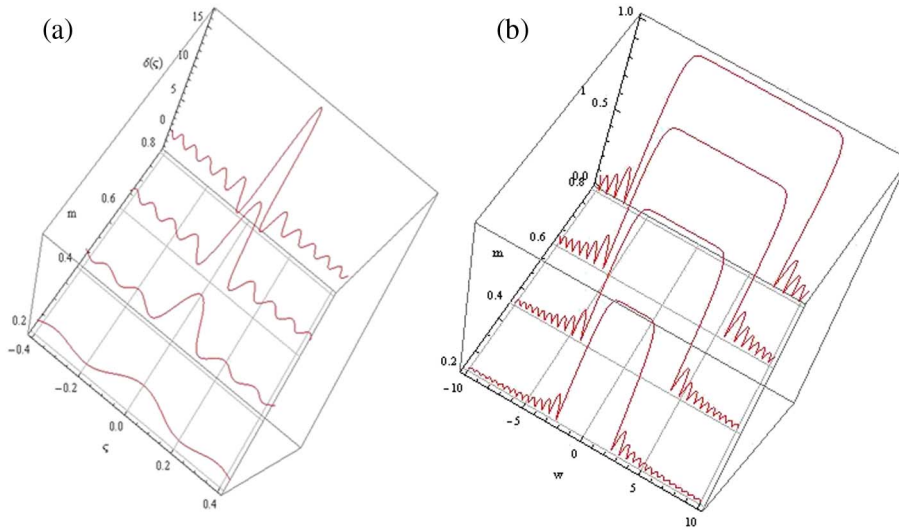
Here it is important to note that the geometrical transformation in Eq. (4b), and in Fig. 2, can be comprehensive for a large set of masks if the masks are properly scaled to fit either a reduced circular aperture or an annular (ring) aperture, as is depicted in Fig. 5. For these applications it is convenient to define a fill factor, which is here denoted as  $\varepsilon$ . This parameter is a real positive number such that  $0 < \varepsilon \leq 1$ . Next, for describing a mask that is scaled to cover a reduced version of the pupil aperture,  $0 \leq \rho \leq \varepsilon\Omega$ . As a first step, we set the cut-off radial frequency to the value  $\varepsilon\Omega$ , and then we note that the mapping from the  $\zeta$ -domain into the  $\rho$ -domain is

$$\rho = \sqrt{\left(\zeta + \frac{1}{2}\right)\varepsilon\Omega}; \quad -\frac{1}{2} \leq \zeta \leq \frac{1}{2}; \quad R(\rho) = S(\zeta), \quad (13a)$$

or, equivalently,

$$\zeta = \left(\frac{\rho}{\varepsilon\Omega}\right)^2 - \frac{1}{2}; \quad 0 \leq \rho \leq \varepsilon\Omega; \quad S(\zeta) = R(\rho). \quad (13b)$$

**Figure 4**



At the left-hand side we plot the changes of the complex amplitude transmittance, in the  $\zeta$ -domain, as one increases the number of Chebyshev polynomials in Eq. (12). At the right-hand side we plot the generated axial irradiance distributions, as one increases the number of Chebyshev polynomials.

Then, the Strehl ratio versus focus error becomes

$$I_{\text{closing}}(W; \varepsilon) = \frac{\left| \int_{-0.5}^{0.5} S(\zeta) \exp(i2\pi\varepsilon^2 W \zeta) d\zeta \right|^2}{\left| \int_{-0.5}^{0.5} S(\zeta) d\zeta \right|^2}. \quad (14)$$

Therefore, we claim that by reducing the pupil aperture, one preserves the functional relationship of the Strehl ratio. However, there is a scale variation. That is,

$$I_{\text{closing}}(W; \varepsilon) = I_S(\varepsilon^2 W). \quad (15)$$

In Eq. (15) the Strehl ratio for the full pupil aperture is  $I_S(W)$ . It is apparent from Eq. (15) that the tolerance to focus error is increased by the factor  $\varepsilon^2$ .

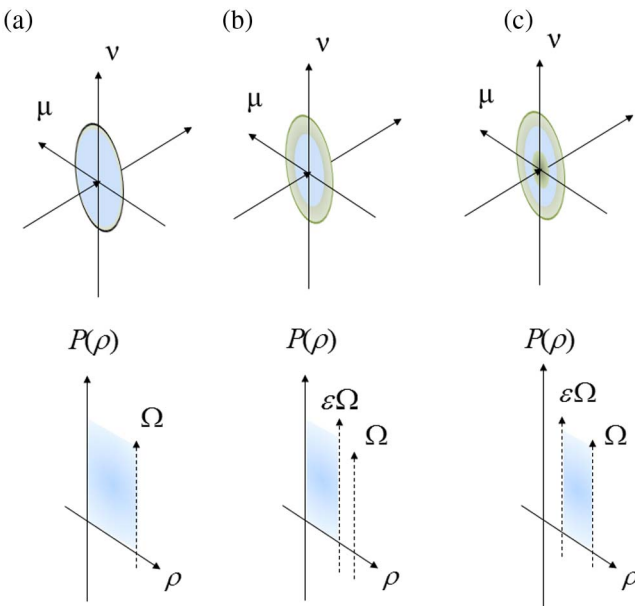
However, we note that by closing the pupil aperture, the light gathering power decreases by the same factor. These results are summarized in Table 2.

Next, for describing scaled versions of annularly distributed complex amplitude distributions, we recognize that the support of the pupil aperture is now  $\varepsilon\Omega \leq \rho \leq \Omega$ . Then, for mapping the  $\rho$ -domain into the  $\zeta$ -domain, we employ the geometrical transformation

$$\rho = \Omega \sqrt{\left(\zeta + \frac{1}{2}\right)(1 - \varepsilon^2) + \varepsilon^2}; \quad -\frac{1}{2} \leq \zeta \leq \frac{1}{2}; \quad R(\rho) = S(\zeta). \quad (16a)$$

or equivalently,

Figure 5



In Row 1, along three different columns, we depict three types of radially symmetric pupil mask. Along Row 2, in (a) we show the full circular aperture as a blue-shaded area. In (b) we portray a reduced circular aperture, and in (c) we depict a scaled annular aperture. These masks are treated as suitable scaled versions of the full pupil aperture.

$$\zeta = \frac{1}{1 - \varepsilon^2} \left[ \left( \frac{\rho}{\Omega} \right)^2 - \frac{1}{2} (1 + \varepsilon^2) \right]; \quad \varepsilon\Omega \leq \rho \leq \Omega; \quad S(\zeta) = R(\rho). \quad (16b)$$

The mapping in Eq. (16) scales usefully any given mask (taken from the  $\zeta$ -domain) into a 2D mask that fits the annular aperture. For these scaled versions, on annular apertures, the Strehl ratio versus focus error is

$$I_{\text{annular}}(W; \varepsilon) = \frac{\left| \int_{-0.5}^{0.5} S(\zeta) \exp(i2\pi(1 - \varepsilon^2)W\zeta) d\zeta \right|^2}{\left| \int_{-0.5}^{0.5} S(\zeta) d\zeta \right|^2}. \quad (17)$$

Thus, the versions fitting the annular apertures have a Strehl ratio versus focus error that is equal to

$$I_{\text{annular}}(W; \varepsilon) = I_S[(1 - \varepsilon^2)W]. \quad (18)$$

Again, in Eq. (18), the Strehl ratio for the full pupil aperture is  $I_s(W)$ .

It is clear from Eq. (18) that the Strehl ratio again preserves its functional relationship. However, there is a different scaling factor. One example suffices for illustrating rather well the above generic results. We analyze the use of the apodizer

$$S(\zeta) = (1 - 4\zeta^2)\text{rect}(\zeta). \quad (19)$$

In what follows, we scaled this apodizer to fit either circular apertures or annular apertures. In Fig. 6(a) we plot, in the  $\zeta$ -domain, the amplitude transmittance in Eq. (19). From Eqs. (4) and (19), we note that the circularly symmetric masks covering the full circular aperture have the following complex amplitude transmittance:

$$R(\rho) = 4 \left( \frac{\rho}{\Omega} \right)^2 \left[ 1 - \left( \frac{\rho}{\Omega} \right)^2 \right] \text{circ} \left( \frac{\rho}{\Omega} \right). \quad (20)$$

The amplitude transmittance in Eq. (20) is plotted in Fig. 6(b). Next, we employ Eqs. (13) and (19) to obtain the complex amplitude transmittances of the masks that fit the reduced versions of the circular aperture:

$$R(\rho) = 4 \left( \frac{\rho}{\varepsilon\Omega} \right)^2 \left[ 1 - \left( \frac{\rho}{\varepsilon\Omega} \right)^2 \right] \text{circ} \left( \frac{\rho}{\varepsilon\Omega} \right). \quad (21)$$

In Fig. 6(c) we plot the amplitude transmittance in Eq. (21) for  $\varepsilon = 0.9, 0.8, 0.7, 0.6$ , and 0.5. Finally, if we apply Eqs. (16) and (19), we identify the complex amplitude transmittances of the annularly distributed masks that fit ring apertures:

$$R(\rho) = \left( \frac{2}{1 - \varepsilon^2} \right)^2 \left[ \left( \frac{\rho}{\Omega} \right)^2 - \varepsilon^2 \right] \left[ 1 - \left( \frac{\rho}{\Omega} \right)^2 \right] \left[ \text{circ} \left( \frac{\rho}{\Omega} \right) - \text{circ} \left( \frac{\rho}{\varepsilon\Omega} \right) \right]. \quad (22)$$

In Fig. 6(d) we plot the amplitude transmittance in Eq. (22) if the obscuration ratio is  $\varepsilon = 0.1, 0.2, 0.3, 0.4$ , and 0.5.

**Table 2. Comparisons of the Variations of the Light Gathering Power and of the Strehl Ratio, in Terms of the Fill Factor  $\varepsilon^a$**

$0 < \varepsilon \leq 1$	Light-Gathering Power $T(\varepsilon)$	Strehl Ratio Versus Focus Errors
Clear pupil $0 \leq \rho \leq \Omega$	$T = 1$	$I(W) = \text{sinc}^2(W)$
Closing down $0 \leq \rho \leq \varepsilon\Omega$	$T_{\text{closing}}(\varepsilon) = \varepsilon^2$	$I_{\text{closing}}(W; \varepsilon) = \text{sinc}^2(\varepsilon^2 W)$
Annular aperture $\varepsilon\Omega \leq \rho \leq \Omega$	$T_{\text{annular}}(\varepsilon) = 1 - \varepsilon^2$	$I_{\text{annular}}(W; \varepsilon) = \text{sinc}^2((1 - \varepsilon^2)W)$

<sup>a</sup>This parameter scales suitably the cut-off spatial frequency  $\Omega$ .

The axial irradiance distribution for the masks in Fig. 6 is related to the Fourier transform of Eq. (19); that is,

$$I_S(W) = \int_{-\infty}^{\infty} (1 - 4\zeta^2)\text{rect}(\zeta) \exp(i2\pi W\zeta) d\zeta = \left(\frac{2}{\pi^2 W^2}\right)^2 [\text{sinc}(W) - \cos(\pi W)]^2. \quad (23)$$

Consequently, by fitting the apodizer in the reduced pupil aperture, the Strehl ratio becomes

$$I_{\text{closing}}(W) = \left(\frac{2}{\pi^2 \epsilon^2 W^2}\right)^2 [\text{sinc}(\epsilon^2 W) - \cos(\pi \epsilon^2 W)]^2. \quad (24)$$

Furthermore, by fitting the apodizer in annular apertures, the Strehl ratio is

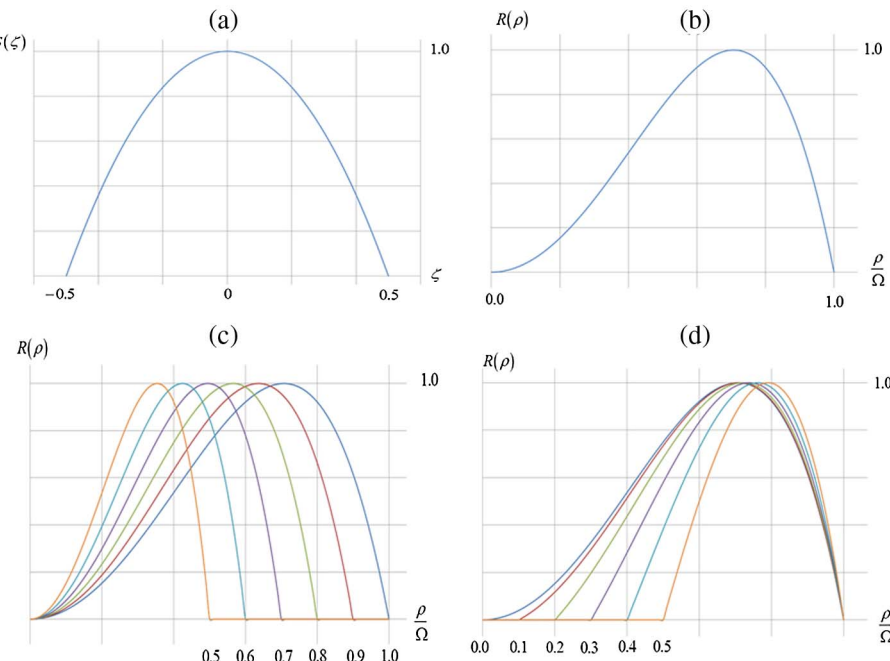
$$I_{\text{annular}}(W) = \left(\frac{2}{\pi^2 (1 - \epsilon^2) W^2}\right)^2 [\text{sinc}((1 - \epsilon^2) W) - \cos(\pi(1 - \epsilon^2) W)]^2. \quad (25)$$

In Fig. 7 we plot the results in Eqs. (23), (24), and (25) for several values of  $\epsilon$ . The simple cases of transparent circles and transparent rings have been summarized already in Table 2. Next, before ending this section, it is relevant to discuss some particularly insightful examples.

### 2.1. Nonconventional Annularly Peaked Mask

For our first example, we propose the use of the following nonconventional narrow annular mask. In the  $\rho$ -domain, that amplitude transmittance is

**Figure 6**



Variations of the amplitude transmittance, as one changes the fill factor  $\epsilon$ . (a) The initial amplitude transmittance in the  $\zeta$ -domain. (b) The amplitude transmittance inside a full pupil aperture. (c) The amplitude transmittances when fitting reduced circular apertures. (d) The amplitude transmittances when fitting reduced annular apertures.

$$R(\rho) = \exp \left\{ -10 \left| 2 \left( \frac{\rho}{\Omega} \right)^2 - 1 \right|^{0.25} \right\} \text{circ} \left( \frac{\rho}{\Omega} \right). \quad (26a)$$

At the top of Fig. 8, we plot the complex amplitude distribution in the  $\zeta$ -domain:

$$S(\zeta) = \exp \{-10|2\zeta|^{0.25}\} \text{rect}(\zeta). \quad (26b)$$

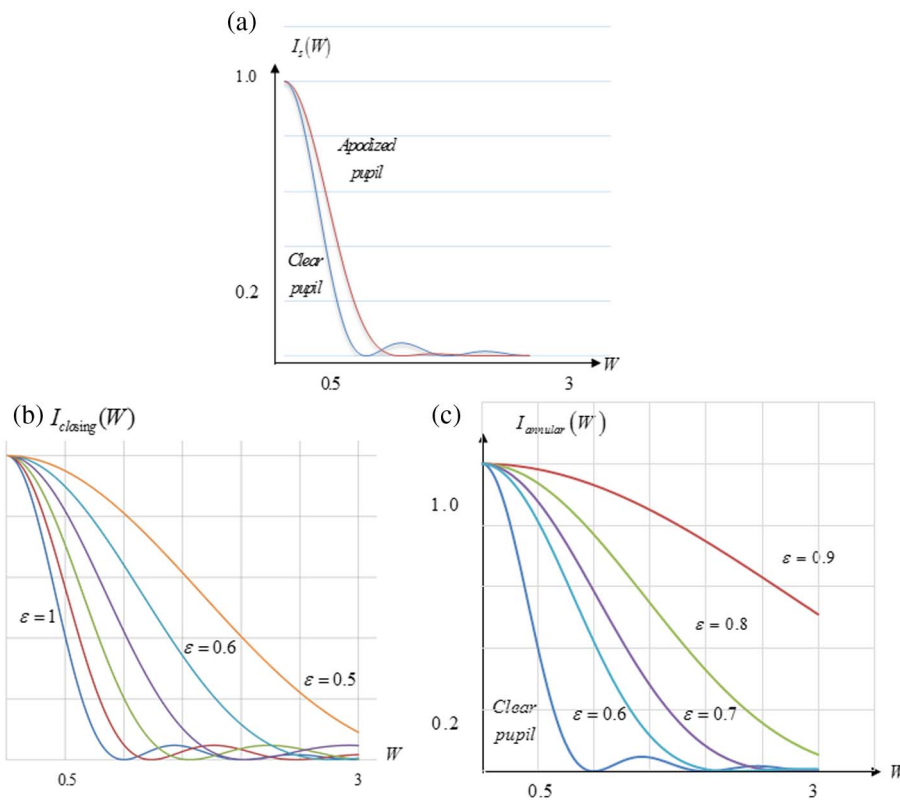
By evaluating numerically its Fourier transform, and later on by taking the square modulus of this Fourier transformation, we obtain the axial irradiance distribution that is depicted at the bottom of Fig. 8. It is apparent from Fig. 8 that, by using the annularly distributed amplitude mask in Eq. (26a), the axial irradiance distribution has a strong peak at the focal plane. Outside the central peak, the axial irradiance distribution decreases slowly as a monotonic function.

## 2.2. Quadratic Phase Delay in the $\zeta$ -Domain

For our second example, we analyze the use of a radial mask that is able to generate an irradiance distribution similar to the Fresnel diffraction pattern of a slit. In the  $\zeta$ -domain, the proposed mask introduces a phase delay to the second power.

In mathematical terms, at the pupil aperture we place a radially symmetric mask, whose complex amplitude distribution is

Figure 7



Graphs depicting the variations of the Strehl ratio versus focus error for the masks in Fig. 6, for certain values of the fill factor  $\varepsilon$ . In (a) we describe a comparison between the full clear circular aperture and an apodized circular aperture. In (b) we plot the variations for scaled circular apertures. In (c) we plot the variations for scaled annular apertures.

$$R(\rho) = \exp\left\{i2\pi B\left[2\left(\frac{\rho}{\Omega}\right)^2 - 1\right]^2\right\} \text{circ}\left(\frac{\rho}{\Omega}\right). \quad (27a)$$

Then, in the  $\zeta$ -domain the complex amplitude distribution is

$$S(\zeta) = \exp\{i2\pi B(2\zeta)^2\}. \quad (27b)$$

In Fig. 9, we plot the normalized axial irradiance distribution if the optical path difference is  $B = 10$ , in units of wavelengths. As one should expect, the Strehl ratio versus focus error is similar to the near-field diffraction pattern generated by a rectangular window. Consequently, the normalized axial irradiance distribution exhibits spurious oscillations. In what follows we show that one can reduce these spurious oscillations by placing a moderate absorbing Gaussian mask on the top of the phase mask in Eq. (27a).

### 2.3. Moderate Axial Gaussian Apodizer

For our third example, we discuss the use of a moderate Gaussian attenuation, in the  $\zeta$ -domain, which is placed on the top of the phase mask in Eq. (27a).

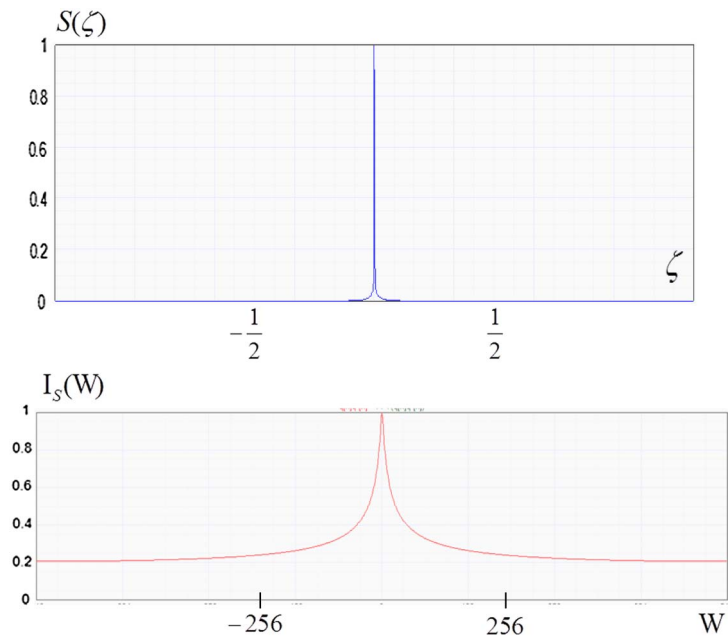
At the bottom, we plot the Strehl ratio versus focus error that one obtains when using this mask.

In the  $\rho$ -domain, the proposed radially symmetric mask has the following complex amplitude transmittance:

$$R(\rho) = \exp\left\{i2\pi B\left[2\left(\frac{\rho}{\Omega}\right)^2 - 1\right]^2\right\} \exp\left\{-c\left[2\left(\frac{\rho}{\Omega}\right)^2 - 1\right]^2\right\} \text{circ}\left(\frac{\rho}{\Omega}\right). \quad (28a)$$

At the top of Fig. 10, we plot the complex amplitude transmittance in the  $\zeta$ -domain:

**Figure 8**



Nonconventional amplitude transmittance, in the  $\zeta$ -domain, of a mask that is used for designing an annular apodizer ( $\rho$ -domain), which is able to generate a monotonically decreasing peaked axial irradiance distribution.

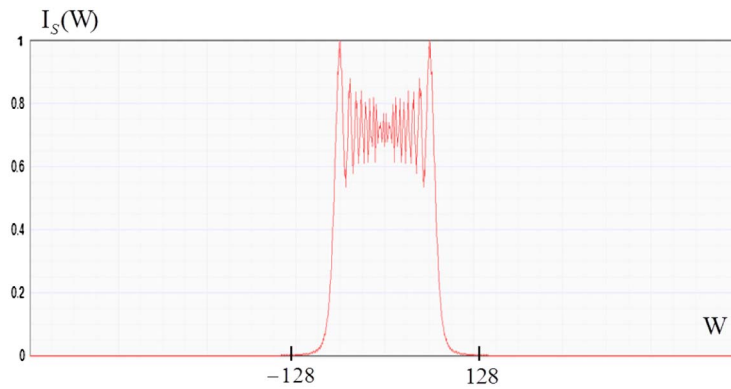
$$S(\zeta) = \exp\{i2\pi B(2\zeta)^2\} \exp\{-4c\zeta^2\} \text{rect}(\zeta). \quad (28b)$$

As depicted at the bottom of Fig. 10, the Strehl ratio versus focus error has now a Gaussian envelope, which exhibits local amplitude variations.

#### 2.4. Cubic Phase Delay in the $\zeta$ -Domain: Axial Bursts

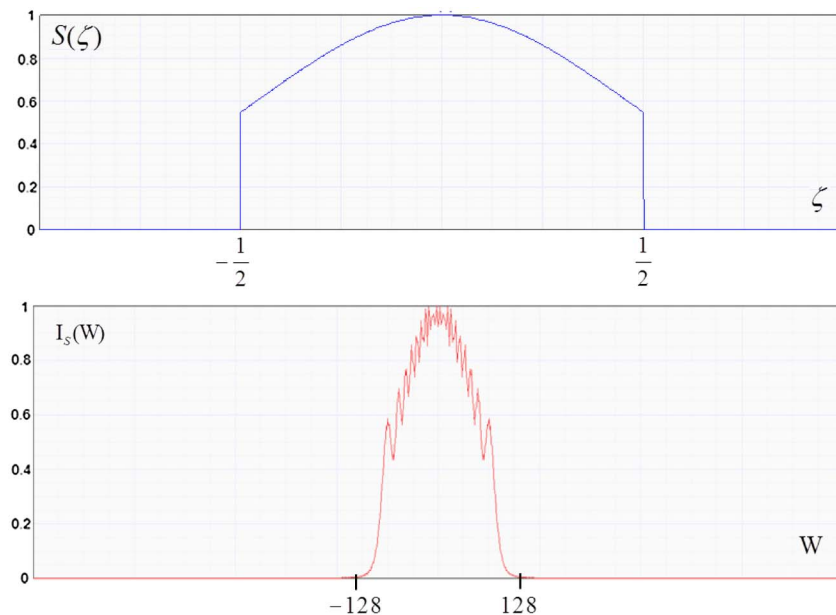
An interesting variant of the previous results is depicted in Fig. 11. Here the normalized axial irradiance distribution has an asymmetrical profile, which is denoted as an axial burst [200,201].

Figure 9



Strehl ratio versus focus error that is similar to the irradiance distribution of the Fresnel diffraction pattern of a slit. This axial irradiance distribution is generated by using the radially symmetric phase mask in Eq. (27a) with an optical path difference of 10 wavelengths.

Figure 10



At the top we display the amplitude transmittance of a moderate Gaussian apodizer in the  $\zeta$ -domain. In Eq. (28a) we describe the amplitude transmittance of the related radial mask.

It is relevant to note that the axial asymmetrical behavior shown in Fig. 11 is caused by the radially symmetric complex amplitude distribution:

$$R(\rho) = \exp \left\{ i2\pi B \operatorname{sgn} \left[ 2 \left( \frac{\rho}{\Omega} \right)^2 - 1 \right] \left| 2 \left( \frac{\rho}{\Omega} \right)^2 - 1 \right|^3 \right\} \exp \left\{ -a \left| 2 \left( \frac{\rho}{\Omega} \right)^2 - 1 \right|^3 \right\} \operatorname{circ} \left( \frac{\rho}{\Omega} \right). \quad (29a)$$

In the  $\zeta$ -domain, the complex amplitude transmittance is

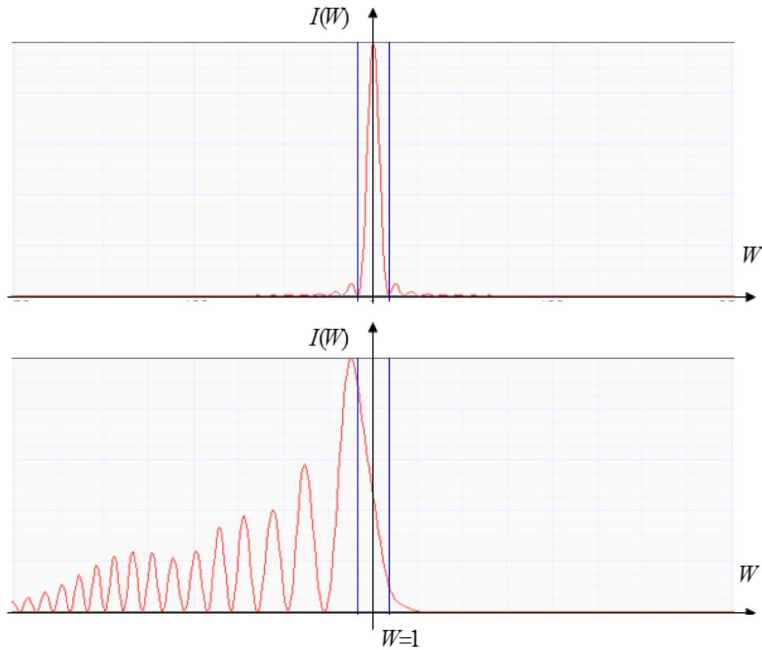
$$S(\zeta) = \exp \{ i2\pi B \operatorname{sgn}(\zeta) |2\zeta|^3 \} \exp \{ -a |2\zeta|^3 \} \operatorname{rect}(\zeta). \quad (29b)$$

At the top of Fig. 11, we plot the axial irradiance distribution of a clear circular aperture. At the bottom of Fig. 11, we plot the axial irradiance distribution associated to an axial burst, which is obtained with the mask in Eq. (29b) for the values  $B = 4$  and  $a = 0.5$ .

### 2.5. Dark Spot along the Optical Axis

Last, but not least, as our fifth example, we consider the use of pupil masks that have spiral or helical variations [202]. This type of pupil mask is characterized for having a zero-order circular harmonic that is equal to zero. Thus, these masks are able to sustain a dark central spot along the optical axis. This kind of irradiance distribution may be useful for optical alignment and for other nonconventional optical techniques [203–218]. For these masks, the overall complex amplitude transmittance is different from zero, but its angular average, as discussed in Eq. (4b), is equal to zero for any value of  $\rho$ . That is,

**Figure 11**



Graphical comparison, at the same scale, of two axial irradiance distributions. At the top, we display the irradiance distribution of a clear pupil aperture. At the bottom, we show the axial irradiance bursts that are caused by the use of the radially symmetric mask in Eq. (29).

$$\langle U(\rho) \rangle = \frac{1}{2\pi} \int_{\varphi=0}^{2\pi} U(\rho, \varphi) d\varphi = 0. \quad (30)$$

This interesting condition implies that the axial irradiance distribution is equal to zero. Hence, the PSF is able to sustain a dark spot along the optical axis. Here we illustrate with two simple examples the unique condition in Eq. (30). For generating helical beams, it is common to use the following complex amplitude transmittance:

$$U(\rho, \varphi) = \exp(i a \varphi). \quad (31)$$

For our first example, in Fig. 12(a) we show the interference pattern between a uniform plane wave, as a reference beam, and the complex amplitude distribution in Eq. (31). This type of interference pattern was analyzed first by Bryngdahl [219] and later by Fürhapter *et al.* [220]. For the second example, the reference beam is a binary zone plate that has binary helical variations or, if you will, phase-daisy variations.

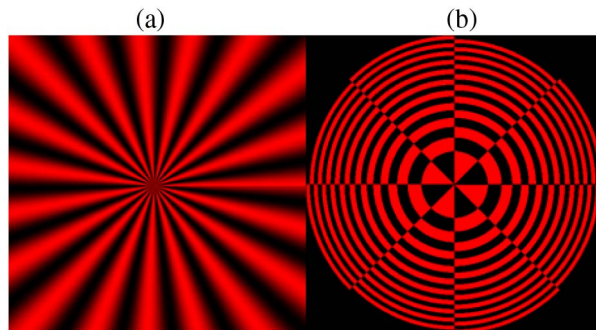
In Fig. 12(b) we show that the interferogram is a zone plate. The reference beam is a plane wave, but the probe beam has the following complex amplitude variations:

$$U(\rho, \varphi) = \sum_{m=-\infty}^{\infty} C_m \left[ 1 - 2 \sum_{n=0}^{N-1} \text{rect}\left(\frac{\varphi - (2n+1)\frac{\pi}{N}}{\frac{\pi}{N}}\right) \right] \exp\left\{i2\pi\frac{\rho^2}{\Omega^2}m\right\} \text{circ}\left(\frac{\rho}{\Omega}\right). \quad (32)$$

It is straightforward to verify that the complex amplitude transmittance in Eqs. (31) and (32) fulfill the condition in Eq. (30). Hence, these masks are able to sustain a dark spot along the optical axis. Now, we note that for generating Fresnel–Soret zone plates with variable foci, Lohmann [221], Rogers and Rogers [222], and Burch and Williams [223] suggested encoding the classical quadratic phase with helical variations.

By following Lohmann's proposal, one can obtain interferograms such as the one depicted in Fig. 13(b). Lohmann and Paris have suggested performing an angular average (on this type of interferogram) for generating a varifocal zone plate with radial symmetry [224]. Next, we follow a closely related approach for generating a series of interferograms that have both helical variations and radial phase variations of the form  $(\rho/\Omega)^m$ . In Fig. 13 we show the interferograms that are obtained by the interference of

**Figure 12**



Irradiance distributions associated with two different interferograms. In each interferogram, the reference beam is a plane wavefront. In (a) the probe beam is a helical beam with continuous phase variations. In (b) the probe beam is a spherical wavefront, which has helical binary phase transitions.

a plane wave (as the reference beam) and an object beam that has the following complex amplitude distribution:

$$U_m(\rho, \varphi) = \exp \left\{ i2\pi a \left( \frac{\rho}{\Omega} \right)^m \varphi \right\}. \quad (33)$$

All the members of this family set satisfy the condition  $\langle U_m(\rho, \varphi) \rangle = 0$ . Hence, these complex amplitude distributions display a dark spot along the optical axis. In Fig. 13(a) we set  $m = 1$  for an axicon, in Fig. 13(b) we set  $m = 2$  for a lens, and in Fig. 13(c) we set  $m = 3$  for a cubic radial phase variation, like the one discussed in Eq. (29), for generating axial bursts. In Section 5, we form pairs of these complex amplitude distributions for setting tunable focalizers. However, before that we consider the following situation. If one employs an optical system for gathering images of extended objects (rather than assessing the optical system by using the axial irradiance distribution), one is interested in optical methods that are able to govern the impact of focus error on the OTF.

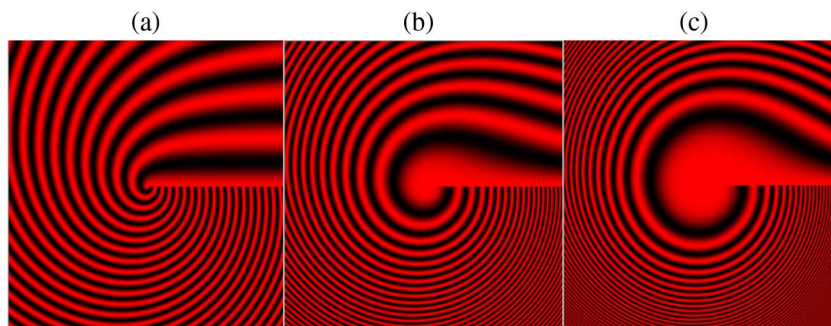
### 3. INFLUENCE OF FOCUS ERROR ON THE OTF: AMBIGUITY FUNCTION

There are several optical methods for increasing the depth of field of an optical system that gathers pictures of extended objects under noncoherent illumination. These methods have disrupted the image quality chain, as is depicted in Fig. 14.

These methods are two-stage techniques. In the first stage, the optical system records pictures while employing a preprocessing mask, which reduces the impact of focus error on the MTF. Hence, the preprocessing masks ensure that several planar scenes, located at different depths of the object field, suffer from virtually the same amount of contrast reduction, but the MTF does not have zero values inside the passband. At the second stage, image contrast can be corrected simultaneously for all different field depths.

The above procedure can be traced back to Haeusler, who showed the usefulness of superimposing several images in the same photographic plate while moving the optical system [225]. Mino and Okano are to be credited for analyzing several amplitude masks that weakened the influence of focus errors on the MTF [226]. Some of us have proposed taking a single snapshot while using an amplitude mask (apodizer) that suitably reduces equally the contrast of objects located at different depths of field. Since the MTF has no zero values inside its passband, and it has only reduced values

**Figure 13**



Irradiance distributions generated by using a two-beam interferometer. In the three depicted cases, the reference beam is a plane wave, and the probe beam has the complex amplitude variations in Eq. (33) for (a)  $m = 1$ , (b)  $m = 2$ , and (c)  $m = 3$ .

(as compared with the in-focus MTF), then in a lax manner, one can say that image quality has been distributed “democratically” among the different planes composing a 3D scene. Hence, by applying simple digital inversion techniques, one can recover simultaneously the contrast of different input planes [104].

The requirements for the preprocessing mask are the following. The mask should generate a MTF with low sensitivity to focus error. This generated MTF should not have zero values inside its passband. For designing this type of mask, it was suggested to employ the ambiguity function as a suitable mathematical tool [227]. Of course, since the Wigner distribution function is the double Fourier transform of the ambiguity function, then the results obtained using the ambiguity function can be worded in terms of the Wigner distribution function. It was early recognized that optical technology may allow for producing nonconventional masks, and that there were several digital algorithms for postprocessing.

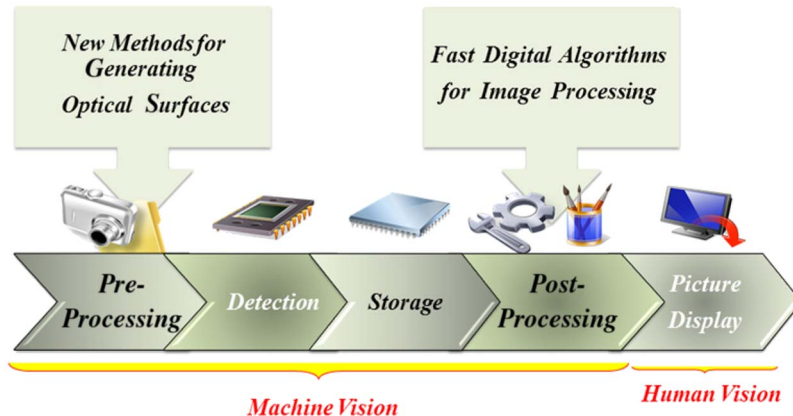
Dowski and Cathey should be duly credited by introducing into optics the cubic phase mask [228], which was known already in the radar community [229].

The cubic phase mask has the advantage, over previously described amplitude masks, that it preserves light-gathering power. However, the cubic phase masks introduce spurious oscillation in the MTF, which can be attenuated by using moderate absorbing amplitude masks, as is suggested in Ref. [230].

In Fig. 15, we show the influence of focus error on an image of Lena when gathering pictures with different masks, and different values of focus error. The results in Fig. 15 are complemented by the images in Figs 16 and 17. In these latter figures, we also display the influence of focus error when gathering pictures with different masks and different values of focus error. In Fig. 16 we display the variations on the MTF; in Fig. 17 we display the variations on the PSF.

It is important to note that, along the columns of Figs. 15, 16, and 17, the focus error coefficient varies from zero to  $3\lambda$ , in steps of  $\lambda/2$ . Along the rows of Figs. 15, 16 and 17, we show the following variations. Along Row 1, we consider an optical system with a clear pupil aperture. Along Row 2, the pupil aperture is covered with an amplitude mask that has moderate Gaussian amplitude variations. Along Row 3, the pupil has a 2D cubic phase mask. Finally, in Row 4, the pupil has both an amplitude mask with moderate Gaussian variations and a 2D cubic phase mask.

**Figure 14**



Pictorial of the image quality chain associated with the two-stage process (preprocessing and postprocessing) for extending the depth of field of an optical system.

From Row 3 of Fig. 16, it is apparent that the cubic mask reduces the impact of focus error on the MTF. The in-focus MTF as well as the out-of-focus MTF have nonzero values inside a region that resembles a four-point star.

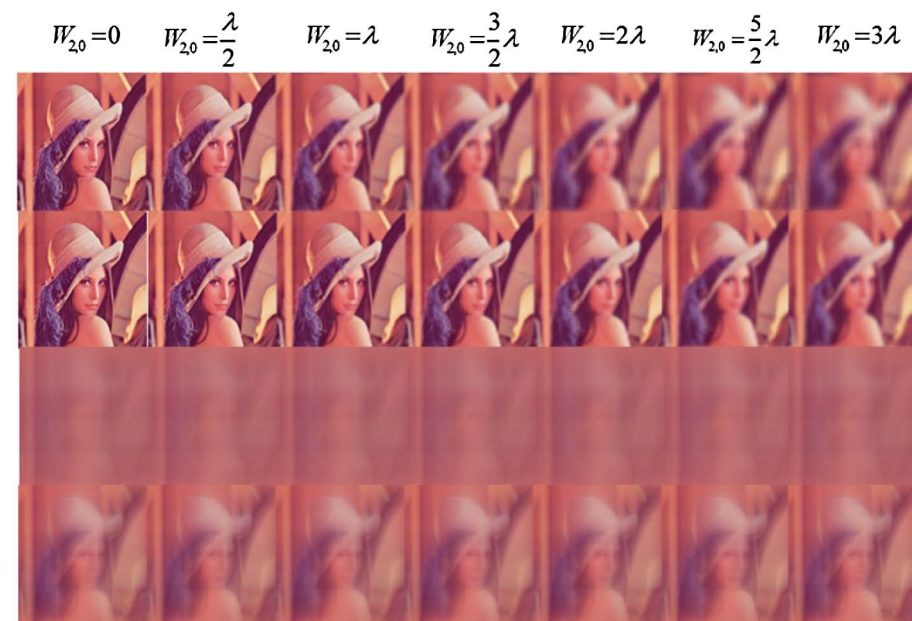
Furthermore, the values of the MTF have low values outside the Cartesian axis. From Row 4 of Fig. 16, we observe that by adding a moderate attenuation mask with a Gaussian profile, the values of the MTF are extended outside the Cartesian axis. This last feature is helpful for avoiding the reduction in contrast, as was already apparent from the comparisons between the images in the last two rows of Fig. 15.

The results in Fig. 17 help us to assess further the advantages of employing a moderate attenuation filter when using the cubic phase mask. From a simple comparison between the images in the last two rows of Fig. 17, we observe that a moderate attenuation mask (with Gaussian profile) also helps to reduce the spread of the 2D PSF.

Dowski and Cathey denoted the pre-processing operation as “encoding,” and the post-processing operation as “decoding.” Their notation follows Haeusler’s proposal, since both notations mimic the usage of the well-known two-step process in optical holography. Perhaps this is not the best notation. However, curiously enough, this wording has inspired further research.

In what follows we review the above described ideas, by noting that in several branches of applied optics, it is convenient to employ local frequencies, or phase-space representations [231–234]. We start by discussing a simple manner for representing the optical characteristics of a 1D pupil mask in phase space. For our

**Figure 15**

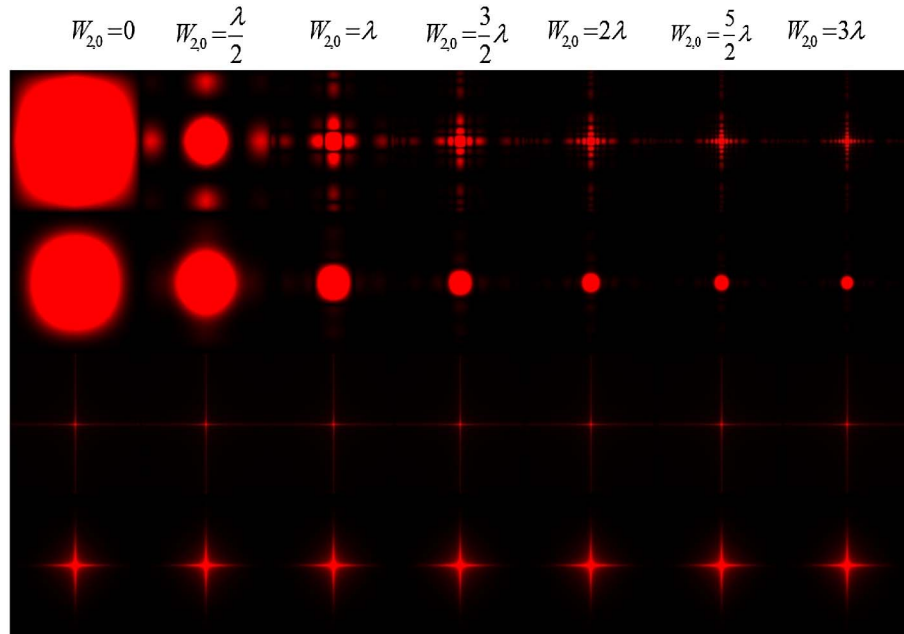


Array of pictures for displaying the variations in image quality, with variable focus error. As is indicated at the top of this figure, along the columns, the focus error coefficient varies in steps of  $\lambda/2$ . Along the rows, we show the use of four different pupil masks that help to reduce the influence of focus error on the MTF.

discussion, we denote as  $Q(\mu)$  the complex amplitude transmittance of a pupil mask. Hence, the pupil mask generates the coherent PSF:

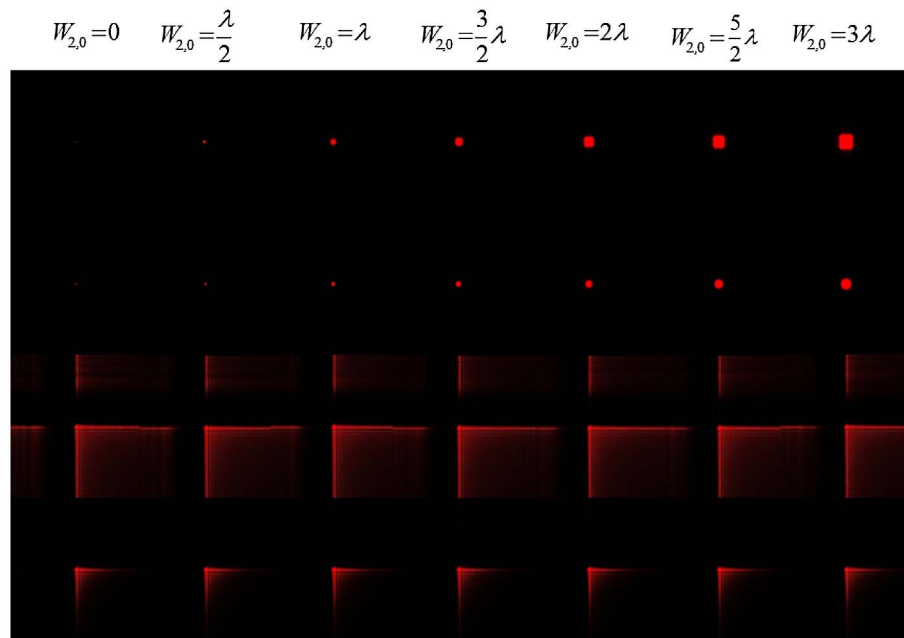
$$q(x) = \int_{-\infty}^{\infty} Q(\mu) \exp\{i2\pi x\mu\} d\mu. \quad (34)$$

Figure 16



Array of pictures displaying the variations of the MTF with variable focus error, when using the same pupil masks that are used in Fig. 15. Along the columns, the focus error coefficient varies in steps of  $\lambda/2$ .

Figure 17



Array of pictures displaying the variations of the irradiance PSF with variable focus error, for the same pupil masks that are used for obtaining the results in Fig. 16.

Next, we define the product spectrum of the pupil mask as

$$P(\mu, \nu) = Q\left(\nu + \frac{\mu}{2}\right)Q^*\left(\nu - \frac{\mu}{2}\right). \quad (35)$$

If one uses the inverse relationship of Eq. (34) in Eq. (35), one obtains that

$$P(\mu, \nu) = \int_{-\infty}^{\infty} q(t) \exp\left\{-i2\pi\left(\nu + \frac{\mu}{2}\right)t\right\} dt \int_{-\infty}^{\infty} q^*(s) \exp\left\{i2\pi\left(\nu - \frac{\mu}{2}\right)s\right\} ds. \quad (36)$$

By assuming that there is a 2D optical mask whose amplitude transmittance is equal to  $P(\mu, \nu)$ , in Eq. (35), then its Fraunhofer diffraction pattern has the following complex amplitude distribution:

$$p(x, y) = \int_{-\infty}^{\infty} \int_{-\infty}^{\infty} P(\mu, \nu) \exp\{i2\pi(x\mu + y\nu)\} d\mu d\nu. \quad (37)$$

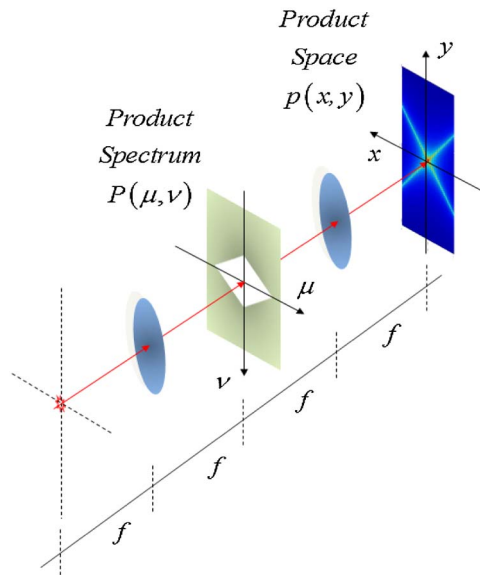
By substituting Eq. (36) into Eq. (37), it is straightforward to show that the 2D Fourier transform of the product spectrum is the product space:

$$p(x, y) = q\left(x + \frac{y}{2}\right)q^*\left(x - \frac{y}{2}\right). \quad (38)$$

As indicated in Fig. 18, we note that the product spectrum of the pupil mask and the product space of the coherent PSF are Fourier pairs.

Next we note that, on the one hand, the Wigner distribution function of  $Q(\mu)$ , or equivalently the Wigner distribution function of  $q(x)$ , is

**Figure 18**



Schematics of a classical optical processor used for displaying the product space as the Fraunhofer diffraction pattern of the product spectrum in Eq. (35).

$$\begin{aligned}
 F(x, \nu) &= \int_{-\infty}^{\infty} P(\mu, \nu) \exp\{i2\pi x\mu\} d\mu \\
 &= \int_{-\infty}^{\infty} Q\left(\nu + \frac{\mu}{2}\right) Q^*\left(\nu - \frac{\mu}{2}\right) \exp\{i2\pi x\mu\} d\mu \\
 &= \int_{-\infty}^{\infty} p(x, y) \exp\{-i2\pi\nu y\} dy \\
 &= \int_{-\infty}^{\infty} q\left(x + \frac{y}{2}\right) q^*\left(x - \frac{y}{2}\right) \exp\{-i2\pi\nu y\} dy. \tag{39}
 \end{aligned}$$

It has been noted that the mathematical operations in Eq. (39) can be implemented optically by employing anamorphic optical processors, such as those depicted in Fig. 19, which are discussed extensively in Refs. [235–239].

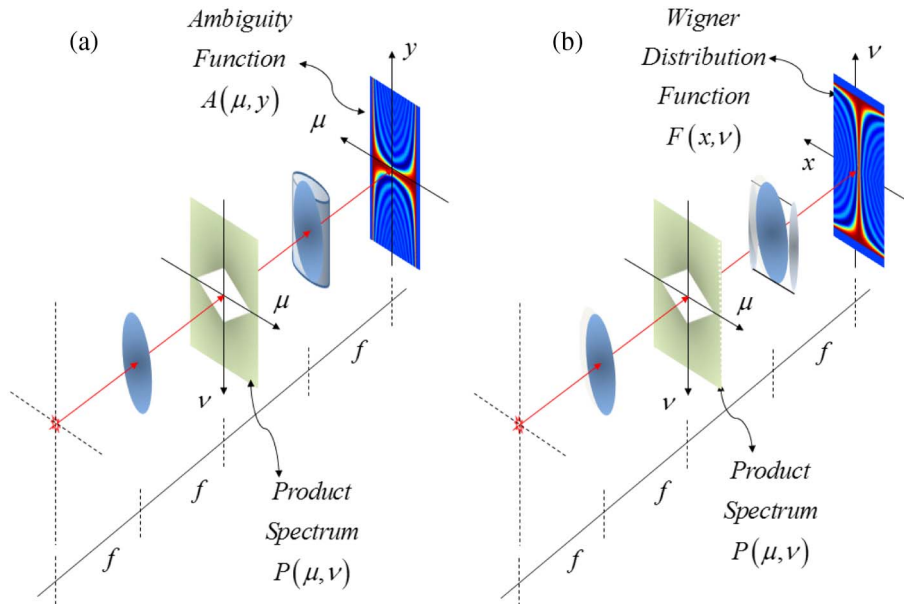
Now, on the other hand, we note that the ambiguity function of  $Q(\mu)$  or, equivalently, the ambiguity function of  $q(x)$ , is

$$\begin{aligned}
 A(\mu, y) &= \int_{-\infty}^{\infty} P(\mu, \nu) \exp\{i2\pi y\nu\} d\nu = \int_{-\infty}^{\infty} Q\left(\nu + \frac{\mu}{2}\right) Q^*\left(\nu - \frac{\mu}{2}\right) \exp\{i2\pi y\nu\} d\nu \\
 &= \int_{-\infty}^{\infty} p(x, y) \exp\{-i2\pi\mu x\} dx = \int_{-\infty}^{\infty} q\left(x + \frac{y}{2}\right) q^*\left(x - \frac{y}{2}\right) \exp\{-i2\pi\mu x\} dx. \tag{40}
 \end{aligned}$$

Hence, it is straightforward to show that

$$F(x, \nu) \int_{-\infty}^{\infty} \int_{-\infty}^{\infty} A(\mu, y) \exp\{i2\pi(x\mu - \nu y)\} d\mu dy. \tag{41}$$

**Figure 19**



Schematics of the use of anamorphic optical processors for transforming the product spectrum into (a) the ambiguity function and (b) the Wigner distribution function. The depicted cylindrical lens has the same focal length as that of the portrayed spherical lenses.

Of course, the inverse relationship of Eq. (40) is

$$A(\mu, y) = \int_{-\infty}^{\infty} \int_{-\infty}^{\infty} F(x, \nu) \exp\{-i2\pi(\mu x - y\nu)\} dx d\nu. \quad (42)$$

As was first suggested in Ref. [240], Fig. 20 summarizes pictorially the above results. The central arrows are used for denoting 2D Fourier transformations, while the peripheral arrows denote 1D Fourier transforms that are implemented by using anamorphic optical processors. In what follows, we employ the rectangular window  $Q(\mu) = \text{rect}(\mu/2\Omega)$  for illustrating the mathematical operations involved when evaluating phase-space representations. First, we evaluate the product spectrum. Second, we obtain the product space. Third, we find the mathematical expression for the Wigner distribution function. Fourth and finally, we obtain the ambiguity function of the clear pupil aperture. The product spectrum of a rectangular window is

$$\begin{aligned} P(\mu, \nu) &= \text{rect}\left(\frac{\nu + \frac{\mu}{2}}{2\Omega}\right) \text{rect}\left(\frac{\nu - \frac{\mu}{2}}{2\Omega}\right) = \text{rect}\left(\frac{\nu}{2\Omega - |\mu|}\right) \text{rect}\left(\frac{\mu}{4\Omega}\right) \\ &= \text{rect}\left(\frac{\mu}{4(\Omega - |\nu|)}\right) \text{rect}\left(\frac{\nu}{2\Omega}\right) = \diamond(\mu, \nu; \Omega). \end{aligned} \quad (43)$$

The result in Eq. (43) describes a binary screen with a rhomboidal clear aperture. Its amplitude transmittance defines in phase space the support of any bandlimited optical signal. Next, we note that as a consequence of Eq. (39), the product space of the coherent PSF is

$$p(x, y) = \text{sinc}\left[\Omega\left(x + \frac{y}{2}\right)\right] \text{sinc}\left[\Omega\left(x - \frac{y}{2}\right)\right]. \quad (44)$$

From Eq. (43) it is straightforward to evaluate the Wigner distribution function:

$$F(x, \nu) = \left(1 - \left|\frac{\nu}{\Omega}\right|\right) \text{sinc}\left[2\Omega x \left(1 - \left|\frac{\nu}{\Omega}\right|\right)\right] \text{rect}\left(\frac{\nu}{2\Omega}\right). \quad (45)$$

Again from Eq. (43), one can evaluate the normalized version of the ambiguity function:

$$A(\mu, y) = \left(1 - \left|\frac{\mu}{2\Omega}\right|\right) \text{sinc}\left[2\Omega y \left(1 - \left|\frac{\mu}{2\Omega}\right|\right)\right] \text{rect}\left(\frac{\mu}{4\Omega}\right). \quad (46)$$

Now, one of the many fascinating features of phase-space representations is the following. If one evaluates the OTF of the generalized pupil aperture,

$$Q(\mu; W_{2,0}) = T(\mu) \exp\left\{i2\pi\left(\frac{W_{2,0}}{\lambda}\right)\left(\frac{\mu}{\Omega}\right)^2\right\} \text{rect}\left[\frac{\mu}{2\Omega}\right], \quad (47)$$

one obtains

$$H_T(\mu; W_{2,0}) = \int_{-\infty}^{\infty} T\left(\nu + \frac{\mu}{2}\right) T * \left(\nu - \frac{\mu}{2}\right) \exp\left\{i2\pi\left(\frac{2W_{2,0}}{\lambda\Omega}\right)\left(\frac{\mu}{\Omega}\right)\nu\right\} d\nu. \quad (48)$$

In Eqs. (47) and (49) we denote as  $W_{2,0}$  the wavefront aberration coefficient describing focus error in an optical system. Again, the Greek letter lambda denotes the wavelength of the optical radiation.

As pointed out in Eq. (39), we know that the ambiguity function of the complex amplitude transmittance  $T(\mu)$  is

$$A_T(\mu; W_{2,0}) = \int_{-\infty}^{\infty} T\left(\nu + \frac{\mu}{2}\right) T * \left(\nu - \frac{\mu}{2}\right) \exp\{i2\pi y\nu\} d\nu. \quad (49)$$

Now, as depicted in Fig. 21, from a simple comparison of Eqs. (47) and (48) we note that

$$A_T\left(\mu, \frac{2W_{2,0}}{\lambda\Omega^2}\mu\right) = H_T(\mu; W_{2,0}). \quad (50)$$

In other words, for a given value of  $W_{2,0}$ , the values of the out-of-focus OTF are contained along the line

$$y = \left[\frac{2\mu}{\lambda\Omega^2}\right] W_{2,0}. \quad (51)$$

Since in a photographic display one can visualize only the modulus of the ambiguity function, then along the previous line, one visualizes the MTF. Furthermore, as is also depicted in Fig. 21, if one selects a fixed value of the spatial frequency, say along the vertical line  $\mu = \sigma$ , then the values of the ambiguity function are the values of the out-of-focus OTF. That is,

$$A_T\left(\sigma, \left(\frac{2\sigma}{\lambda\Omega^2}\right) W_{2,0}\right) = H_T(\sigma; W_{2,0}). \quad (52)$$

Therefore, the display of the ambiguity function is a highly redundant picture that contains all possible values of the MTFs of a pupil aperture mask  $T(\mu)$  for variable

Figure 20

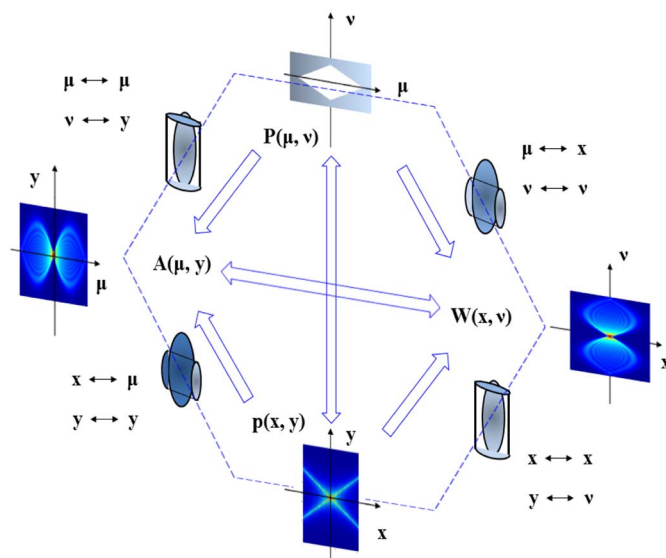


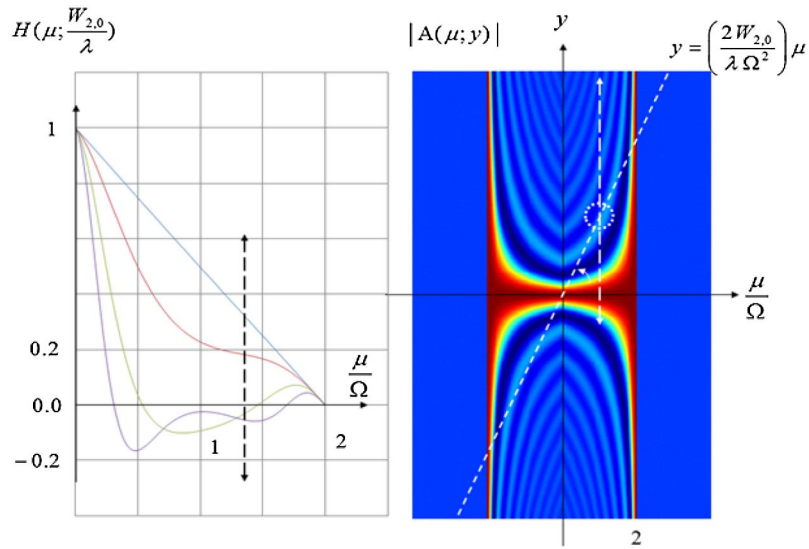
Diagram of the Fourier transformations that are required for interrelating the complex amplitude distributions used in phase-space representations. Single-headed arrows denote 1D Fourier transforms, which are implemented by using the anamorphic processors in Fig. 19. Double-headed arrows denote a 2D Fourier transform operation, which is implemented by using a classical optical processor.

focus error. This is a remarkable result that allows us to visualize the impact of focus errors on the MTF. Additionally, as we discuss next, the ambiguity function is a very helpful diagram for identifying pupil masks that reduce the influence of focus error on the OTF. To that end, it is relevant to note the following. If a pupil mask has an ambiguity function that spreads along the  $y$  axis, in the  $(\mu, y)$  plane, then according to Eqs. (51) and (52), the values of the MTF change slowly with focus error. Consequently, these masks are able to extend the depth of field. We have noted that the spread of the ambiguity function along the  $y$  axis has a peculiar elongated distribution, which is called the “bow-tie effect” [241].

In Fig. 22 we show the ambiguity functions of three different pupil masks: in Fig. 22(a) is the clear pupil aperture, in Fig. 22(b) is a cubic phase mask, and in Fig. 22(c) is a moderated Gaussian apodizer that covers a cubic phase mask. From Figs. 22(b) and 22(c), it is apparent that some masks are able to generate ambiguity functions that have elongated distributions along the vertical axis. According to the previous results (in Fig. 21), these elongated distributions indicate that the mask is able to reduce the influence of focus error in the OTF. As previously indicated, the elongated distribution is referred as the bow-tie effect. In Sections 4 and 5, we note that, rather than using a single phase mask, it is convenient to use a pair of phase masks for controlling the presence of the bow-tie effect, or, if you will, for governing the depth of field of an optical system, while preserving a fixed full pupil aperture.

Next, we express the out-of-focus OTF as a Taylor series expansion. We show that certain masks are able to reduce, by one-half, the number of terms of the Taylor series. If one expresses the OTF versus focus error as a Taylor series around  $W_{2,0} = 0$ , one obtains

Figure 21



Graphical procedure for extracting the values of the MTF versus focus error by using the values of the ambiguity function associated with the pupil complex amplitude transmittance. At the left-hand side, we use broken lines with double arrows to depict the variations of the MTF with focus error, at a fixed spatial frequency. At the right-hand side, we identify the intersection of two broken lines as the value of the MTF. As is shown in the text, the slope of the tilted broken line is related to the focus error coefficient, while the vertical broken line identifies a fixed spatial frequency.

$$H_T(\mu; W_{2,0}) = \sum_{m=0} \frac{(W_{2,0})^m}{m!} \left\{ \left( \frac{\partial}{\partial W_{2,0}} \right)^m H_T(\mu; W_{2,0}) \right\} \Big|_{W_{2,0}=0}. \quad (53)$$

In the above series expansion, we note that the  $m$ -fold derivative is

$$\left\{ \left( \frac{\partial}{\partial W_{2,0}} \right)^m H_T(\mu; W_{2,0}) \right\} \Big|_{W_{2,0}=0} = \left( \frac{4\pi\mu}{\lambda\Omega^2} \right)^m \int_{-\infty}^{\infty} \nu^m T\left(\nu + \frac{\mu}{2}\right) T * \left(\nu + \frac{\mu}{2}\right) d\nu. \quad (54)$$

Trivially, since the variable  $\nu$  to the power  $m = 2n + 1$  is an odd function, the integral in Eq. (47) can be equal to zero provided that the remaining part of the integrand is an even function in the variable  $\nu$ . That is,

$$P(\mu, \nu) = T\left(\nu + \frac{\mu}{2}\right) T * \left(\nu + \frac{\mu}{2}\right) = P(\mu, -\nu). \quad (55)$$

By expressing the complex amplitude transmittance in terms of its modulus and its phase, we conclude that the condition in Eq. (55) is achieved if

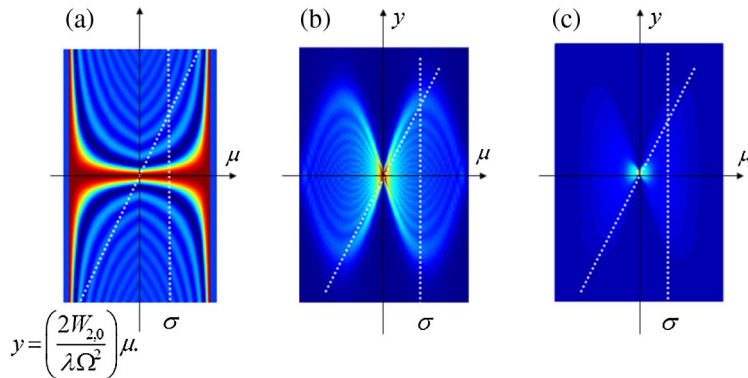
$$T(\nu) = |T(\nu)| \exp\{i\chi(\mu)\} = |T(-\nu)| \exp\{-i\chi(-\mu)\} = |T(\nu)| \exp\{-i\chi(-\mu)\}. \quad (56)$$

Thus, for reducing the impact of focus errors on the OTF, one needs to use phase variations that are odd functions, such as those depicted in Fig. 23, which can be expressed as

$$Q_n(\nu) = \exp \left\{ i2\pi a \operatorname{sgn}(\nu) \left| \frac{\nu}{\Omega} \right|^n \right\}. \quad (57)$$

In Eq. (57) the Latin letter  $a$  denotes the optical path difference. The signum function is denoted as  $\operatorname{sgn}(\nu)$ , as is described in Ref. [242]. The phase variations are described by monomial to the power  $n$ . At the left-hand side of Fig. 23, we display the phase profiles associated to Eq. (57) for  $n = 1, 2, 3, 4, 5, 6, 7, 8$ , and 9. At the right-hand side of Fig. 23, we show the interferograms for  $n = 2, 3, 4, 5, 6, 7, 8$ , and 9.

**Figure 22**



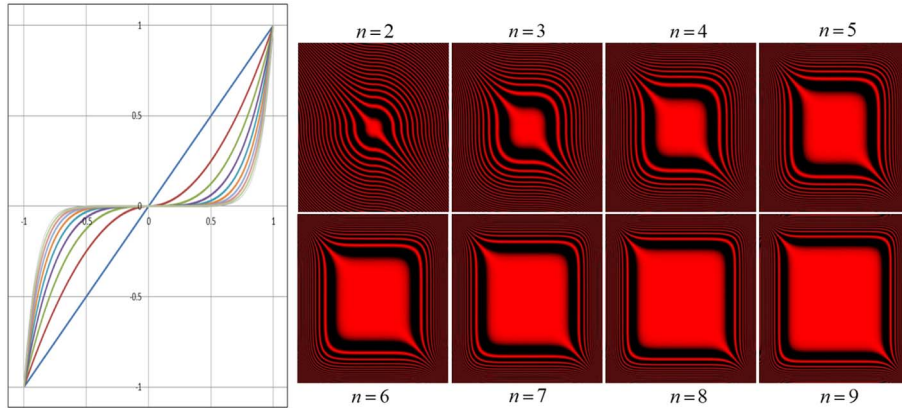
Display of the modulus of the ambiguity functions obtained by using three different pupil masks. By employing the procedure in Fig. 21, one can identify the impact of focus error on the MTF. The last two pictures exhibit the bow-tie effect on the ambiguity function.

From Fig. 24 it is apparent that this type of phase mask is able to reduce the influence of focus error. Furthermore, we note that, by using the asymmetric phase variations of high order (say  $n = 5, 6$ ), one preserves the overall appearance of the input picture.

It is interesting to note that the power  $n$ , in Eq. (57), can be indeed a real number. This latter type of phase mask is denoted as a fractional power wavefront [243]. More details are given in what follows.

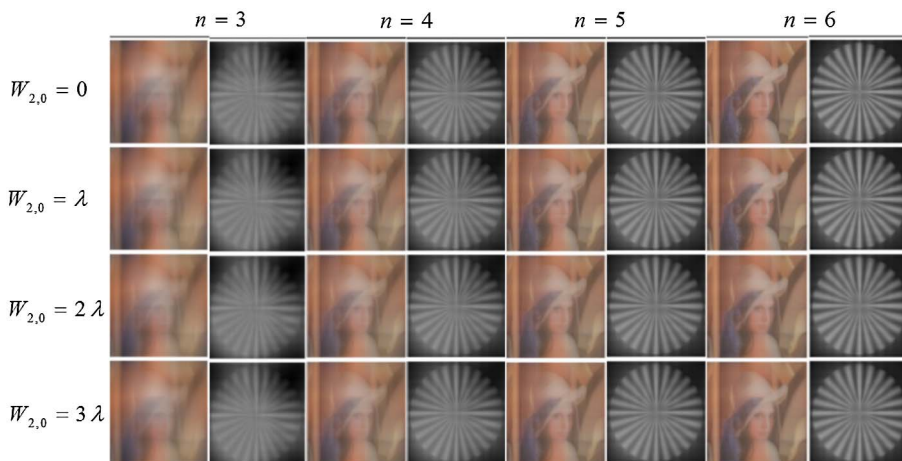
Here, it is convenient to recognize that one can obtain an optical display of the ambiguity function by employing an anamorphic processor, as is shown in Fig. 25. We recognize that along any vertical line of the ambiguity function (depicted as a set

**Figure 23**



Asymmetric phase profiles and their associated interferograms. At the left-hand side, we plot the monomials  $\text{sign}(\mu) |\mu/\Omega|$  to the power  $n = 1, 2, 3, 4, 5, 6, 7, 8, 9$ . At the right-hand side, we display the 2D interferograms that are generated employing a plane wave, as a reference beam, and the masks that have the 2D versions of the phase profiles at the left-hand side.

**Figure 24**



Array of pictures depicting the images that one gathers when using an optical system that suffers from focus errors, and if its pupil aperture is covered with the phase mask in Fig. 23. Along the rows of this array of pictures, we increase the values of the focus error coefficient,  $W_{2,0} = 0, \lambda, 2\lambda$ , and  $3\lambda$ . Along the columns, we show the changes when increasing the power of the asymmetrical phase masks.

of broken lines in Fig. 25), the complex amplitude distribution comes from the Fraunhofer diffraction pattern of a vertical line along the product spectrum  $P(\mu; \nu)$ . It is convenient to note that the product spectrum can be thought of as being formed by a continuous set of rectangular windows. In mathematical terms,

$$P(\mu, \nu) = \text{rect}\left(\frac{\nu}{2\Omega - |\mu|}\right) \text{rect}\left(\frac{\mu}{4\Omega}\right). \quad (58)$$

Hence, the complex amplitude distribution along the  $y$  axis of the ambiguity function can be thought of as being formed by a continuous set of Fraunhofer diffraction patterns. That is,

$$A(\mu, y) = \left(1 - \left|\frac{\mu}{2\Omega}\right|\right) \text{sinc}\left[2\Omega y \left(1 - \left|\frac{\mu}{2\Omega}\right|\right)\right] \text{rect}\left(\frac{\mu}{4\Omega}\right). \quad (59)$$

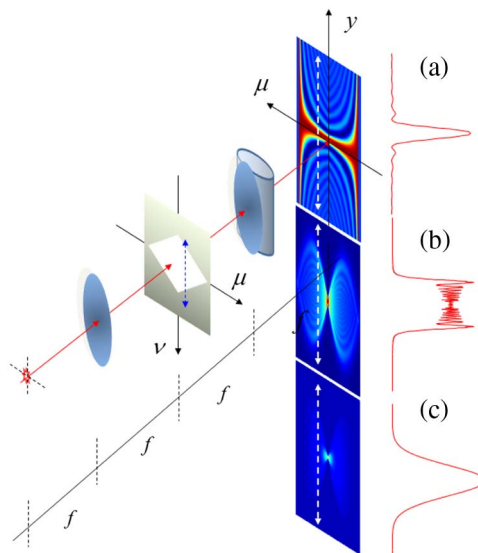
Along this type of conceptual chart, we consider other possibilities. For example, let us assume that at the product spectrum any vertical line has now a quadratic phase factor,

$$P(\mu, \nu) = \exp\left\{i2\pi\left(\frac{\nu}{\Omega}\right)^2\right\} \text{rect}\left(\frac{\nu}{2\Omega - |\mu|}\right) \text{rect}\left(\frac{\mu}{4\Omega}\right). \quad (60)$$

For obtaining this type of product spectrum, one needs a cubic phase mask. Then, the anamorphic optical processor generates the following ambiguity function:

$$A(\mu, y) = \text{rect}\left(\frac{\mu}{4\Omega}\right) \int_{-\frac{2\Omega - |\mu|}{2}}^{\frac{2\Omega - |\mu|}{2}} \exp\left\{i2\pi a\left(\frac{\nu}{\Omega}\right)^2 + i2\pi y\nu\right\} d\nu. \quad (61)$$

Figure 25



Schematics for visualizing, along a vertical line, the variations of the ambiguity function as a 1D Fraunhofer diffraction pattern. (a) The formation of a 1D Fraunhofer diffraction pattern of a rectangular aperture. (b) Depiction of the formation of a 1D Fraunhofer diffraction pattern of a cubic phase mask. (c) The 1D Fraunhofer diffraction pattern of the moderate Gaussian apodizer that covers a cubic phase mask.

It is apparent from Eq. (61) that, along the  $y$  axis, the ambiguity function is now composed by a continuous set of Fresnel diffraction patterns of rectangular windows. Then, the ambiguity function spreads over the  $(\mu, y)$  plane. As a result, the OTF has low sensitivity to focus errors. One can extrapolate this result by exploring the use of high-order aberration polynomials at the product spectrum, as was indicated in Eq. (57). However, it is relevant to note that these phase-only masks introduce spurious oscillations on the MTF. For reducing this undesirable feature, next we explore the use of the following amplitude transmittances:

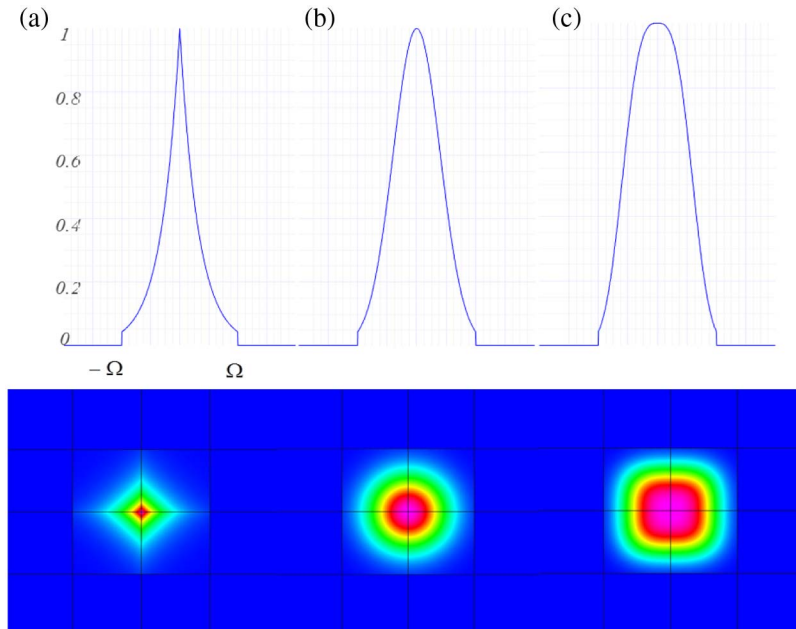
$$Q_s(\nu) = 1 - \left| \frac{\nu}{\Omega} \right|^s, \quad (62a)$$

$$Q_s(\nu) = \exp \left\{ -c \left| \frac{\nu}{\Omega} \right|^s \right\}. \quad (62b)$$

In Eq. (62a) the Latin letter  $s$  is a real positive number that denotes the power of the attenuation monomial. In Eq. (62b) the lowercase letter  $c$  denotes a damping factor in the amplitude mask, and, again, the Latin letter  $s$  is the power of the monomial inside the argument of the exponential function. Here it is relevant to recognize the following notation for the Gaussian-like profiles. As depicted in Fig. 26, if in Eq. (62) we set  $s = 2$ , then we have a Gaussian attenuating mask. For  $0 < s < 2$ , we have a sub-Gaussian mask, and if  $s > 2$ , then we have a super-Gaussian mask. When referring to any value of  $s$ , we employ the generic notation hyper-Gaussian mask [244].

It is known that amplitude masks are able to reduce the influence of focus errors on the MTF. However, amplitude masks reduce the light-gathering power of an optical system. In what follows, we show that amplitude masks with moderate absorption are

**Figure 26**



Amplitude transmittances associated with several types of hyper-Gaussian masks. At the top, we display the graphs of the amplitude transmittance profiles of (a) sub-Gaussian masks, (b) Gaussian masks, and (c) super-Gaussian masks. At the bottom, we show pseudo-color variations that encode the 2D versions of the amplitude transmittance at the top of this figure.

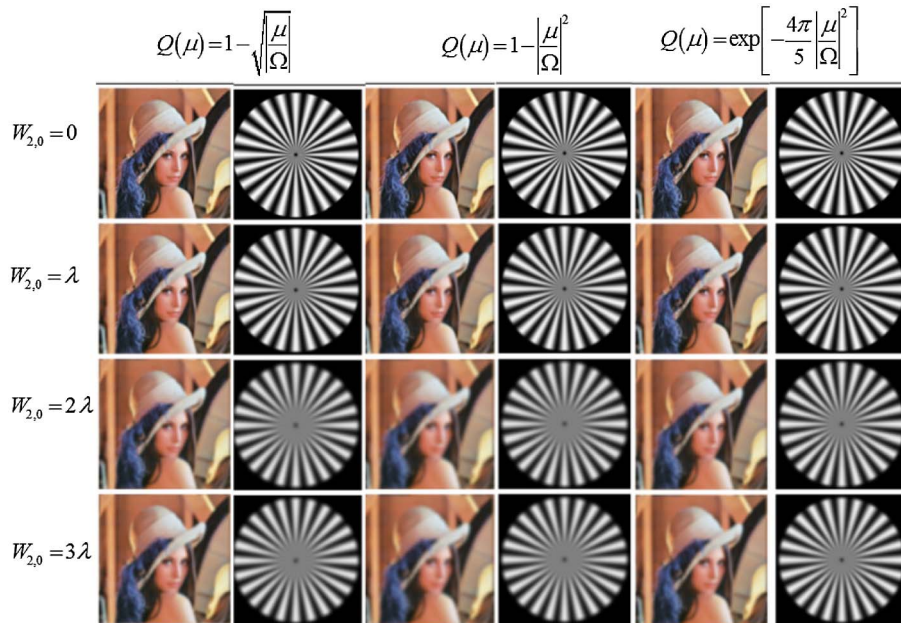
useful for reducing spurious oscillation of the MTF, which is caused by phase masks. To our end, in Fig. 27 we display the images that one can obtain when using amplitude masks.

It is apparent from Fig. 27 that these absorption masks are able to reduce the influence of focus error, inside the range  $|W_{2,0}| \leq 3\lambda$ . Furthermore, we note that when using amplitude masks (as it happens when using high-order phase masks, say for  $n = 5, 6$ ), one preserves the overall appearance of the input picture. In what follows we recognize that the actual importance of using the amplitude masks is depicted in Fig. 28.

We show in Fig. 28(a) that by using a cubic phase mask, the MTF (in decibels) exhibits spurious oscillations around the tendency curve. In Fig. 28(b) we show that one can mitigate these spurious oscillations by using Gaussian amplitude masks, which have moderate absorption coefficients. Furthermore, by comparison of the normalized MTFs in Figs. 28(c) and 28(d), we note also that the amplitude masks increase the bandwidth of the MTFs. Hence, we claim that the amplitude masks have a favorable impact, for extending the depth of field, when one employs the cubic phase mask.

Now, in Fig. 29 we present an array of pictures for making visual comparisons, which illustrate further the advantages of using moderate Gaussian absorption masks, which work together with cubic phase masks. Along Row 1 of Fig. 29, we display the pictures obtained when using only a cubic phase mask (with an optical path difference of  $a = 15$ ). Along Row 2 of Fig. 29, we show the pictures obtained when one covers (the above described phase mask) with a Gaussian absorption mask ( $s = 2$  and  $c = 7\pi/10$ ). From Fig. 28 and from a simple comparison between the Row 1 and

Figure 27



Array of images obtained when using amplitude masks over the pupil aperture. Along the rows of the array, we increase the value of the focus error coefficient,  $W_{2,0} = 0, \lambda, 2\lambda, 3\lambda$ . Along the two initial columns, as is indicated at the top of this figure, the pupil mask has the amplitude filter in Eq. (62a) with  $s = 1/2$ . Along the two intermediate columns, the amplitude filter has a power  $s = 2$ . Along the final columns, the amplitude transmittance is the one in Eq. (62b) with  $c = 7\pi/10$  and  $s = 2$ .

the Row 2 of Fig. 29, we claim that, for reducing the impact of focus error while avoiding the presence of spurious oscillations, it is convenient to employ both a phase mask and an amplitude mask. Toward this goal, we analyze the use of masks that have the following complex amplitude transmittance:

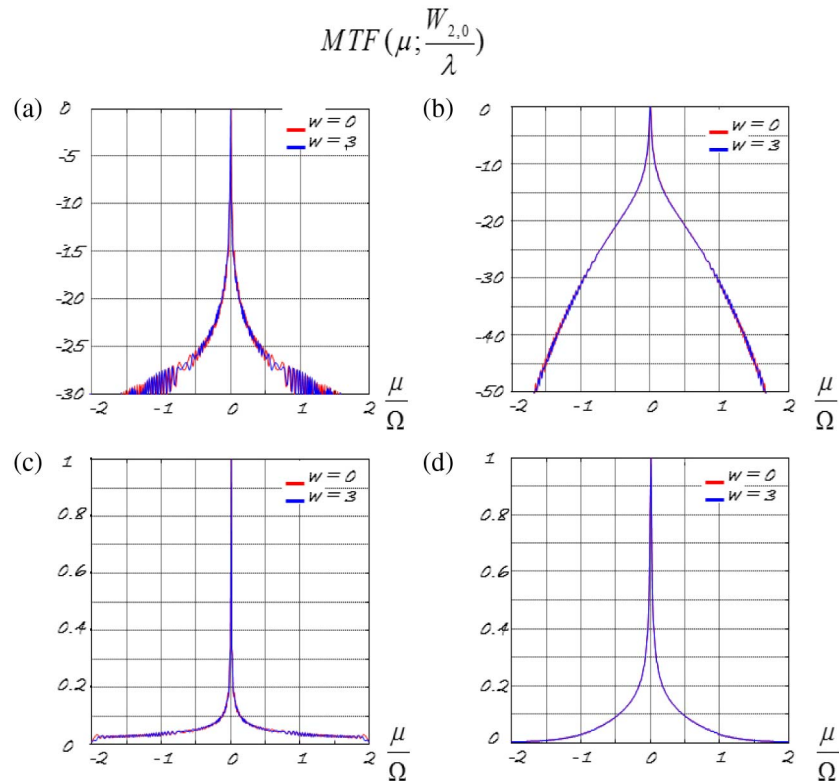
$$Q_{m,s}(\nu) = \exp \left\{ i2\pi a \operatorname{sgn}(\nu) \left| \frac{\nu}{\Omega} \right|^m \right\} \exp \left\{ -c \left| \frac{\nu}{\Omega} \right|^s \right\}, \quad (63)$$

In Fig. 30 we show the main features of the following complex amplitude transmittance:

$$Q_{m,s}(\mu, \nu) = \exp \left\{ i24\pi \left[ \operatorname{sgn}(\mu) \left| \frac{\mu}{\Omega} \right|^m + \operatorname{sgn}(\nu) \left| \frac{\nu}{\Omega} \right|^m \right] \right\} \\ \times \exp \left\{ -1.13 \left[ \left| \frac{\mu}{\Omega} \right|^s + \left| \frac{\nu}{\Omega} \right|^s \right] \right\} \operatorname{rect} \left( \frac{\mu}{2\Omega} \right) \operatorname{rect} \left( \frac{\nu}{2\Omega} \right). \quad (64)$$

Of course, there is a wide range of values that the coefficients  $a$  and  $c$  can take. The same is true for the values of  $m$  and  $s$ . After several numerical evaluations, we have suggested employing the following complex amplitude transmittance:

**Figure 28**



Visualizing the influence of a moderate absorption mask on the MTF. In (a) we show in decibels the in-focus MTF (red curve) and the out-of-focus MTF (blue curve) of a cubic phase mask. In (b) we show, also in decibels, the two MTFs that are obtained when using a moderate absorption mask (with Gaussian profile) and the cubic phase mask. In (c) and (d), we plot the equivalent results, if one evaluates the normalized versions of the MTFs.

$$Q_{\text{phase}}(\mu, \nu) = \exp \left\{ i24\pi \left[ \text{sgn}(\mu) \left| \frac{\mu}{\Omega} \right|^{3.1} + \text{sgn}(\nu) \left| \frac{\nu}{\Omega} \right|^{3.1} \right] \right\} \text{rect} \left( \frac{\mu}{2\Omega} \right) \text{rect} \left( \frac{\nu}{2\Omega} \right). \quad (65)$$

For visualizing this proposal, we employ Fig. 30. At the margins of the interferogram, we indicate the phase profile of the fractional wavefront.

Furthermore, along the margins of the of the pseudo-color display that encodes the attenuation values, we depict the amplitude variations of the hyper-Gaussian mask:

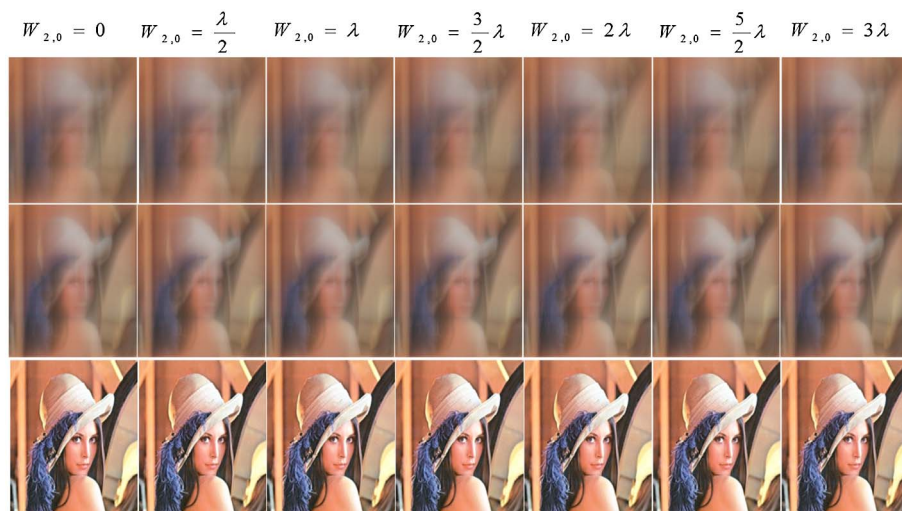
$$Q_{\text{ampl}}(\mu, \nu) = \exp \left\{ -1.13 \left[ \left| \frac{\mu}{\Omega} \right|^{4.7} + \left| \frac{\nu}{\Omega} \right|^{4.7} \right] \right\} \text{rect} \left( \frac{\mu}{2\Omega} \right) \text{rect} \left( \frac{\nu}{2\Omega} \right). \quad (66)$$

Here it is relevant to indicate that *the OTF is never invariant to focus error inside the passband of the optical system*. However, by properly selecting a pupil mask and within a certain range of values of  $W_{2,0}$ , the square value of the difference between the out-of-focus OTF and the in-focus OTF can have rather small values of  $\eta$ . That is,

$$0 < |H(\mu; W_{2,0}) - H(\mu; 0)|^2 = \eta \ll 1. \quad (67)$$

Again, strictly speaking, the value of  $\eta$  is never equal to zero inside the passband. However, if one uses some of the masks in Eq. (66), inside the range  $0 \leq W_{2,0} \leq 3\lambda$ , then  $\eta = 10^{-6}$ . In the following section, we describe methods for implementing tunable versions of the phase masks, as well as tunable versions of the amplitude masks. *We show that by using tunable versions, one can suitably govern the depth of field, while the optical system remains working at full pupil aperture.*

**Figure 29**



Array of pictures for visualizing the influence of a moderate absorption mask on the MTF. Along the columns of this array, we increase the value of the focus error coefficient. Along Row 1 we display the images gathered with a cubic phase mask. Along Row 2, we show the images obtained when using an amplitude mask with a Gaussian profile covering the cubic phase mask at the pupil aperture. Along Row 3, we show the images obtained after an inverse digital filter is applied to the pictures along Row 2 of this figure.

#### 4. PHASE CONJUGATE PAIRS

In what follows we consider an admittedly naïve approach, yet a very useful one, for exploiting the mathematical operations involved when evaluating the ambiguity function

$$A(\sigma, y) = \int_{-\infty}^{\infty} Q\left(\nu + \frac{\sigma}{2}\right) Q^*\left(\nu - \frac{\sigma}{2}\right) \exp\{i2\pi\nu y\} d\nu. \quad (68)$$

Inside the integrand in Eq. (68), trivially, we recognize the kernel of the Fourier transform as well as the product of two complex amplitude distributions. One complex amplitude distribution is the complex conjugate of the other. Furthermore, the two complex amplitude distributions are laterally displaced by the spatial frequency  $\sigma$ .

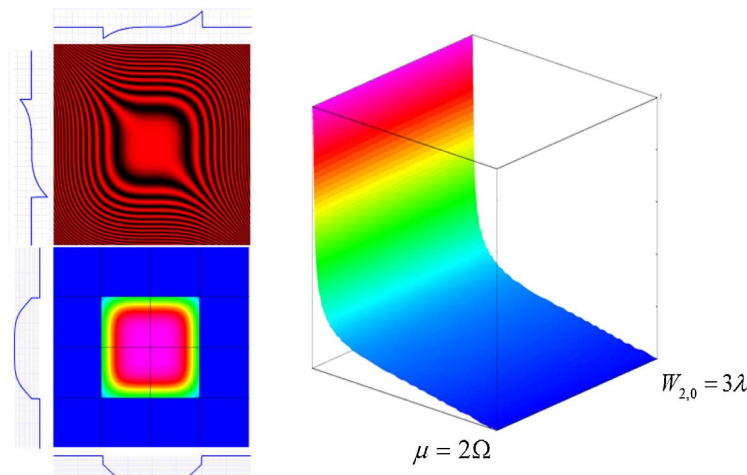
In Fig. 31 we depict a coherent optical processor that performs the same operation. However, now the complex amplitude distributions are associated to the complex amplitude transmittances of two masks, which are physically displaced by the spatial frequency  $\sigma$ . At the pupil aperture of the optical processor, the complex amplitude transmittance of the first mask is  $T_1(\nu)$ , and the complex amplitude transmittance of second mask is the complex conjugate of the first element,  $T_2(\nu) = T_1^*(\nu)$ . The pair is denoted here as a complex conjugate pair.

If a lateral displacement is introduced between the elements of the complex conjugate pair (say by the value  $\sigma$ ), then one implements the following complex amplitude transmittance:

$$P(\mu = \sigma, \nu) = T_1\left(\nu + \frac{\sigma}{2}\right) T_2\left(\nu - \frac{\sigma}{2}\right) = T_1\left(\nu + \frac{\sigma}{2}\right) T_1^*\left(\nu - \frac{\sigma}{2}\right). \quad (69)$$

The amplitude transmittance in Eq. (69) is the generalized pupil function of the optical processor in Fig. 31. We remember that this complex amplitude transmittance is a

Figure 30



Pictorials describing a complex amplitude filter that reduces the influence of focus error and spurious oscillations. At the left-hand side, upper corner, we present the interferogram. At the margins of the interferogram, as blue curves, are the phase profiles. At the left-hand side, lower corner, we display the pseudo-color representation of the amplitude variations of the 2D mask. Again, at its margins, as blue curves, we plot the amplitude profiles. At the right-hand side, we plot the MTF for variable focus error in the interval  $0 \leq W_{2,0} \leq 3\lambda$ .

vertical line in the product spectrum, which is shown in Fig. 25. For the complex conjugate pair, the coherent PSF is

$$t(x; \sigma) = \int_{-\infty}^{\infty} T_1\left(\nu + \frac{\sigma}{2}\right) T_1^*\left(\nu - \frac{\sigma}{2}\right) \exp\{i2\pi x\nu\} d\nu = A(\sigma, x). \quad (70)$$

By a simple comparison of Eq. (68) and Eq. (70), we recognize that, when using a complex conjugate pair, the coherent PSF is equal to a vertical line along the ambiguity function of  $T_1(\nu)$ , which is the complex amplitude transmittance of one element of the pair. This is a noteworthy result. *By physically using a pair of phase masks (in a coherent optical processor) one can understand the influence that a single mask has on the out-of-focus OTF.* Now, if we take into account the influence of focus error in the optical processor, then the irradiance PSF is

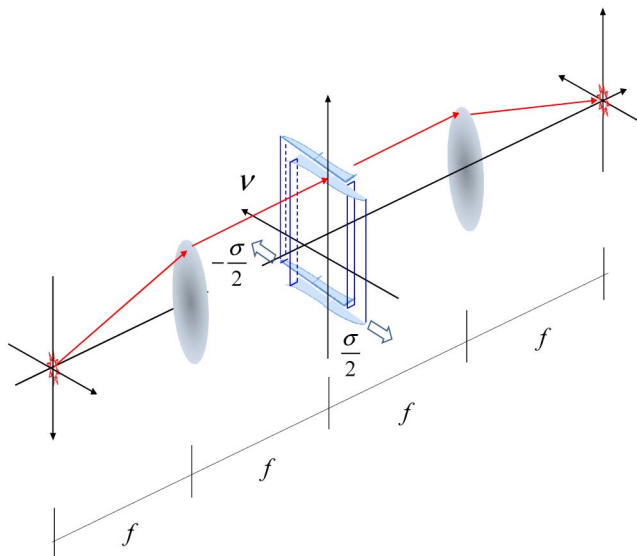
$$h(x; \sigma; W_{2,0}) = \left| \frac{\int_{-\infty}^{\infty} T_1\left(\nu + \frac{\sigma}{2}\right) T_1^*\left(\nu - \frac{\sigma}{2}\right)}{\exp\left\{i2\pi\left(\frac{W_{2,0}}{\lambda}\right)\left(\frac{\nu}{\Omega}\right)^2\right\} \exp\{i2\pi x\nu\}} d\nu \right|^2. \quad (71)$$

Hence, it is straightforward to obtain the OTF associated to the PSF in Eq. (71), which is

$$\begin{aligned} H(\mu; \sigma; W_{2,0}) &= \int_{-\infty}^{\infty} h(x; \sigma; W_{2,0}) \exp\{-i2\mu x\} dx \\ &= \int_{-\infty}^{\infty} A\left(\mu, y + \frac{W_{2,0}}{\lambda\Omega^2}\right) A^*\left(\mu, y - \frac{W_{2,0}}{\lambda\Omega^2}\right) \exp\{-i2\pi\mu x\} dx. \end{aligned} \quad (72)$$

It is apparent from Eq. (72) that now the expression for evaluating the OTF resembles again the mathematical operation for obtaining an ambiguity function. However, now the mathematical operation uses the ambiguity function of one element of the pair. These general results are illustrated next, by recognizing that the above method is

**Figure 31**



Schematics of an optical processor that employs two spherical lenses (with fixed focal length  $f$ ) and a varifocal lens as a spatial filter, which is located at the Fraunhofer plane.

useful for setting several tunable optical devices, which have interesting properties under noncoherent illumination.

#### 4.1. Varifocal Lenses and Axial Scanners

As pointed out in the introduction of this paper, Kitajima apparently was the first person to describe an optical device for implementing varifocal lenses. Later on, an improved version was discovered, independently and simultaneously, by Lohmann and Alvarez; as was indicated in the introduction. Next, we discuss a 1D model of these proposals. Let us consider that the complex amplitude transmittance of one element of the pair is

$$T_1(\nu) = \exp \left\{ i2\pi a \left( \frac{\nu}{\Omega} \right)^3 \right\} \text{rect} \left( \frac{\nu}{2\Omega} \right). \quad (73)$$

In Eq. (73) the lowercase letter  $a$  denotes the optical path difference in units of the wavelength  $\lambda$ . When this optical element is used as a complex conjugate pair, one sets the following generalized pupil function:

$$\begin{aligned} P(\mu = \sigma, \nu) &= \exp \left\{ i2\pi \left( \frac{3a\sigma}{\Omega} \right) \left( \frac{\nu}{\Omega} \right)^2 \right\} \text{rect} \left( \frac{\nu + \frac{\sigma}{2}}{2\Omega} \right) \text{rect} \left( \frac{\nu - \frac{\sigma}{2}}{2\Omega} \right) \\ &= \exp \left\{ i2\pi \left( \frac{3a\sigma}{\Omega} \right) \left( \frac{\nu}{\Omega} \right)^2 \right\} \diamond (\nu, \sigma; \Omega). \end{aligned} \quad (74)$$

The complex amplitude transmittance in Eq. (74) represents a lens with tunable optical power, which is located at the frequency domain. As is depicted in Fig. 32, this optical device can be applied to implement a telecentric axial scanner. Heuristically, from the viewpoint of geometrical optics, one can describe the behavior of this device as follows. On the one hand, at the top of Fig. 32, we note that if  $\sigma = 0$  then the point source (located at  $z = 0$ ) is able to pass through the pinhole, which is placed at the image of the telecentric processor. On the other hand (as depicted at the bottom of Fig. 32), by laterally shifting the elements of the complex conjugate pair, a point source located at  $z \neq 0$  is able to pass through the pinhole.

For the above application, and from the viewpoint of technical optics, it is relevant to express the focus error coefficient in terms of the axial displacement  $z$ ; for fine details, see the following references [245]. Here we use Newton's imaging formula for a point source located at a distance  $z$ , before the front focal plane of the optical processor. Its image is located at the distance  $z' = -f^2/z$ . Since at the Fraunhofer plane the reference sphere is a plane wave, then the focus error aberration coefficient is

$$W_{2,0} = \frac{h^2}{2} \left( \frac{1}{R} - \frac{1}{R_0} \right) \Big|_{R_0 \rightarrow \infty} = -\frac{h^2}{2f^2} z = -\frac{z}{8(f\#)^2}. \quad (75)$$

In Eq. (75) we denote the  $f$ -number as  $f\#$ . This means that a focus error coefficient that is equal to  $3\lambda$  (with  $\lambda \approx 5 \times 10^{-7}$  m) implies a longitudinal displacement equal to  $z = -24(f\#)^2$ . For example, if  $f\# = 11$ , then  $z \approx -1.5$  mm. Now, from Eqs. (74) and (75), we note that, for canceling the wavefront error associated to the point source position  $z$ , we require that

$$1 = \exp \left\{ i2\pi \left[ \left( \frac{3a\sigma}{\Omega} \right) + \left( \frac{W_{2,0}}{\lambda} \right) \right] \left( \frac{\nu}{\Omega} \right)^2 \right\}; \quad a = \frac{(N-1)e}{\lambda}; \quad \frac{\sigma}{\Omega} = \frac{d}{h}. \quad (76)$$

In Eq. (76) we denote as  $N$  the refractive index of the optical glass, the Latin letter  $e$  is the physical thickness of one element of the phase conjugate pair, and the lateral

displacement is equal to  $d = \lambda f \sigma$ . As before, the pupil aperture is  $h = \lambda f \Omega$ . Hence, from Eq. (76), we obtain

$$d = \left[ \frac{h}{(N-1)e(f\#)^2} \right] z. \quad (77)$$

For the above numerical example, if  $N = 1.5$  and  $e = 0.99$  mm, we obtain that  $d \approx h/40$ , which is indeed a feasible value.

#### 4.2. Quartic Phase Masks for a Tunable Cubic Phase Mask

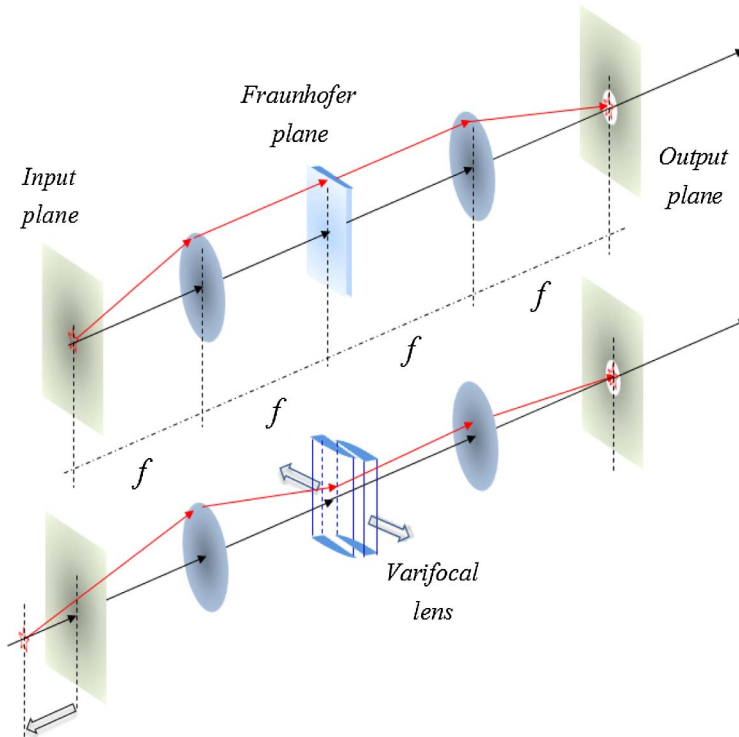
Of course, one can extrapolate the previous result for proposing a tunable, or controllable, cubic phase mask [246,247]. In what follows, we discuss an extension to Lohmann–Alvarez lenses by considering the use of the following transparent mask:

$$T_1(\nu) = \exp \left\{ i2\pi a \left( \frac{\nu}{\Omega} \right)^4 \right\} \text{rect} \left( \frac{\nu}{2\Omega} \right). \quad (78)$$

By employing this phase mask and its complex conjugate mask, one can generate the following complex amplitude transmittance:

$$T(\nu; \sigma) = \exp \left\{ i2\pi \left( \frac{4a\sigma}{\Omega} \right) \left( \frac{\nu}{\Omega} \right)^3 + i2\pi \left( \frac{\sigma}{\Omega} \right)^3 \frac{\nu}{\Omega} \right\} \diamond (\nu; \sigma; \Omega). \quad (79)$$

Figure 32



Schematics of an axial scanning technique. We employ geometrical optics rays for indicating the following. At the top, we show the image of a point source that is able to pass through a pinhole located at the output plane. At the bottom, we show another point source that is now located at a different position along the optical axis. Due to the influence of the varifocal lens, the image of this second point source is now able to pass through the same pinhole.

It is clear from Eq. (79) that, by changing the value of  $\sigma$ , we can change the optical path difference of a cubic phase mask. In other words, one can control the optical path difference of the cubic phase mask that extends the depth of field. Therefore, without modifying the size of the pupil aperture, one can control the influence of focus error on the MTF by laterally displacing a pair of complex conjugate masks, where each mask has the complex amplitude transmittance in Eq. (79). We note that, despite the fact that the proposed phase mask generates a linear phase variation, in the variable  $\nu$ , this term is irrelevant from the viewpoint of the MTF. In other words, from Eq. (79) we recognize that the OTF is

$$\begin{aligned} H(\mu; \sigma; W_{2,0}) &= \int_{-\infty}^{\infty} T\left(\nu + \frac{\mu}{2}; \sigma\right) T^*\left(\nu - \frac{\mu}{2}; \sigma\right) \exp\left\{i2\pi\left(\frac{2W_{2,0}\mu}{\lambda\Omega^2}\right)\nu\right\} d\nu \\ &= \exp\left\{i2\pi a\left(\frac{\sigma}{\Omega}\right)^3\left(\frac{\mu}{\Omega}\right)\right\} \\ &\quad \times \int_{-\infty}^{\infty} \exp\left\{i2\pi\left(\frac{12a\sigma\mu}{\Omega^2}\right)\left(\frac{\nu}{\Omega}\right)^2\right\} \\ &\quad \times \exp\left\{i2\pi\left(\frac{2W_{2,0}\mu}{\lambda\Omega^2}\right)\nu\right\} \diamond(\mu; \nu; \Omega) \diamond(\nu; \sigma; \Omega) d\nu. \end{aligned} \quad (80)$$

It is apparent from Eq. (80) that the MTF is independent from the linear phase factor outside the integral. The proposal of a phase conjugate pair (using two quartic phase elements) enables us to tune the depth of field by selecting the proper amount of lateral displacement  $\sigma$ . The whole operation can have the same fully open pupil aperture, provided that the elements of the phase conjugate pair are larger than the pupil. This condition implies that the members of the pair are magnified by a factor  $L$ , which is a real number such that  $L > 1$ . In practical terms, this means that we do not pay attention to the influence of this function when evaluating Eq. (80).

#### 4.3. Tunable Sinusoidal Phase Mask

For having an alternative analytical model for the use of phase masks that extend field depth, one of us proposed analyzing the behavior of a phase mask that has a sinusoidal profile, as depicted with the red curve in Fig. 30. This phase mask is also useful for describing the bow-tie effect, as was previously indicated in Fig. 22.

Ostensibly from Fig. 33, a sinusoidal phase profile approximates the profile of a cubic phase mask. Other authors have also considered the use of phase profiles that obey trigonometric relationships [248,249]. In what follows, we discuss a simple analytical model for implementing a tunable sinusoidal phase mask. To our end, each member of the pair now has a cosinusoidal phase profile [250]. This approach has been recently revisited by other authors [251]. Now, the complex amplitude transmittance of the first element of the pair is

$$T_1(\nu) = \exp\left\{i2\pi a \cos\left(\frac{\pi\nu}{2\Omega}\right)\right\} \text{rect}\left(\frac{\nu}{2\Omega}\right). \quad (81)$$

In Eq. (81) and Fig. 33, we consider only a section of a cosinusoidal phase variation. We show in what follows that this phase mask is useful for governing the depth of field, while working at full pupil aperture. By employing the above mask and its complex conjugate mask, it is easy to show that the complex amplitude transmittance of the phase conjugate pair is

$$T(\nu; \sigma) = \exp\left\{i2\pi\left[2a \sin\left(\frac{\pi\sigma}{4\Omega}\right)\right] \sin\left(\frac{\pi\nu}{2\Omega}\right)\right\} \diamond(\nu; \sigma; L\Omega). \quad (82)$$

It is apparent from Eq. (82) that, by changing the value of  $\sigma$ , we can change the optical path difference of a section of a sinusoidal phase mask. Hence, the proposed phase conjugate pair is a tunable device. The out-of-focus OTF associated to Eq. (82) can be obtained by evaluating

$$H(\mu, \sigma; W_{2,0}) = \int_{-\infty}^{\infty} T\left(\nu + \frac{\mu}{2}; \sigma\right) T^*\left(\nu - \frac{\mu}{2}; \sigma\right) \exp\left\{i2\pi\left(\frac{2W_{2,0}\mu}{\lambda\Omega^2}\right)\nu\right\} d\nu. \quad (83)$$

As is shown in Appendix B, the out-of-focus OTF is

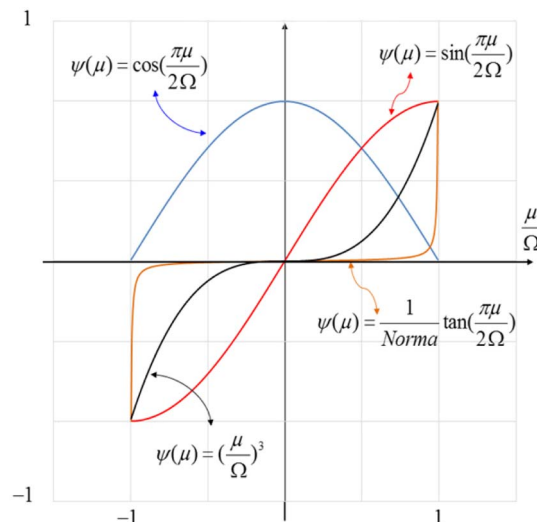
$$\begin{aligned} H(\mu; \sigma; W_{2,0}) &= \left(1 - \left|\frac{\mu}{2\Omega}\right|\right) \sum_{m=-\infty}^{\infty} (-i)^m J_m \left[8\pi a \sin\left(\frac{\pi\sigma}{4\Omega}\right) \sin\left(\frac{\pi\mu}{4\Omega}\right)\right] \\ &\times \text{sinc}\left\{\left(1 - \left|\frac{\mu}{2\Omega}\right|\right) \left[8\left(\frac{W_{2,0}}{\lambda}\right) \left(\frac{\mu}{2\Omega}\right) - \frac{m}{2}\right]\right\} \text{rect}\left(\frac{\mu}{4\Omega}\right). \end{aligned} \quad (84)$$

Of course, Eq. (84) contains as a particular case the in-focus OTF

$$\begin{aligned} H(\mu; \sigma; 0) &= \left(1 - \left|\frac{\mu}{2\Omega}\right|\right) J_0 \left[8\pi a \sin\left(\frac{\pi\sigma}{4\Omega}\right) \sin\left(\frac{\pi\mu}{4\Omega}\right)\right] \text{rect}\left(\frac{\mu}{4\Omega}\right) \\ &+ 2\left(1 - \left|\frac{\mu}{2\Omega}\right|\right) \left\{ \sum_{m=1}^{\infty} (-i)^m J_m \left[8\pi a \sin\left(\frac{\pi\sigma}{4\Omega}\right) \sin\left(\frac{\pi\mu}{4\Omega}\right)\right] \right. \\ &\times \left. \text{sinc}\left[\left(1 - \left|\frac{\mu}{2\Omega}\right|\right) \frac{m}{2}\right]\right\} \text{rect}\left(\frac{\mu}{4\Omega}\right). \end{aligned} \quad (85)$$

In Fig. 34, for a given row, along the columns we display the variations of the MTF for  $W = 0, 1, 2$ , and  $3$ . For a fixed column, along the rows, we display the variations of the MTF for values of  $\sigma = 0, 8, 16$ , and  $32$ . From Fig. 34, we observe that, by increasing the lateral displacement (between the members of the phase pair), the MTF

Figure 33



Graphical comparison between four different phase profiles, which are useful for extending the depth of field. Three masks have phase variations that follow trigonometric functions. As a reference, we also plot the cubic profile.

has low sensitivity to focus error. Hence, we claim that by controlling the lateral displacement, one can govern the depth of field, without modifying the size of the pupil aperture.

Before ending Section 4, we describe the use of a pair of amplitude masks that are useful for setting a Gaussian spatial filter with adjustable half-width [252].

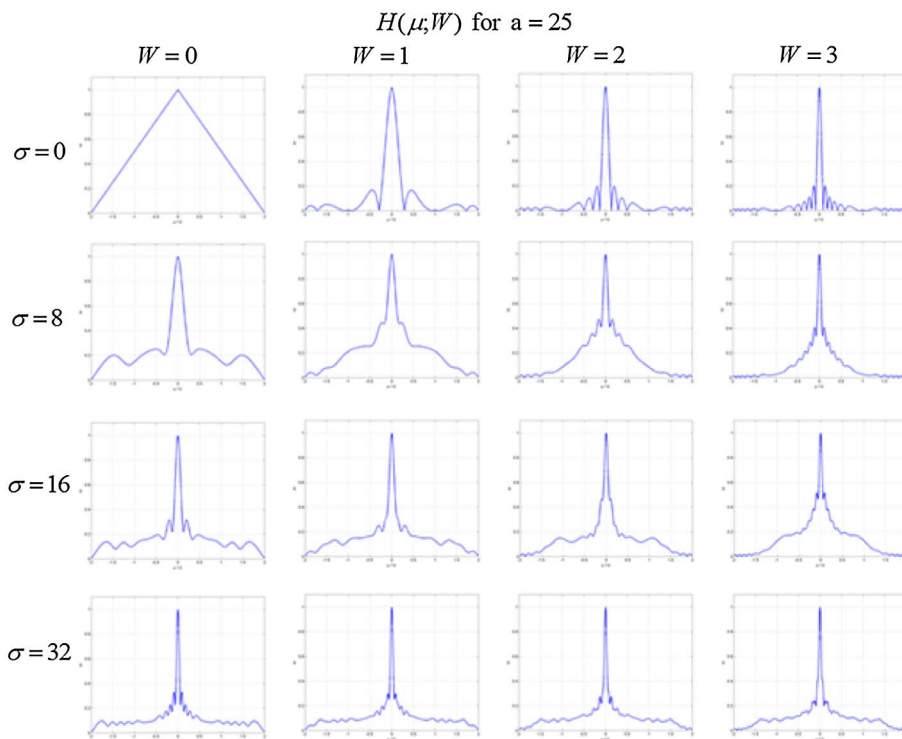
#### 4.4. Tunable Gaussian Mask

For the present task, we use a pair of amplitude masks that are laterally displaced as the Alvarez–Lohmann lenses. The first mask has an amplitude transmittance that is equal to

$$T_1(\nu) = \exp \left\{ -c \left[ 1 + \left( \frac{\nu}{L\Omega} \right)^3 \right] \right\} \text{rect} \left( \frac{\nu}{2L\Omega} \right). \quad (86)$$

In Eq. (86), as before, we use a lowercase letter  $c$  for denoting a dimensionless damping factor of the hyper-Gaussian mask. We have also included a factor  $L > 1$ , for taking into account that the length of the mask is  $L(2\Omega)$ . However, we note that the optical system has a pupil aperture whose length is equal to  $2\Omega$ . Next, in what follows, we indicate that the masks have physically meaningful amplitude transmittances. At the lower edge of the first mask (outside the pupil aperture), the amplitude

**Figure 34**



Array of graphs for describing the evolution of the MTF versus focus error, if one introduces a lateral displacement between the elements forming a phase conjugate pair. As is discussed in the main text, each element has a cosinusoidal phase profile for generating a tunable sinusoidal phase profile. Along the columns of this figure,  $W$  denotes the focus error coefficient in units of wavelength,  $W = W_{2,0}/\lambda$ . The Greek letter  $\sigma$  denotes the amount of lateral displacement between the elements forming the phase pair.

transmittance is  $T_1(-L\Omega) = 1$ , while at the upper edge, outside the pupil aperture, the amplitude transmittance is  $T_1(L\Omega) = \exp(-2c)$ . The amplitude transmittance of the second mask is

$$T_2(\nu) = \exp \left\{ -c \left[ 1 - \left( \frac{\nu}{L\Omega} \right)^3 \right] \right\} \text{rect} \left( \frac{\nu}{2L\Omega} \right). \quad (87)$$

Here, it is convenient to recognize that, at the lower edge of the second mask (beyond the pupil aperture), the amplitude transmittance is  $T_2(-L\Omega) = \exp(-2c)$ , while at the upper edge, outside the pupil aperture, the amplitude transmittance is  $T_2(L\Omega) = 1$ . The two masks working as a pair generate the amplitude transmittance,

$$T(\nu; \sigma) = T_1 \left( \nu + \frac{\sigma}{2} \right) T_2 \left( \nu - \frac{\sigma}{2} \right) \text{rect} \left( \frac{\nu}{2\pi} \right), \quad (88)$$

or, equivalently,

$$T(\nu; \sigma) = \exp \left\{ -2c \left[ 1 + \left( \frac{\sigma}{2L\Omega} \right)^3 \right] \right\} \exp \left\{ - \left( \frac{3c\sigma}{L^3\Omega} \right) \left( \frac{\nu}{\Omega} \right)^2 \right\} \text{rect} \left( \frac{\nu}{2\Omega} \right). \quad (89)$$

In Fig. 35 we depict schematically the use of the above masks, which are already shifted by the spatial frequency  $\sigma$ . From Eq. (89) and from Fig. 35, it is apparent that inside the pupil aperture, the overall amplitude transmittance varies as a Gaussian function.

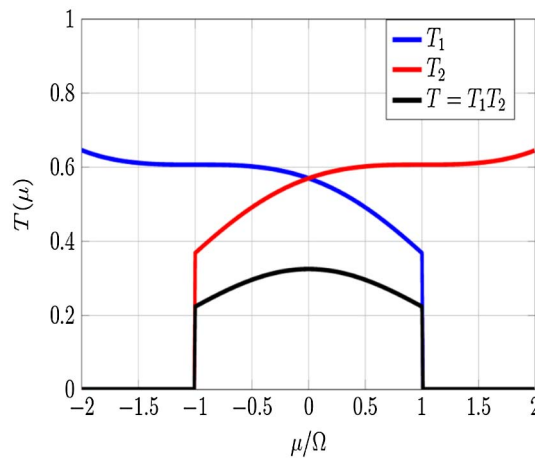
At the center of the pupil, the amplitude transmittance is

$$T(0; \sigma) = \exp \left\{ -2c \left[ 1 + \left( \frac{\sigma}{2L\Omega} \right)^3 \right] \right\}. \quad (90)$$

At the edges of the pupil, the amplitude transmittance is

$$T(\pm\Omega; \sigma) = \exp \left\{ -2c \left[ 1 + \left( \frac{\sigma}{2L\Omega} \right)^3 \right] \right\} \exp \left\{ -3 \frac{c\sigma}{L^3\Omega} \right\}. \quad (91)$$

**Figure 35**



Graphical representation of the technique for generating a Gaussian profile with tunable half-width. The curve in blue represents the amplitude transmittance of the mask in Eq. (86), while the curve in red represents the amplitude transmittance of the mask in Eq. (87). The curve in black is the resultant amplitude transmittance in Eq. (89).

Hence, the width of the Gaussian profile depends linearly with the lateral displacement  $\sigma$ . Thus, by selecting the value of  $\sigma$ , one can govern the amplitude transmittance ratio from the center of the pupil to the edges. That is,

$$\Gamma(\sigma) = \frac{T(0; \sigma)}{T(\pm\Omega; \sigma)} = \exp \left\{ -3 \frac{c\sigma}{L^3\Omega} \right\}. \quad (92)$$

Finally, we recognize that if one uses simultaneously the tunable cubic phase mask and the tunable Gaussian amplitude mask, then one has 2 extra degrees of freedom for setting the preprocessing filter.

In Fig. 36 we show an array of pictures that display the changes of the ambiguity function, as one modifies either the phase delay (columns along the array pictures) or the value of the damping factor (rows along the array of pictures).

Next, we discuss the 2D version of the technique for generating a Gaussian amplitude profile, with tunable half-width, in 2D. For the first mask, the amplitude transmittance is

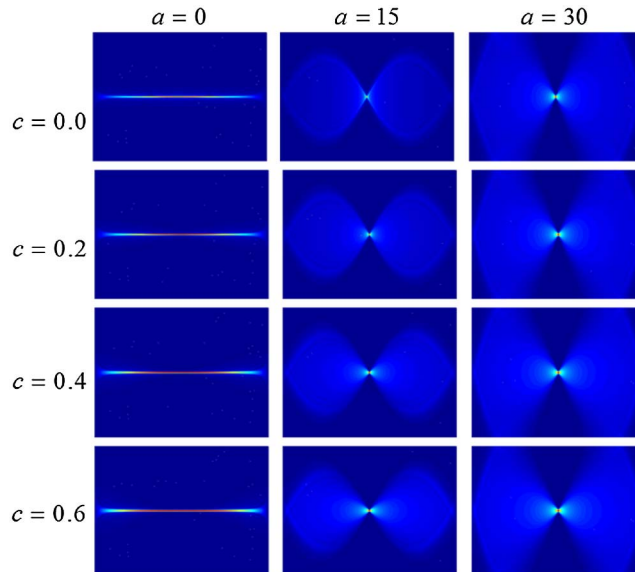
$$T_1(\mu, \nu) = \exp \left\{ -c \left[ 4 + \left( \frac{\mu}{L\Omega} \right)^3 + 3 \left( \frac{\nu}{L\Omega} \right)^2 \left( \frac{\mu}{L\Omega} \right) \right] \right\} \text{rect} \left( \frac{\mu}{2L\Omega} \right) \text{rect} \left( \frac{\nu}{2L\Omega} \right). \quad (93)$$

For the second mask, the amplitude transmittance is

$$T_2(\mu, \nu) = \exp \left\{ -c \left[ 4 - \left( \frac{\mu}{L\Omega} \right)^3 - 3 \left( \frac{\nu}{L\Omega} \right)^2 \left( \frac{\mu}{L\Omega} \right) \right] \right\} \text{rect} \left( \frac{\mu}{2L\Omega} \right) \text{rect} \left( \frac{\nu}{2L\Omega} \right). \quad (94)$$

At the corners of the masks, the amplitude transmittance reaches either the maximum value that is equal to unity, or minimum value that is equal to  $\exp(-8c)$ . Next, we

**Figure 36**



Array of phase-space pictures that display the changes on the modulus of ambiguity functions, which are caused by the use of a tunable cubic mask (whose optical path difference increases along the columns of the array) and the use of tunable Gaussian masks (whose damping coefficient increases along the rows of the array).

place the two mask in contact, and we introduce a lateral displacement  $\sigma$ , between the masks. Hence, the overall amplitude transmittance inside the pupil aperture is

$$T(\mu, \nu; \sigma) = T_1\left(\mu + \frac{\sigma}{2}, \nu\right)T_2\left(\mu - \frac{\sigma}{2}, \nu\right)\text{rect}\left(\frac{\mu}{2\Omega}\right)\text{rect}\left(\frac{\nu}{2\Omega}\right), \quad (95)$$

or equivalently,

$$\begin{aligned} T(\mu, \nu; \sigma) &= \exp\left\{-2c\left[4 + \left(\frac{\sigma}{2L\Omega}\right)^3\right]\right\} \\ &\times \exp\left\{-\left(\frac{3c\sigma}{L^3\Omega}\right)\left[\left(\frac{\mu}{\Omega}\right)^2 + \left(\frac{\nu}{\Omega}\right)^2\right]\right\}\text{rect}\left(\frac{\mu}{2\Omega}\right)\text{rect}\left(\frac{\nu}{2\Omega}\right). \end{aligned} \quad (96)$$

We note from Eq. (96) that, indeed, the overall amplitude transmittance varies, as a 2D Gaussian function inside the pupil aperture, which is a rectangular window. In the following section, we discuss a different method for implementing masks with circular symmetry.

#### 4.5. Vortex Pairs: Phase Masks with Circular Symmetry

Several years ago, out of curiosity, we identified the sufficient and necessary conditions for obtaining self-images in polar coordinates  $(r, \varphi)$ , as is discussed in reference [253]. One of us recognized that the eigenfunctions of the Helmholtz equation are the helicoidally Bessel beams:

$$\psi_{m,n}(r, \theta) = J_n\left(\sqrt{\frac{2\pi r}{\lambda}}\left[1 - \left(\frac{m\lambda}{p}\right)^2\right]\right)\exp(in\theta). \quad (97)$$

In the frequency domain, the eigenfunctions in Eq. (97) are a set of rings, which are known as the Montgomery rings [254]:

$$\Psi_{m,n}(\rho, \varphi) = \frac{(i)^n}{\rho}\delta\left(\rho - \frac{1}{\lambda}\sqrt{\left[1 - \left(\frac{m\lambda}{p}\right)^2\right]}\right)\exp(in\varphi). \quad (98)$$

In Fig. 37 we plot the location of these rings for  $p = M\lambda$  when  $M = 10$ ; hence, the radii are

$$\rho = \frac{1}{p}\sqrt{(M^2 - m^2)}; \quad m = 0, 1, \dots, 9. \quad (99)$$

A particular case of the above eigenfunctions was identified later on, under the name “nondiffracting beam” [255]. As was pointed out in Eq. (30), if one employs the eigensolutions in Eq. (98) with  $n \neq 0$ , then the eigensolutions are able to sustain a dark central spot.

In recent publications, we have revisited the use of helical modulated masks for producing nonconventional radially symmetric focalizers, as well as radially symmetric apodizers [256].

As is schematically depicted in Fig. 38, for implementing radially symmetric, tunable focal devices, we proposed the use of two helically modulated elements, which work as pair. This pair is here called the vortex pair. Here, we consider first the presence of a free-form refractive element, whose complex amplitude transmittance is

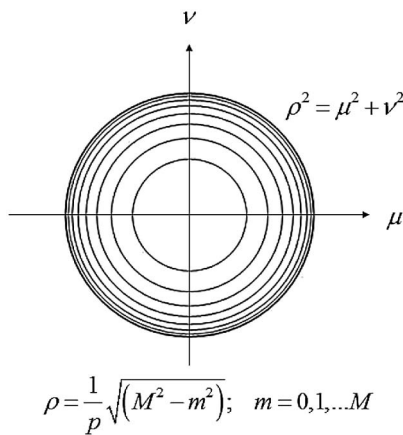
$$T_1(\rho, \varphi) = \exp\{-i2\pi aR(\rho)\varphi\} \text{circ}\left(\frac{\rho}{\Omega}\right). \quad (100)$$

In Eq. (100) the Greek letters  $\rho$  and  $\varphi$  denote the polar coordinates over the pupil aperture, which is located at the Fraunhofer plane of the optical processor in Fig. 38. We represent the finite size of the pupil aperture by using the circ function, which is equal unity if  $\rho \leq \Omega$ . Otherwise, the circ function is equal to zero. At this stage of our discussion, the function  $R(\rho)$  represents any real radial function. The Latin letter  $a$  is the maximum value of the optical path difference. That is,

$$a = (N - 1) \frac{e}{\lambda}. \quad (101)$$

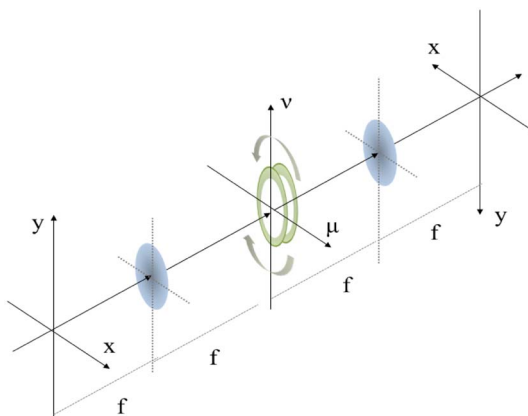
In Eq. (101) the uppercase  $N$  is the value of the refractive index of the material, which is used for building the free-form refractive element. We employ the letter  $e$  for

Figure 37



Schematics describing the geometrical location of the Montgomery rings at the Fraunhofer plane. Each ring is useful for synthesizing one of the eigensolutions in Eq. (98).

Figure 38



Schematics of a classical optical processor that employs a vortex pair at the Fraunhofer diffraction plane. The gray arrows, at the periphery of the circles in green, represent the need of introducing an in-plane between the elements of the pair.

denoting the maximum thickness of the refractive element, and the Greek letter  $\lambda$  represents the wavelength of the optical radiation. Next, we consider a second free-form element whose complex amplitude transmittance is the complex conjugate of Eq. (100). That is,

$$T_2(\rho, \varphi) = \exp\{i2\pi aR(\rho)\varphi\} \text{circ}\left(\frac{\rho}{\Omega}\right). \quad (102)$$

Now, it is convenient to combine the two above refractive elements for setting a vortex pair. If we introduce an in-plane rotation (say by an angle  $\beta$ ) between the elements of the pair, we obtain the following complex amplitude transmittance:

$$T(\rho; \beta) = T_1\left(\rho, \varphi + \frac{\beta}{2}\right) T_2\left(\rho, \varphi - \frac{\beta}{2}\right) = \exp\{-i2\pi(a\beta)R(\rho)\} \text{circ}\left(\frac{\rho}{\Omega}\right). \quad (103)$$

From Eq. (103) we recognize that the complex amplitude transmittance of the vortex pair no longer depends on angle  $\varphi$ . In other words, the complex amplitude transmittance of the vortex pair has only radial variations. Furthermore, it is also apparent from Eq. (103) that angle  $\beta$  controls the maximum value of the optical path difference.

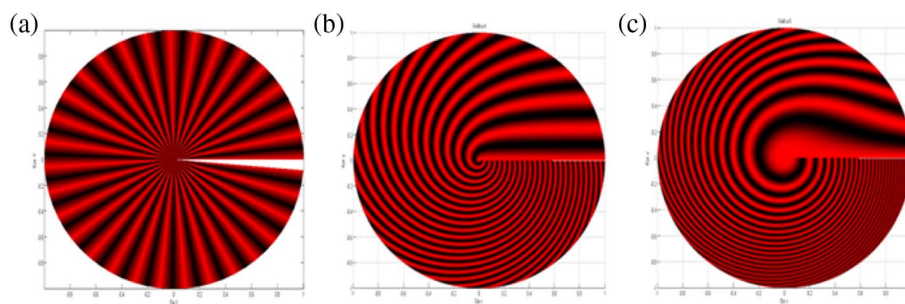
*The above result has truly outstanding consequences. In principle, now one can select any radial phase variation  $R(\rho)$ , and then one can govern its optical path difference; simply by rotating the elements of the vortex pair.* In Fig. 39, we show three interferograms that are associated to three different masks, which have phase profiles with both radial and helical variations. We emphasize here that an important particular case is the implementation of a varifocal lens. To this end, the radial phase variation should be quadratic. that is,  $R(\rho) = (\rho/\Omega)^2$ . Hence, from Eq. (103) we have that

$$\begin{aligned} T(\rho; \beta) &= \exp\left\{-i2\pi(a\beta)\left(\frac{\rho}{\Omega}\right)^2\right\} \text{circ}\left(\frac{\rho}{\Omega}\right) \\ &= \exp\left\{-i\frac{\pi}{\lambda}\left[\frac{2(N-1)e\beta}{h^2}\right]r^2\right\} \text{circ}\left(\frac{\rho}{\Omega}\right). \end{aligned} \quad (104)$$

Then, we recognize that Eq. (104) describes the complex amplitude transmittance of a varifocal lens whose optical power is

$$K(\beta) = \frac{1}{f'} = \left[\frac{2(N-1)e}{h^2}\right]\beta = \beta K_0. \quad (105)$$

Figure 39



Three interferograms obtained by using a plane wave as the reference beam and a probe beam that has both helical variations and radial variations. In (a), the radial function is equal to a constant  $R(\rho) = 1$ . In (b), the radial function describes an axicon  $R(\rho) = (\rho/\Omega)$ . In (c), the radial function represents a lens  $R(\rho) = (\rho/\Omega)^2$ .

The previously discussed simple results are applied next for designing nonconventional zoom systems that use varifocal lenses. However, before that, it is pertinent here to make the following remark about the optical methods for continuously changing the maximum value of the optical path difference in a phase mask.

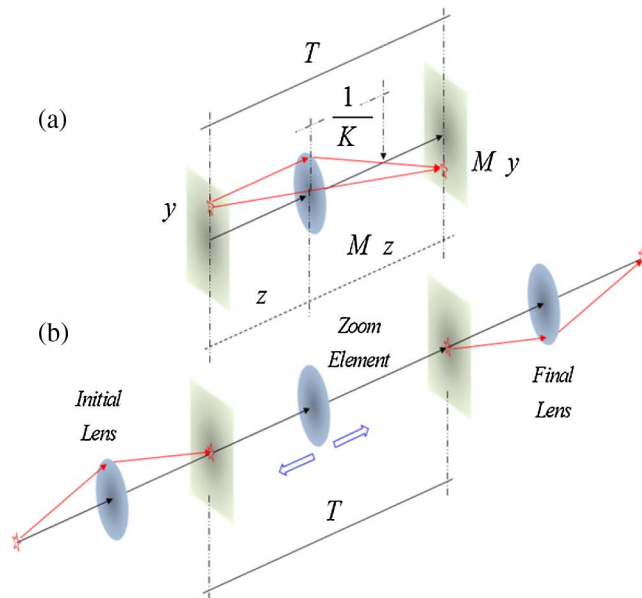
We remember that the first tunable version of the cubic phase mask, as discussed in Section 4.2, is able to control the depth of field without changing the size of the pupil aperture. This tunable phase mask was obtained as an extension of the Lohmann–Alvarez technique. Next, we note that rather recently, Acosta and Bara-Viñas suggested a method that relies on rotating Zernike’s plates [257]. We duly credit Demenikov *et al.* for proposing a tunable phase mask that controls the depth of field by rotating two phase plates [248]. However, we recognize that, on the one hand, the two latter techniques employ masks that have *phase variations expressible in terms of trigonometric functions on the polar angle*. On the other hand, we observe that in the previously discussed vortex pair technique, each mask has *linear phase variations in the polar angle itself*.

## 5. NONCONVENTIONAL ZOOM SYSTEMS

In Fig. 40 we depict schematically the image formation process between two conjugated planes, which are separated by a fixed distance  $T$ . This distance is typically called the throw. It is known that the values of the magnification  $M$  and the throw  $T$  are sufficient for specifying the position of the lens, as well as its optical power [258,259]. The lens should be located at a distance  $z$  from the input plane, such that

$$z = \frac{T}{M - 1}. \quad (106)$$

**Figure 40**



Schematics of an admittedly simplistic version of a single-lens zoom system. In (a), two geometrical optics rays depict the method for identifying the focal length from the values of throw  $T$  and magnification  $M$ . In (b), we illustrate the use of the varifocal lens as a zoom element. In this latter sketch, the input plane is produced by an initial lens, and the output plane is the object plane of a final lens.

Now, for mapping the input plane into the output plane, at a fixed value of  $T$ , the optical power is

$$K = -\frac{(1-M)^2}{TM}. \quad (107)$$

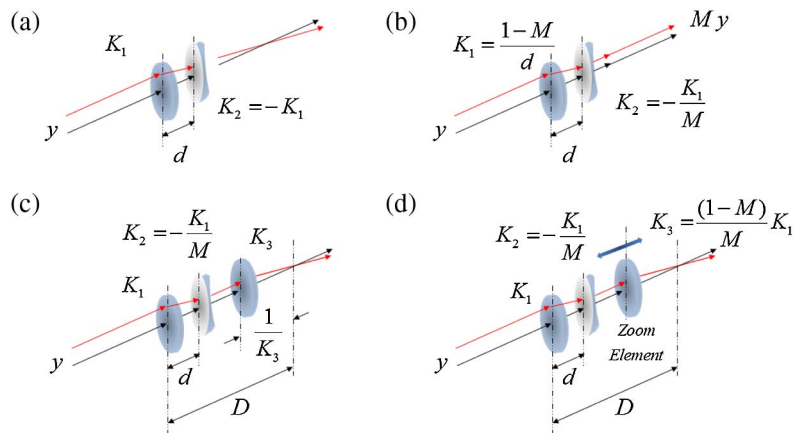
Hence, as depicted in Fig. 40(a), an admittedly simplistic version of a zoom system consists of a single varifocal lens that moves along the optical axis. This simplistic design disrupts the classical notion that a zoom system requires more than one optical element. In this context, we note that, according to Clark [260], a zoom system similar to the one depicted in Fig. 40(b) was patent by Allen [261]; who used as a zoom element a lens with fixed focal length.

From Fig. 40(b) it is apparent that, for Allen's zoom system, the fixed conjugate planes are now the exit plane of the first lens and the entrance plane of the third lens. If the zoom element has a fixed focal length, then one recognizes that there are only two sharp images for a fixed throw. These sharp images have magnification  $M$  and  $1/M$ . Nowadays, one may use Allen's device if the third lens incorporates a mask that extends the depth of field in a manner similar to the proposal in Ref. 262.

Here we suggest using a varifocal lens as the zoom element. In this latter case, for a fixed throw, one can select the desired magnification by properly locating the varifocal lens along the optical axis. At each new axial position, the zoom element must change its optical power, as in Eq. (107).

In what follows, we discuss the Gaussian optics of tunable telephoto objectives, which employ varifocal lenses for achieving tunable magnifications with zero Petzval sum. The optical devices to be discussed are depicted in Fig. 41. We show that some members of this family set of optical devices can also have short back focal lengths and rather low telephoto ratios [263–265]. Next, we focus our attention to the optical system in Fig. 41(a). By employing a positive lens (say with optical power  $K_1$ ) and a negative lens (with optical power  $K_2 = -K_1$ ), one can obtain a telephoto objective that has zero Petzval sum.

Figure 41



Optical devices that employ varifocal lenses for achieving tunable magnification with zero Petzval sum. In (a), we depict a two-element telephoto objective. In (b), we show a telecentric device with governable angular magnification. In (c), we display a design that has low telephoto ratios, while working with fixed values of the distances  $d$  and  $D$ . In (d), we show a variation of the latter device, but now the system has zero Petzval sum.

The composing optical elements are varifocal lenses, which are separated by a fixed distance  $d$ , as is depicted schematically in Fig. 42. It is convenient to express the optical power of the composing varifocal lenses as

$$K_1 = \frac{M_a - 1}{d}; \quad K_2 = -K_1. \quad (108)$$

In Eq. (108),  $M_a$  denotes the angular magnification of the telephoto objective. Trivially, the equivalent optical power is

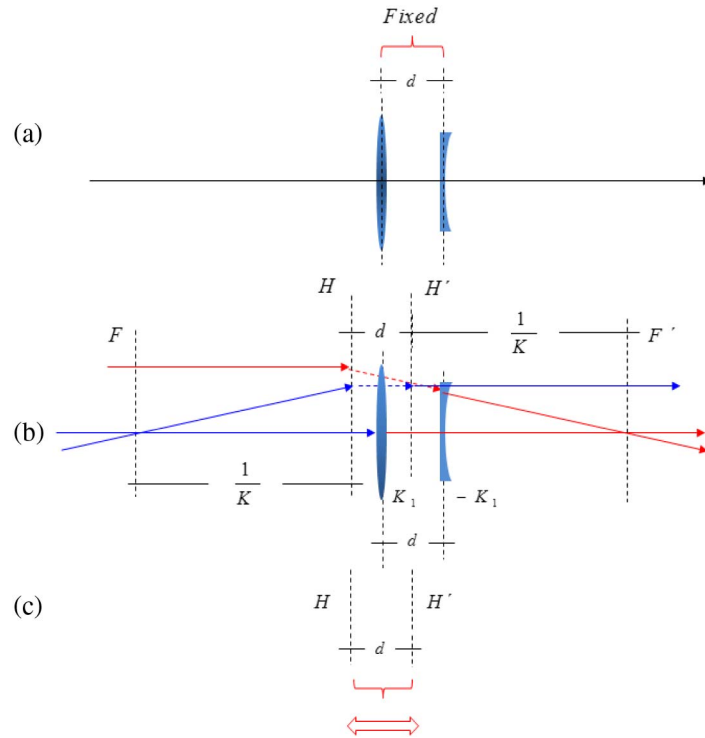
$$K = \frac{1}{f'} = K_1^2 d = \frac{(M_a - 1)^2}{d}. \quad (109)$$

By paraxial ray tracing, one can obtain that the back focal length of the system is

$$f_{\text{back}} = \frac{2 - M_a}{(M_a - 1)^2} d. \quad (110)$$

It is apparent from Eq. (110) and Fig. 43 that, inside the range  $1.3 < M_a < 1.45$ , the back focal length can have small values. Furthermore, if we employ Cox' definition of telephoto ratio [266],  $\mathfrak{R}$ , as well as the results in Eqs. (109) and (110), then we obtain

**Figure 42**

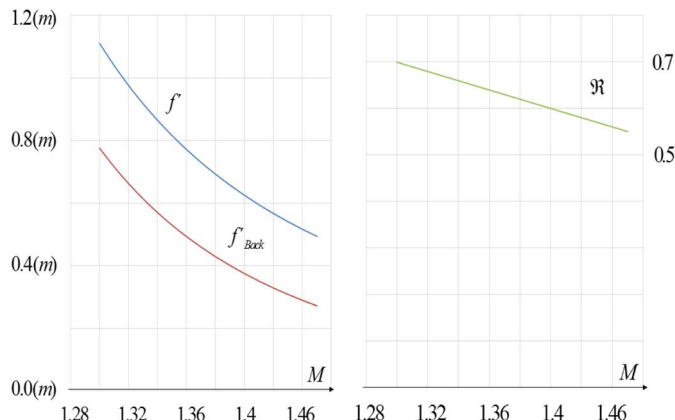


Outline on the use of two varifocal lenses for implementing a tunable telephoto objective. In (a), we show that the lenses have a fixed interlens separation  $d$ . In (b), we display the cardinal planes of the optical system. In (c), we indicate that the separation between the principal planes is always  $d$ . However, by using varifocal lenses, one is able to displace axially the principal planes. Thus, the varifocal lenses surrogate any physical displacement of the constituting elements.

$$\Re = \frac{f_{\text{back}}}{f'} = 2 - M_a. \quad (111)$$

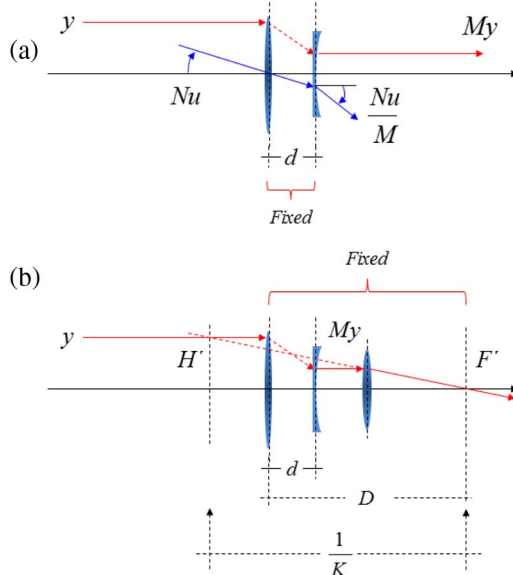
Thus, for realizing low telephoto ratios, one needs to increase the value of  $M_a$ . As depicted at the right-hand side of in Fig. 43, we note that it is feasible to achieve telephoto ratios with values inside the range  $0.55 \leq \Re \leq 0.7$ . Next, we discuss the Gaussian optics design of an afocal system, which is useful for obtaining another type of tunable telephoto objective that also has zero Petzval sum. To our end, we show the schematics of the telescopic system in Fig. 44(a). We note that now the constituting elements are separated by fixed distance  $d$  such that

Figure 43



Gaussian optics characteristics of the telephoto objective in Fig. 42 and Eqs. (109) and (110). For  $d = 0.1$  (m) and inside the interval  $1.3 \leq M_a \leq 1.47$ , we plot the values of the equivalent focal length,  $f'$ , the back focal length, and the telephoto ratio.

Figure 44



Schematics of two optical systems that employ varifocal lenses for implementing (a) an afocal device with tunable angular magnification and (b) a telephoto objective with tunable telephoto ratio and zero Petzval sum.

$$d = \frac{1}{K_1} + \frac{1}{K_2}. \quad (112)$$

Next, we recognize that the first optical system transforms an incoming parallel beam into another parallel beam, with a compression ratio equal to  $M$ , where

$$M = \frac{y_2}{y_1} = \frac{K_1}{K_2}. \quad (113)$$

Of course, the angular magnification of the afocal device is equal to  $1/M$ . From Eqs. (112) and (113) we obtain the optical powers that are needed when one changes the magnification  $M$ , for a fixed value of  $d$ ,

$$K_1 = \frac{1-M}{d}; \quad K_2 = -\frac{1-M}{Md}. \quad (114)$$

Hence, even when the separation between the two varifocal lenses is constant, the afocal system can change continuously its angular magnification. Next, we address our attention to the optical system in Fig. 44(b). In what follows we show that the previously discussed afocal device can be transformed into a telephoto objective with the following features: the magnification is tunable, the optical device has zero Petzval sum, and one can obtain rather low telephoto ratios. From Fig. 44(b) and Eq. (114) we note that the telephoto objective can have zero Petzval sum if the optical power of the third element is

$$K_3 = \frac{(1-M)^2}{Md} = \frac{(1-M)}{M} K_1. \quad (115)$$

Trivially, the back focal length of the optical system is  $1/K_3$ . The equivalent optical power of the system is

$$K = MK_3 = \frac{(1-M)^2}{d}. \quad (116)$$

As before, we use the Cox definition of telephoto ratio and the results in Eqs. (115) and (116) to obtain

$$\mathfrak{R} = \frac{f_{\text{back}}}{f'} = \frac{K}{K_3} = M. \quad (117)$$

It is apparent from Eq. (117) that one can achieve very low values of telephoto ratios if  $M \ll 1$ . Finally, by paraxial ray tracing, we recognize that the field of view ( $N_0 \bar{u}_0$ ) is limited by the maximum height,  $\bar{y}_3$ , of the third optical element; that is,

$$N_0 \bar{u}_0 = K \bar{y}_3 = \frac{(1-M)^2}{d} \bar{y}_3. \quad (118)$$

In the same context, we notice that the separation between the second component and the third component can have reasonable values. For illustrating this point, we evaluate the values of  $K_1 d$ ,  $K_2 d$ ,  $K_3 d$ , and  $K d$ , as well as the ratio

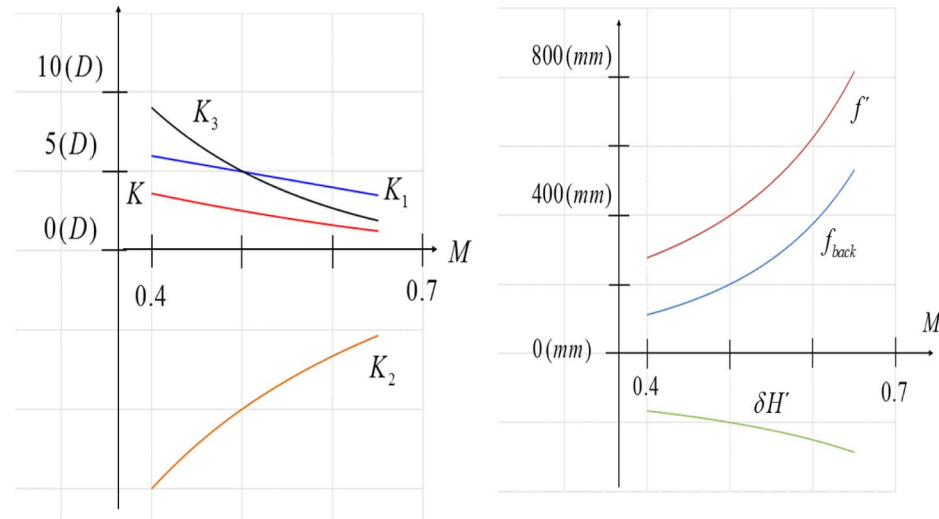
$$\frac{\delta H'}{d} = \frac{1}{1-M}. \quad (119)$$

Our results are plotted in Fig. 45 in the range  $0.4 < M < 0.7$ . From Fig. 45 it follows that the equivalent optical power changes linearly, in proportion to the variations of  $K_1$ . We observe that if the desired magnification is in the range  $0.4 \leq M \leq 0.5$ , then the back focal length has values in the interval 50 (mm)–200 (mm). Since the equivalent focal length has values in the interval 150 (mm)–400 (mm), then one can achieve telephoto ratios that are less than or equal to 0.5.

The characteristics of the above proposed optical devices are conveniently summarized in Table 3. It is relevant to note that it may appear cumbersome to have an optical system that simultaneously changes its optical power and its location along the optical axis. However, in addition to adaptive optics [267–275], some optical designers have already directed their attention to the incorporation of new types of varifocal lenses into nonconventional optical systems [276–280]. Hence, one can foresee that other types of governable optical elements, such as tunable axicons and controllable phase rendering techniques, will be considered in future imaging devices [281–283].

Before ending the current paper, it is relevant to recognize that few contributions have considered the impact of noise levels when extending the depth of field. The presence of noise reduces the effectiveness of applying simple inverse filtering techniques that are part of the methods for extending the depth of field.

**Figure 45**



Gaussian optics characteristics of the device in Fig. 43(b) for  $d = 0.1$  (m), in the interval  $0.4 \leq M \leq 0.6$ . At the left-hand side, we plot the values of  $K_1$ ,  $K_2$ ,  $K_3$ , and  $K$ . At the right-hand side, we plot  $f_{\text{back}} = 1/K_3$ ,  $f' = 1/K$ , and  $\delta H'$ .

**Table 3. Simple Optical Systems That Employ Varifocal Lenses for Implementing Devices with Tunable Magnification<sup>a</sup>**

	Constraint	Optical Power	Axial Displacement	$P = \text{Petzval Sum}$
Single-lens zoom system	$T$	$K = -(1 - M)^2/MT$	$\delta z \neq 0$	$P \neq 0$
Two-lens afocal system	$d$	$K = 0$	$\delta z \neq 0$	$P \neq 0$
Two-lens telephoto objective	$d$	$K = (1 - M)^2/d$	$\delta z \neq 0$	$P = 0$
Three-lens telephoto objective	$d$ and $D$	$K = (1 - M)^2/d$	$\delta z = 0$	$P \neq 0$
Three-lens telephoto objective	$d$ and $D$	$K = (1 - M)^2/d$	$\delta z \neq 0$	$P = 0$

<sup>a</sup>Along the first column, we list the number of optical elements. Along the second column, we list the physical constraints. Along the third column, we list the equivalent optical power. Along the fourth and the fifth columns, we indicate if the system requires an axial displacement and if the Petzval sum is equal to zero, respectively.

## 6. CONCLUSIONS

Summarizing, based on scalar diffraction, we have discussed a simple comprehensive treatment of the methods for increasing focal depth, as well as for controlling the influence of focus error on the MTF, for an optical system working at full pupil aperture. Our discussion includes a review of the methods for designing tunable amplitude masks and tunable phase masks that extend the depth of field, and of the use of varifocal lenses for designing nonconventional optical devices.

Aiming for a simple heuristic narrative, we have included a large set of schematic diagrams that help to visualize the influence of certain masks, and nonconventional optical windows, on the OTF. Figure captions are closely related to the descriptions within the text, while avoiding replication. Our schematic diagrams depict the basic characteristics of linear optical systems, phase-space representations, and the use of geometrical optics rays. We have refrained ourselves from presenting only sets of fancy digitally processed images.

In the first part of our discussion, we have shown the usefulness of performing an angular averaging operation on a 2D mask, if you will, for obtaining the zero-order circular harmonic. This operation is convenient for describing as a 1D Fourier transformation the axial behavior of an optical system. *This remarkably simple result was here applied for discussing the use of masks that reduce the sidelobes of the axial impulse response. At the same time, these masks spread the main lobe of the axial impulse response. In this manner, one can reduce the tolerance of focus error associated to the Strehl ratio, or, equivalently, one can increase focal depth.*

In the second part of our discussion, we have related the use of masks for controlling the impact of focus error on the MTF, with the use of the ambiguity function as is employed in radar engineering. *We have used a Taylor series expansion of the ambiguity function for identifying symmetric conditions on the generalized pupil function, which lead to MTFs with low sensitivity to focus errors. This symmetry condition is extremely useful for initiating the search for suitable masks that reduce the impact of focus error on the MTF.*

In the third part of our discussion, we have noted that, for evaluating the ambiguity function, the integrand in the Fourier transform resembles the physical arrangement of the Lohmann–Alvarez phase pair. This undeniably naïve, yet very useful, approach was applied for proposing *adjustable phase masks or, if you will, tunable phase masks, which are able to govern the depth of field without changing the size of the pupil aperture.*

Furthermore, we have noted that phase masks able to reduce the influence of focus error also generate spurious oscillation in the MTF. Hence, we have argued in favor of using amplitude masks with moderate absorption. *We have shown that amplitude masks can reduce the unwanted oscillations on the MTF.* In the same context, we have shown that two suitable amplitude masks, working as a pair, are able generate a *Gaussian attenuation filter, with tunable half-width.*

Next, we have pointed out that the out-of-focus OTF is never equal to the in-focus OTF. In other words, *strictly speaking, there is no OTF invariance.* However, provided that one employs a suitable pupil mask, the square value of the difference between the out-of-focus OTF and the in-focus OTF can have rather small values within a certain range of values of the focus error coefficient  $W_{2,0}$ .

This later result has practical consequences when stipulating tolerances between the square value of the difference between the out-of-focus OTF and the in-focus OTF for a given range of values of  $W_{2,0}$ . For example, inside the range  $0 \leq W_{2,0} \leq 3\lambda$ , the

*square modulus of the difference between the out-of-focus OTF and the in-focus OTF has negligible values, if one uses a hyper-Gaussian absorption mask with screens having fractional order phase profiles.*

In the fourth part of our discussion, we have considered *vortex pupil masks*, which have an overall complex amplitude transmittance different from zero, but its angular average (or, if you will, its zero-order circular harmonic) is equal to zero. *Thus, we have indicated that vortex pupil masks are able to sustain an axial irradiance distribution that is equal to zero.*

Next, we have noted that one can arrive to the concept of vortex pairs by exploiting Lohmann's proposal for generating tunable zone plates. We have shown that *vortex pairs are useful for implementing a large family of tunable focalizers*. As a particular example, we have indicated that *vortex pairs are particularly useful, but are not limited, for implementing varifocal lenses*. We have indicated that, for the elements forming a vortex pairs, *their phases are linear functions of the azimuthal angle*. In this context, we have discussed the use of other types of phase-only masks that have profiles expressible in terms of trigonometric functions.

In the fifth part of our discussion, we have described *the use of varifocal lenses for designing a nonconventional zoom system. We have discussed the Gaussian optics characteristic of a telecentric device with tunable magnification, as well as that of two telephoto objectives with variable magnification and very low telephoto ratios*. We have indicated that, for the two telephoto objectives, one can have optical systems with zero Petzval sum. Even though it may appear cumbersome to have an optical system that *simultaneously changes its optical power and its location along the optical axis*, we have indicated that some optical designers have already directed their attention to the incorporation of new types of varifocal lenses for proposing nonconventional optical systems.

In addition to adaptive optics, we have noted that there are currently several competing techniques for implementing varifocal lenses. We have extrapolated this trend by indicating that future optical systems may incorporate nonconventional tunable devices that will work at full pupil aperture when recording optical images. Once the images are recorded, and before the images are displayed, future digital processors will work in real time for presenting meaningful pictures to human observers.

## APPENDIX A

The Greek letter  $\mu$  denotes a variable in the frequency domain. We employ the Greek letter  $\Omega$  for denoting the cut-off spatial frequency. We describe the pupil aperture by the rectangular function  $\text{rect}(\mu/2\Omega)$ . We assume that in the frequency domain there is a set of complex valued functions,  $\Phi_n(\mu)$ , that form a complete, orthonormal set of functions with weight function  $W(\mu)$ . Then,

$$\int_{-\infty}^{\infty} \Phi_m(\mu) W(\mu) \Phi_n^*(\mu) d\mu = \delta_{m,n}. \quad (\text{A1})$$

In Eq. (A1) we employ the standard definition of a scalar product in a Hilbert space. The symbol  $\delta_{m,n}$  represents Kronecker's delta. Following Dirac's original proposal on bra vectors, we define  $\Psi_n(\mu) = W(\mu) \Phi_n(\mu)$ , where  $W(\mu)$  is the weight function. Trivially, if  $W(\mu) = 1$ , then  $\Psi_n(\mu) = \Phi_n(\mu)$ . These latter functions are the ket vectors.

Next, we assume that if, at the frequency domain, the complex amplitude transmittance is equal to the function  $\Psi_n(\mu) = W(\mu) \Phi_n(\mu)$ , then at the output plane the diffraction pattern has a complex amplitude distribution equal to

$$\psi_m(x) = \int_{-\infty}^{\infty} \Psi_m(\mu) \exp\{i2\pi x\mu\} d\mu. \quad (\text{A2})$$

It is convenient now to recognize the following result. For representing mathematically the bandlimited version of a point source, one can employ the closure property of a Hilbert space:

$$\delta(\mu - \nu) = \sum_{m=0}^{\infty} C_m(\nu) \Psi_m(\mu). \quad (\text{A3})$$

In Eq. (A3), the coefficient is

$$C_m(\nu) = \int_{-\infty}^{\infty} \delta(\mu - \nu) \Phi_m^*(\mu) d\mu = \Phi_m^*(\nu). \quad (\text{A4})$$

Hence, one has that

$$\delta(\mu - \nu) = \sum_{m=0}^{\infty} \Phi_m^*(\nu) \Psi_m(\mu). \quad (\text{A5})$$

In what follows, we note that, by taking the Fourier transform of Eq. (A5), one obtains an expression that describes the bandlimited version of a tilted, plane wavefront:

$$\exp\{i2\pi\nu x\} = \sum_{m=0}^{\infty} \Phi_m^*(\nu) \psi_m(x). \quad (\text{A6})$$

By setting  $\nu = 0$ , we obtain that

$$1 = \sum_{m=0}^{\infty} \Phi_m^*(0) \psi_m(x). \quad (\text{A7})$$

In the main text we employ Eq. (A7) for stating the condition for achieving an arbitrarily extended depth of focus; that is,

$$S(\zeta) = \sum_{m=0}^M \Phi_m^*(0) \Psi_m(\zeta) \text{rect}(\zeta). \quad (\text{A8})$$

Then, by increasing the number of terms,  $M$ , one expects to achieve an extended depth of focus; that is,

$$I_S(W) = \frac{\left| \sum_{n=0}^N \Phi_n^*(0) \psi_n(W) \right|^2}{\left| \sum_{n=0}^N \Phi_n^*(0) \psi_n(0) \right|^2} \approx 1. \quad (\text{A9})$$

We include this appendix for the sake of completeness of the present paper.

## APPENDIX B

Here we note that, by substituting Eq. (82) into Eq. (83), one obtains that

$$\begin{aligned} H(\mu; \sigma; W_{2,0}) &= \int_{-\infty}^{\infty} \exp \left\{ i2\pi \left[ 4a \sin\left(\frac{\pi\sigma}{4\Omega}\right) \sin\left(\frac{\pi\mu}{4\Omega}\right) \right] \cos\left(\frac{\pi\nu}{2\Omega}\right) \right\} \\ &\times \exp \left\{ i2\pi \left( \frac{2W_{2,0}\mu}{\lambda\Omega^2} \right) \nu \right\} \diamond(\mu; \nu; \Omega) d\nu. \end{aligned} \quad (\text{B1})$$

Next, we recognize that by using the Jacobi–Anger expansion, one can rewrite Eq. (B1) as

$$\begin{aligned} H(\mu; \sigma; W_{2,0}) &= \sum_{m=-\infty}^{\infty} (-i)^m J_m \left[ 8\pi a \sin\left(\frac{\pi\sigma}{4\Omega}\right) \sin\left(\frac{\pi\mu}{4\Omega}\right) \right] \\ &\quad \times \int_{-\infty}^{\infty} \exp\left\{ i2\pi\left(\frac{2W_{2,0}\mu}{\lambda\Omega^2} - \frac{m}{4\Omega}\right)\nu \right\} \diamond(\mu; \nu; \Omega) d\nu. \end{aligned} \quad (\text{B2})$$

If one performs the integral operation in Eq. (B2), one obtains

$$\begin{aligned} H(\mu; \sigma; W_{2,0}) &= \left(1 - \left|\frac{\mu}{2\Omega}\right|\right) \sum_{m=-\infty}^{\infty} (-i)^m J_m \left[ 8\pi a \sin\left(\frac{\pi\sigma}{4\Omega}\right) \sin\left(\frac{\pi\mu}{4\Omega}\right) \right] \\ &\quad \times \operatorname{sinc}\left\{ \left(1 - \left|\frac{\mu}{2\Omega}\right|\right) \left[ 8\left(\frac{W_{2,0}}{\lambda}\right) \left(\frac{\mu}{2\Omega}\right) - \frac{m}{2} \right] \right\} \operatorname{rect}\left(\frac{\mu}{4\Omega}\right). \end{aligned} \quad (\text{B3})$$

Equation (B3) is to be recognized as Eq. (84) in the main text. Trivially, if in Eq. (B3) we set  $\mu = 0$ , then  $H(0; \sigma; W_{2,0}) = 1$ , and by setting  $\mu = 2\Omega$ , one has then  $H(2\Omega; \sigma; W_{2,0}) = 0$ . Furthermore, if  $\sigma = 0$ , then Eq. (B3) reduces to the out-of-focus OTF associated to clear pupil aperture:

$$H(\mu; \sigma; W_{2,0}) = \left(1 - \left|\frac{\mu}{2\Omega}\right|\right) \operatorname{sinc}\left\{ \left(1 - \left|\frac{\mu}{2\Omega}\right|\right) \left[ 8\left(\frac{W_{2,0}}{\lambda}\right) \left(\frac{\mu}{2\Omega}\right) \right] \right\} \operatorname{rect}\left(\frac{\mu}{4\Omega}\right). \quad (\text{B4})$$

Finally, for the proposed phase conjugated pair, we note that Eq. (B3) contains the in-focus OTF,  $W_{2,0} = 0$ , which is equal to

$$\begin{aligned} H(\mu; \sigma; 0) &= \left(1 - \left|\frac{\mu}{2\Omega}\right|\right) \sum_{m=-\infty}^{\infty} (-i)^m J_m \left[ 8\pi a \sin\left(\frac{\pi\sigma}{4\Omega}\right) \sin\left(\frac{\pi\mu}{4\Omega}\right) \right] \\ &\quad \times \operatorname{sinc}\left\{ \left(1 - \left|\frac{\mu}{2\Omega}\right|\right) \frac{m}{2} \right\} \operatorname{rect}\left(\frac{\mu}{4\Omega}\right). \end{aligned} \quad (\text{B5})$$

The result in Eq. (B5) is expressed as Eq. (85) in the main text.

## FUNDING

CoNaCyT, research project 157673 (CA40120112).

## ACKNOWLEDGMENT

We are truly indebted to reviewers for their useful suggestions. We would like to thank Sergio Ledesma, Emmanuel Yepez-Vidal and Eloy Garcia-Almanza for helping us to generate several figures.

## REFERENCES

1. R. J. Pieper and A. Korpel, “Image processing for extended depth of field,” *Appl. Opt.* **22**, 1449–1453 (1983).
2. J. Ojeda-Castañeda, L. R. Berriel Valdos, and E. L. Montes, “Line spread function relatively insensitive to defocus,” *Opt. Lett.* **8**, 458–460 (1983).
3. J. Ojeda-Castañeda, “Focus error operator and related special functions,” *J. Opt. Soc. Am.* **73**, 1042–1047 (1983).
4. G. Haeusler and E. Koerner, “Simple focusing criterion,” *Appl. Opt.* **23**, 2468–2469 (1984).

5. G. Indebetouw and H. Bai, "Imaging with a Fresnel zone pupil masks: extended depth of field," *Appl. Opt.* **23**, 4299–4302 (1984).
6. C. Varamit and G. Indebetouw, "Imaging properties of defocused partitioned pupils," *J. Opt. Soc. Am. A* **2**, 799–802 (1985).
7. Z. S. Hegedus, "Annular pupil arrays-application to confocal scanning," *Opt. Acta* **32**, 815–826 (1985).
8. J. Ojeda-Castañeda, L. R. Berriel Valdos, and E. Montes, "Spatial filter for increasing the depth of focus," *Opt. Lett.* **10**, 520–522 (1985).
9. J. E. Villeneuve, A. Boivin, and S. C. Biswas, "L'image tridimensionnelle du point en présence d'aberration sphérique primaire et de filtrage d'amplitude: unitaire ou modal," *Can. J. Phys.* **63**, 287–300 (1985).
10. J. P. Mills and B. J. Thompson, "Effect of aberrations and apodization on the performance of coherent optical systems. I. The amplitude impulse response," *J. Opt. Soc. Am. A* **3**, 694–703 (1986).
11. J. P. Mills and B. J. Thompson, "Effect of aberrations and apodization on the performance of coherent optical systems. II: Imaging," *J. Opt. Soc. Am. A* **3**, 704–716 (1986).
12. J. Ojeda-Castañeda, P. Andrés, and A. Díaz, "Objects that exhibit high focal depth," *Opt. Lett.* **11**, 267–269 (1986).
13. L. N. Hazra and A. Guha, "Far-field diffraction properties of radial Walsh filters," *J. Opt. Soc. Am. A* **3**, 843–846 (1986).
14. T. C. Poon and M. Motamedi, "Optical-digital incoherent image processing for extended depth of field," *Appl. Opt.* **26**, 4612–4615 (1987).
15. K. Engelhardt and G. Haeusler, "Acquisition of 3-D data by focus sensing," *Appl. Opt.* **27**, 4684–4689 (1988).
16. A. W. Lohmann, "Scaling laws for lens systems," *Appl. Opt.* **28**, 4996–4998 (1989).
17. J. G. Baker, "Zoom lens," U.S. patent 4,925,281 (May 15, 1990).
18. A. Kolodziejczyk, S. Bard, Z. Jaroszewicz, and M. Sypek, "The light sword optical element-a new diffractive structure with extended depth of focus," *J. Mod. Opt.* **37**, 1283–1286 (1990).
19. N. Davidson, A. A. Friesem, and E. Hasman, "Holographic axilens: high resolution and long focal depth," *Opt. Lett.* **16**, 523–525 (1991).
20. T. Dresel, G. Haeusler, and H. Venzke, "Three-dimensional sensing of rough surfaces by coherence radar," *Appl. Opt.* **31**, 919–925 (1992).
21. J. Sochacki, A. Kotodziejczyk, Z. Jaroszewicz, and S. Bara, "Nonparaxial design of generalized axicons," *Appl. Opt.* **31**, 5326–5330 (1992).
22. J. Sochacki, S. Bara, Z. Jaroszewicz, and A. Kołodziejczyk, "Phase retardation of the uniform-intensity axilens," *Opt. Lett.* **17**, 7–9 (1992).
23. J. Ojeda-Castañeda, G. Saavedra, and E. López-Olazagasti, "Supergaussian beams of continuous order as grin modes," *Opt. Commun.* **102**, 21–24 (1993).
24. R. M. Gonzalez, J. Linares, and C. Gomez-Reino, "Gradient-index axicon lenses: a quasi-geometrical study," *Appl. Opt.* **33**, 3420–3426 (1994).
25. A. W. Lohmann and B. H. Soffer, "Relationships between the Radon-Wigner and fractional Fourier transforms," *J. Opt. Soc. Am. A* **11**, 1798–1801 (1994).
26. L. N. Hazra, Y. Han, and C. A. Delisle, "Kinoform lenses: Sweatt model and phase function," *Opt. Commun.* **117**, 31–36 (1995).
27. C. J. R. Sheppard, "Leaky annular pupils for improved axial imaging," *Optik* **99**, 32–34 (1995).
28. J. van der Gracht, E. W. Dowski, M. G. Taylor, and D. M. Deaver, "Broadband behavior of an optical-digital focus-invariant system," *Opt. Lett.* **21**, 919–921 (1996).

29. M. Levoy and P. Hanrahan, "Light field rendering," in *Proceedings of SIGGRAPH* (1996), pp. 31–42.
30. C. Parigger, Y. Tang, D. H. Plemmons, and J. W. L. Lewis, "Spherical aberration effects in lens-axicon doublets: theoretical study," *Appl. Opt.* **36**, 8214–8221 (1997).
31. S. Bradburn, W. T. Cathey, and E. R. Dowski, "Realizations of focus invariance in optical-digital systems with wave-front coding," *Appl. Opt.* **36**, 9157–9166 (1997).
32. L. N. Hazra and C. A. Delisle, "Primary aberrations of a thin lens with different object and image space media," *J. Opt. Soc. Am. A* **15**, 945–953 (1998).
33. H. Farid and E. Simoncelli, "Range estimation by optical differentiation," *J. Opt. Soc. Am. A* **15**, 1777–1786 (1998).
34. R. Piestun, B. Spektor, and J. Shamir, "Pattern generation with extended focal depth," *Appl. Opt.* **37**, 5394–5398 (1998).
35. H. B. Wach, E. R. Dowski, Jr., and W. T. Cathey, "Control of chromatic focal shift through wavefront coding," *Appl. Opt.* **37**, 5359–5367 (1998).
36. J. Ojeda-Castañeda and A. Castro, "Simultaneous Cartesian coordinate display of defocused optical transfer functions," *Opt. Lett.* **23**, 1049–1051 (1998).
37. J. Ojeda-Castañeda and A. Saucedo, "Tunable focal depth by random superposition," *Opt. Mem. Neural Netw.* **8**, 81–86 (1999).
38. I. Leiserson, S. G. Lipson, and V. Sarafis, "Superresolution in far-field imaging," *Opt. Lett.* **25**, 209–211 (2000).
39. G. Boyer and V. Sarafis, "Two pinhole superresolution using spatial filters," *Optik* **4**, 177–179 (2000).
40. W. Chi and N. George, "Electronic imaging using a logarithmic asphere," *Opt. Lett.* **26**, 875–877 (2001).
41. S. S. Sherif, E. R. Dowski, and W. T. Cathey, "A logarithmic phase filter to extend the depth of field of incoherent hybrid imaging systems," *Proc. SPIE* **4471**, 272–280 (2001).
42. H. Wang and F. Gan, "High focal depth with a pure-phase apodizers," *Appl. Opt.* **40**, 5658–5662 (2001).
43. T. Naemura, T. Yoshida, and H. Harashima, "3-D computer graphics based on integral photography," *Opt. Express* **8**, 255–262 (2001).
44. G. Boyer, "New class of axially apodizing filters for confocal scanning microscopy," *J. Opt. Soc. Am. A* **19**, 584–589 (2002).
45. S. Sanyal and A. Ghosh, "High tolerance to spherical aberrations and defects of focus with a birefringent lens," *Appl. Opt.* **41**, 4611–4618 (2002).
46. H. Wang and F. Gan, "Phase-shifting apodizers for increasing focal depth," *Appl. Opt.* **41**, 5263–5266 (2002).
47. M. Martinez-Corral, A. Pons, and M. T. Caballero, "Axial apodization in 4Pi-confocal microscopy by annular binary filters," *J. Opt. Soc. Am. A* **19**, 1532–1536 (2002).
48. N. George and W. Chi, "Extended depth of field using a logarithmic asphere," *J. Opt. A* **5**, S157–S163 (2003).
49. S. Mezouari and A. R. Harvey, "Phase pupil functions for reduction of defocus and spherical aberrations," *Opt. Lett.* **28**, 771–773 (2003).
50. X. Liu, X. Cai, S. Chang, and C. P. Grover, "Optical system having large focal depth for distant object tracking," *Opt. Express* **11**, 3242–3247 (2003).
51. S. Prasad, T. Torgersen, V. Pauca, R. Plemmons, and J. van der Gracht, "Engineering the pupil phase to improve image quality," *Proc. SPIE* **5108**, 1–12 (2003).

52. S. Mezouari and A. R. Harvey, "Combined amplitude and phase filters for increased tolerance to spherical aberration," *J. Mod. Opt.* **50**, 2213–2220 (2003).
53. S. R. Marschner, H. W. Jensen, M. Cammarano, S. Worley, and P. Hanrahan, "Light scattering from human hair fibers," *ACM Trans. Graph.* **22**, 780–791 (2003).
54. S. S. Sherif, W. T. Cathey, and E. R. Dowski, "Phase plate to extend the depth of field of incoherent hybrid imaging systems," *Appl. Opt.* **43**, 2709–2721 (2004).
55. S. Stallinga, "Light distribution close to focus in biaxially birefringent media," *J. Opt. Soc. Am. A* **21**, 1785–1798 (2004).
56. M. Yun, L. Liu, J. Sun, and D. Liu, "Transverse or axial superresolution with radial birefringent filter," *J. Opt. Soc. Am. A* **21**, 1869–1874 (2004).
57. M. Levoy, B. Chen, V. Vaish, M. Horowitz, I. McDowall, and M. Bolas, "Synthetic aperture confocal imaging," *ACM Trans. Graph.* **23**, 825–831 (2004).
58. X. Liu, X. Cai, S. Chang, and C. P. Grover, "Cemented doublet lens with an extended focal depth," *Opt. Express* **13**, 552–557 (2005).
59. X. Gao, Z. Fei, W. Xu, and F. Gan, "Tunable three-dimensional intensity distribution by a pure phase-shifting apodizer," *Appl. Opt.* **44**, 4870–4873 (2005).
60. G. Muyo and A. R. Harvey, "Decomposition of the optical transfer function: wavefront coding imaging systems," *Opt. Lett.* **30**, 2715–2717 (2005).
61. W. Chi and N. George, "Integrated imaging with a centrally obscured logarithmic asphere," *Opt. Commun.* **245**, 85–92 (2005).
62. I. Golub, "Fresnel axicon," *Opt. Lett.* **31**, 1890–1892 (2006).
63. S. Abrahamsson, S. Usawab, and M. Gustafsson, "A new approach to extended focus for high-speed, high-resolution biological microscopy," *Proc. SPIE* **6090**, 60900N (2006).
64. M. Levoy, R. Ng, A. Adams, M. Footer, and M. Horowitz, "Light field microscopy," in *Proceedings of ACM SIGGRAPH* (2006), pp. 924–934.
65. R. Raskar, A. Agrawal, and J. Tumblin, "Coded exposure photography: motion deblurring via fluttered shutter," in *Proceedings of SIGGRAPH* (2006), pp. 795–804.
66. A. Greengard, Y. Y. Schechner, and R. Piestun, "Depth from diffracted rotation," *Opt. Lett.* **31**, 181–183 (2006).
67. E. Ben-Eliezer, E. Marom, N. Konforti, and Z. Zalevsky, "Radial mask for imaging systems that exhibit high resolution and extended depths of field," *Appl. Opt.* **45**, 2001–2013 (2006).
68. M. Somayaji and M. P. Christensen, "Enhancing form factor and light collection of multiplex imaging systems by using a cubic phase mask," *Appl. Opt.* **45**, 2911–2923 (2006).
69. Z. Zalevsky, A. Shemer, A. Zlotnik, E. B. Eliezer, and E. Marom, "All-optical axial super resolving imaging using a low-frequency binary-phase mask," *Opt. Express* **14**, 2631–2643 (2006).
70. S. Mezouari, G. Muyo, and A. R. Harvey, "Circularly symmetric phase filters for control of primary third-order aberrations: coma and astigmatism," *J. Opt. Soc. Am. A* **23**, 1058–1062 (2006).
71. S. Bernet, A. Jesacher, S. Fuerhapter, C. Maurer, and M. Ritsch-Marte, "Quantitative imaging of complex samples by spiral phase contrast microscopy," *Opt. Express* **14**, 3792–3805 (2006).
72. A. Dorrrington, M. Cree, A. Payne, R. Conroy, and D. Carnegie, "Achieving sub-millimetre precision with a solid-state full-field heterodyning range imaging camera," *Meas. Sci. Technol.* **18**, 2809–2816 (2007).
73. A. Levin, R. Fergus, F. Durand, and W. T. Freeman, "Image and depth from a conventional camera with a coded aperture," *ACM Trans. Graph.* **26**, 70 (2007).

74. Q. Yang, L. Liu, and J. Sun, "Optimized phase pupil masks for extended depth of field," *Opt. Commun.* **272**, 56–66 (2007).
75. M. Somayaji and M. P. Christensen, "Frequency analysis of the wavefront-coding odd-symmetric quadratic phase mask," *Appl. Opt.* **46**, 216–226 (2007).
76. G. Mikula, Z. Jaroszewicz, A. Kolodziejczyk, K. Petelczyc, and M. Sypek, "Imaging with extended focal depth by means of lenses with radial and angular modulation," *Opt. Express* **15**, 9184–9193 (2007).
77. A. Castro, Y. Frauel, and B. Javidi, "Integral imaging with large depth of field using an asymmetric phase mask," *Opt. Express* **15**, 10266–10273 (2007).
78. E. Garcia-Guerrero, E. R. Mendez, H. M. Escamilla, T. A. Leskova, and A. A. Maradudin, "Design and fabrication of random phase diffusers for extending the depth of focus," *Opt. Express* **15**, 910–923 (2007).
79. G. Mikula, Z. Jaroszewicz, A. Kolodziejczyk, K. Petelczyc, and M. Sypek, "Imaging with extended focal depth by means of lenses with radial and angular modulation," *Opt. Express* **15**, 9184–9193 (2007).
80. N. Caron and Y. Sheng, "Polynomial phase masks for extending the depth of field of a microscope," *Appl. Opt.* **47**, E39–E41 (2008).
81. P. Mouroulis, "Depth of field extension with spherical optics," *Opt. Express* **16**, 12995–13004 (2008).
82. H. Zhao, Q. Li, and H. Feng, "Improved logarithmic phase mask to extend the depth of field of an incoherent imaging system," *Opt. Lett.* **33**, 1171–1173 (2008).
83. S. R. P. Pavan and R. Piestun, "High-efficiency rotating point spread functions," *Opt. Express* **16**, 3484–3489 (2008).
84. J. Ares García, S. Bará, M. Gomez García, Z. Jaroszewicz, A. Kolodziejczyk, and K. Petelczyc, "Imaging with extended focal depth by means of the refractive light sword optical element," *Opt. Express* **16**, 18371–18378 (2008).
85. Y. Takahashi and S. Komatsu, "Optimized free-form phase mask for extension of depth of field in wavefront-coded imaging," *Opt. Lett.* **33**, 1515–1517 (2008).
86. G. Muyo, A. Singh, M. Andersson, D. Huckridge, A. Wood, and A. R. Harvey, "Infrared imaging with a wavefront-coded singlet lens," *Opt. Express* **17**, 21118–21123 (2009).
87. J. Ojeda-Castañeda, A. Sauceda-Carvajal, and J. E. A. Landgrave, "Pseudo zone plate for extended focal depth," *Opt. Mem. Neural Netw.* **18**, 164–170 (2009).
88. F. Zhou, R. Ye, G. Li, H. Zhang, and D. Wang, "Optimized circularly symmetric phase mask to extend the depth of focus," *J. Opt. Soc. Am. A* **26**, 1889–1895 (2009).
89. F. Yan and X. Zhang, "Optimization of an off-axis three-mirror anastigmatic system with wavefront coding technology based on MTF invariance," *Opt. Express* **17**, 16809–16819 (2009).
90. H. Zhao and Y. Li, "Performance of an improved logarithmic phase mask with optimized parameters in a wavefront-coding system," *Appl. Opt.* **49**, 229–238 (2010).
91. R. Horstmeyer, S. B. Oh, and R. Raskar, "Iterative aperture mask design in phase space using a rank constraint," *Opt. Express* **18**, 22545–22555 (2010).
92. S. Bernet and M. Ritsch-Marte, "Optical device with a pair of diffractive optical elements," U.S. patent application 20100134869 A1 (June 3, 2010).
93. J. Ojeda-Castañeda and C. M. Gómez-Sarabia, "Optical processor arrays for controlling focal length or for tuning the depth of field," *Photon. Lett. Poland* **3**, 44–46 (2011).

94. G. Grover, S. Quirin, C. Fiedler, and R. Piestun, "Photon efficient double-helix PSF microscopy with application to 3D photo-activation localization imaging," *Biomed. Opt. Express* **2**, 3010–3020 (2011).
95. S. Quirin, S. R. P. Pavan, and R. Piestun, "Optimal 3D single-molecule localization for superresolution microscopy with aberrations and engineered point spread functions," *Proc. Natl. Acad. Sci. USA* **109**, 675–679 (2011).
96. G. Grover, K. DeLuca, S. Quirin, J. DeLuca, and R. Piestun, "Super-resolution photon-efficient imaging by nanometric double-helix point spread function localization of emitters (SPINDLE)," *Opt. Express* **20**, 26681–26695 (2012).
97. N. Reza and L. N. Hazra, "Toraldo filters with concentric unequal annuli of fixed phase by evolutionary programming," *J. Opt. Soc. Am. A* **30**, 189–195 (2012).
98. G. Haeusler, "Method and microscope device for the deflectometric detection of local gradients and the (continued) three-dimensional shape of an object," U.S. patent 8,224,066 (July 17, 2012).
99. O. Palillero-Sandoval, J. F. Aguilar, and L. R. Berriel-Valdos, "Phase mask coded with the superposition of four Zernike polynomials for extending the depth of field in an imaging system," *Appl. Opt.* **53**, 4033–4038 (2014).
100. Lord Rayleigh, "On the theory of optical images, with special reference to the microscope," *Philos. Mag.* **XLII**, 167–195 (1896).
101. A. Marechal and M. Françon, "Influence des faibles aberrations," in *Difraction structures des images. Influence de la cohérence de la lumière* (Masson & Cie, 1970), pp. 105–142.
102. H. H. Hopkins, "The aberration permissible in optical systems," *Proc. Phys. Soc. B* **70**, 449–470 (1957).
103. W. B. Wetherell, "The calculation of image quality," in *Applied Optics and Optical Engineering*, R. R. Shannon and J. C. Wyant, eds. (Academic, 1980), Vol. 3.
104. J. Ojeda-Castañeda, R. Ramos, and A. Noyola-Isgleas, "High focal depth by apodization and digital restoration," *Appl. Opt.* **27**, 2583–2586 (1988).
105. W. T. Cathey and E. R. Dowski, "New paradigm for imaging systems," *Appl. Opt.* **41**, 6080–6092 (2002).
106. E. H. Adelson and J. Y. A. Wang, "Single lens stereo with plenoptic camera," *IEEE Trans. Pattern Anal. Mach. Intell.* **14**, 99–106 (1992).
107. R. Ng, "Digital light field photography," Ph.D. dissertation (Stanford University, 2006).
108. J. Ojeda-Castañeda, E. Yépez-Vidal, and C. M. Gómez-Sarabia, "Multiple-frame photography for extended depth of field," *Appl. Opt.* **52**, D84–D91 (2013).
109. A. W. Lohmann, "Image formation of dilute arrays for optical information processing," *Opt. Commun.* **86**, 365–370 (1991).
110. A. W. Lohmann, "A fake zoom lens for fractional Fourier experiments," *Opt. Commun.* **115**, 437–443 (1995).
111. S. C. Tucker, W. T. Cathey, and E. R. Dowski, "Extended depth of field and aberration control for inexpensive digital microscope systems," *Opt. Express* **4**, 467–474 (1999).
112. J. van der Gracht, J. Nagy, V. Pauca, and R. Plemmons, "Iterative restoration of wavefront coded imagery for focus invariance," in *Integrated Computational Imaging Systems*, OSA Technical Digest (Optical Society of America, 2001), paper ITuA1.
113. R. Conroy, A. Dorrington, R. Künnemeyer, and M. Cree, "Range imager performance comparison in homodyne and heterodyne operating modes," *Proc. SPIE* **7239**, 723905 (2009).
114. M. Demenikov and A. R. Harvey, "Image artifacts in hybrid imaging systems with a cubic phase mask," *Opt. Express* **18**, 8207–8212 (2010).

115. M. Demenikov and A. R. Harvey, "Parametric blind-deconvolution algorithm to remove image artifacts in hybrid imaging systems," *Opt. Express* **18**, 18035–18040 (2010).
116. M. Larivière-Bastien and S. Thibault, "Limits of imaging-system simplification using cubic mask waveform coding," *Opt. Lett.* **38**, 3830–3833 (2013).
117. M. Demenikov, "Optimization of hybrid imaging systems based on maximization of kurtosis of the restored point spread function," *Opt. Lett.* **36**, 4740–4742 (2011).
118. S. Pal and L. N. Hazra, "Structural design of four component mechanically compensated zoom lenses," *Opt. Eng.* **51**, 063001 (2012).
119. M. Broxton, L. Gosenick, S. Yang, N. Cohen, A. Andelman, K. Deisseroth, and M. Levoy, "Wave optics theory and 3-D deconvolution for the light field microscope," *Opt. Express* **21**, 25418–25439 (2013).
120. K. Marwah, G. Wetzstein, Y. Bando, and R. Raskar, "Compressive light field photography using overcomplete dictionaries and optimized projections," *ACM Trans. Graph.* **32**, 46 (2013).
121. N. Cohen, S. Yang, A. Andelman, M. Broxton, L. Gosenick, K. Deisseroth, M. Horowitz, and M. Levoy, "Enhancing the performance of the light field microscope using wavefront coding," Stanford Computer Graphics Laboratory Tech. Rep. (2014).
122. A. Doblas, S. V. King, N. Patwary, G. Saavedra, M. Martinez-Corral, and C. Preza, "Investigation of the SQUBIC phase mask design for depth-invariant wide field microscopy point spread function engineering," *Proc. SPIE* **8949**, 894914 (2014).
123. P. Jacquinot and B. Roizen-Dossier, "Apodisation," *Prog. Opt.* **3**, 29–186 (1964).
124. W. H. Steel, *Interferometry*, 2nd ed. (Cambridge University, 1986), pp. 234–235.
125. M. Ya Mints and E. D. Prilepskii, "Apodization of a passive optical system with aberrations," *Opt. Spectrosc.* **52**, 538–541 (1982).
126. J. Ojeda-Castañeda, L. R. Berriel-Valdos, and E. Montes, "Bessel annular apodizers: imaging characteristics," *Appl. Opt.* **26**, 2770–2772 (1987).
127. J. Ojeda-Castañeda, E. Tepichín, and A. Díaz, "Arbitrarily high focal depth with a quasioptimum real and positive transmittance apodizers," *Appl. Opt.* **28**, 2666–2670 (1989).
128. J. Ojeda-Castañeda, P. Andres, and A. Diaz, "Annular apodizer for low sensitivity to defocus and to spherical aberration," *Opt. Lett.* **11**, 487–489 (1986).
129. J. Ojeda-Castañeda, J. C. Escalera, and M. J. Yzuel, "Supergaussian rings: focusing properties," *Opt. Commun.* **114**, 189–193 (1995).
130. H. H. Hopkins, "The frequency response of a defocused optical system," *Proc. Phys. Soc.* **231**, 91–103 (1955).
131. M. Subbarao, "Optical transfer function of a diffraction-limited system for polychromatic illumination," *Appl. Opt.* **29**, 554–558 (1990).
132. A. R. FitzGerrell, E. R. Dowski, Jr., and W. T. Cathey, "Defocus transfer function for circularly symmetric pupils," *Appl. Opt.* **36**, 5796–5804 (1997).
133. H. H. Hopkins, "The application of frequency response techniques in optics," in *Proceedings of the Conference on Optical Instrumentation Techniques* (Chapman & Hall 1962), pp. 480–514.
134. P. A. Stokseth, "Properties of a defocused optical system," *J. Opt. Soc. Am.* **59**, 1314–1321 (1969).
135. W. T. Welford, "Use of annular apertures to increase focal depth," *J. Opt. Soc. Am.* **50**, 749–753 (1960).
136. H. F. A. Tschunko, "Imaging performance of annular apertures. 3: Apodization and modulation transfer functions," *Appl. Opt.* **18**, 3770–3774 (1979).

137. C. S. Chung and H. H. Hopkins, "Influence of nonuniform amplitude on the optical transfer function," *Appl. Opt.* **28**, 1244–1250 (1989).
138. K. H. Brenner, A. W. Lohmann, and J. Ojeda-Castañeda, "The ambiguity function as a polar display of the OTF," *Opt. Commun.* **44**, 323–326 (1983).
139. H. Bartelt, J. Ojeda-Castañeda, and E. E. Sicre, "Misfocus tolerance seen by simple inspection of the ambiguity function," *Appl. Opt.* **23**, 2693–2696 (1984).
140. J. Ojeda-Castañeda, L. R. Berriel-Valdos, and E. Montes, "Ambiguity function as a design tool for high focal depth," *Appl. Opt.* **27**, 790–795 (1988).
141. D. S. Barwick, "Efficient metric for pupil-phase engineering," *Appl. Opt.* **46**, 7258–7261 (2007).
142. A. W. Lohmann, J. Ojeda-Castañeda, and N. Streibl, "The influence of wave aberrations on the Wigner distribution," *Opt. Appl.* **13**, 465–471 (1983).
143. D. Zalvidea and E. E. Sicre, "Phase pupil functions for focal depth enhancement derived from a Wigner distribution function," *Appl. Opt.* **37**, 3623–3627 (1998).
144. D. Zalvidea, C. Colautti, and E. E. Sicre, "Quality parameters analysis of optical imaging systems with enhanced focal depth using the Wigner distribution function," *J. Opt. Soc. Am. A* **17**, 867–873 (2000).
145. J. Ville, "Théorie et applications de la notion de signal analytique," *Cables et Transmission* **2**, 61–74 (1948).
146. P. M. Woodward, "The transmitted RADAR signal," in *Probability and Information Theory with Applications to Radar* (McGraw-Hill, 1964), pp. 115–133.
147. E. Wigner, "On the quantum correction for thermodynamic equilibrium," *Phys. Rev.* **40**, 749–759 (1932).
148. A. Papoulis, "Ambiguity function in Fourier optics," *J. Opt Soc. Am.* **64**, 779–788 (1974).
149. K. Dutta and J. W. Goodman, "Reconstruction of images of partially coherent objects from samples of mutual intensity," *J. Opt. Soc. Am.* **67**, 796–803 (1977).
150. J.-P. Guigay, "The ambiguity function in diffraction and isoplanatic imaging by partially coherent beams," *Opt. Commun.* **26**, 136–138 (1978).
151. A. Walther, "Radiometry and coherence," *J. Opt. Soc. Am.* **58**, 1256–1259 (1968).
152. A. Walther, "Propagation of the generalized radiance through lenses," *J. Opt. Soc. Am.* **68**, 1606–1610 (1978).
153. M. J. Bastiaans, "The Wigner distribution function applied to optical signals and systems," *Opt. Commun.* **25**, 26–30 (1978).
154. M. J. Bastiaans, "Wigner distribution function and its applications to first-order optics," *J. Opt. Soc. Am.* **69**, 1710–1716 (1979).
155. H. H. Szu and J. A. Blodgett, "Wigner distribution and ambiguity function," in *Optics in Four Dimensions-1980* (American Institute of Physics, 1980), pp. 355–381.
156. E. Wolf, "New theory of partial coherence in the space-frequency domain. I. Spectra and cross spectra of steady state sources," *J. Opt. Soc. Am.* **72**, 343–351 (1982).
157. M. Testorf and A. W. Lohmann, "Holography in phase space," *Appl. Opt.* **47**, A70–A77 (2008).
158. C. W. McCutchen, "Generalized aperture and the three-dimensional diffraction image," *J. Opt. Soc. Am.* **54**, 240–244 (1964).
159. L. Mertz, *Transformations in Optics* (Wiley, 1965).
160. H. Arsenault and A. Boivin, "An axial form of the sampling theorem and its application to optical diffraction," *J. Appl. Phys.* **38**, 3988–3990 (1967).
161. J. E. A. Landgrave and L. R. Berriel-Valdos, "Sampling expansions for three-dimensional light amplitude distribution in the vicinity of an axial image point," *J. Opt. Soc. Am. A* **14**, 2962–2976 (1997).

162. A. W. Lohmann and J. Ojeda-Castañeda, "Symmetries and periodicities of the Strehl ratio," *Opt. Acta* **31**, 603–610 (1984).
163. J. Ojeda-Castañeda, P. Andrés, and E. Montes, "Phase-space representation of the Strehl ratio: ambiguity function," *J. Opt. Soc. Am. A* **4**, 313–317 (1987).
164. D. Zalvidea, M. Lehman, S. Granieri, and E. E. Sicre, "Analysis of the Strehl ratio using the Wigner distribution function," *Opt. Commun.* **118**, 207–214 (1995).
165. J. Ojeda-Castañeda, P. Andrés, and A. Díaz, "Strehl ratio with low sensitivity to spherical aberration," *J. Opt. Soc. Am. A* **5**, 1233–1236 (1988).
166. J. Ojeda-Castaneda, E. Tepichín, and A. Pons, "Apodization of annular apertures: Strehl ratio," *Appl. Opt.* **27**, 5140–5145 (1988).
167. J. Ojeda-Castaneda and A. Díaz, "High focal depth by quasibifocus," *Appl. Opt.* **27**, 4163–4165 (1988).
168. S. Sanyal and A. Ghosh, "High focal depth with quasi-bifocus birefringent lens," *Appl. Opt.* **39**, 2321–2325 (2000).
169. C. W. McCutchen, "Convolution relation within the three-dimensional diffraction image," *J. Opt. Soc. Am. A* **8**, 868–870 (1991).
170. P. Andrés, M. Martínez-Corral, and J. Ojeda-Castaneda, "Off-axis focal shift for rotationally nonsymmetric screens," *Opt. Lett.* **18**, 1290–1292 (1993).
171. M. Martínez-Corral, P. Andrés, and J. Ojeda-Castaneda, "On-axis diffractional behavior of two-dimensional pupils," *Appl. Opt.* **33**, 2223–2229 (1994).
172. J. Ojeda-Castaneda, M. Martínez-Corral, P. Andrés, and A. Pons, "Strehl ratio vs. defocus for noncentrally obscured pupils," *Appl. Opt.* **33**, 7611–7616 (1994).
173. Q. Gong and S. S. Hsu, "Aberration measurement using axial intensity," *Opt. Eng.* **33**, 1176–1186 (1994).
174. M. Martínez-Corral, P. Andrés, J. Ojeda-Castañeda, and G. Saavedra, "Tunable axial super-resolution by annular binary filters: application to confocal microscopy," *Opt. Commun.* **119**, 491–498 (1995).
175. G. G. Siu, M. Cheng, and L. Cheng, "Design of a phase-filtering mask and an aspherical lens for uniform irradiance and phase on target," *Appl. Opt.* **37**, 1074–1080 (1998).
176. Q. Cao and S. Chi, "Axially symmetric on-axis flat-top beam," *J. Opt. Soc. Am. A* **17**, 447–455 (2000).
177. I. Kitajima, "Improvements in lenses," British patent 250,268 (July 29, 1926).
178. W. T. Plummer, J. G. Baker, and J. van Tassell, "Photographic optical systems with nonrotational aspheric surfaces," *Appl. Opt.* **38**, 3572–3592 (1999).
179. A. W. Lohmann, "Improvements relating to lenses and to variable optical lens systems formed by such lenses," British patent 998,191 (May 29, 1964).
180. A. W. Lohmann, "Lentille de distance focale variable," French patent 1,398,351 (June 10, 1964).
181. A. W. Lohmann, "Lente focale variabile," Italian patent 727,848 (June 19, 1964).
182. A. W. Lohmann, "A new class of varifocal lenses," *Appl. Opt.* **9**, 1669–1671 (1970).
183. L. W. Alvarez, "Two-element variable-power spherical lens," U.S. patent 3,305,294 (Dec. 3, 1964).
184. L. W. Alvarez and W. E. Humphrey, "Variable-power lens and system," U.S. patent 3,507,565 (Apr. 21, 1970).
185. L. W. Alvarez, "Method of forming an optical element of reduced thickness," U.S. patent 3,829,536 (Aug. 13, 1974).
186. L. W. Alvarez, "Development of variable lenses and a new refractor," *J. Am. Optom. Assoc.* **49**, 24–29 (1978).
187. J. G. Baker, "Optical system utilizing a transversely movable plate for focusing," U.S. patent 4,457,592 (July 3, 1984).

188. I. A. Palusinski, J. M. Sasian, and J. E. Greivenkamp, "Lateral-shift variable aberration generators," *Appl. Opt.* **38**, 86–90 (1999).
189. I. M. Barton, S. N. Dixit, L. J. Summers, C. A. Thompson, K. Avicola, and J. Wilhelmsen, "Diffractive Alvarez lens," *Opt. Lett.* **25**, 1–3 (2000).
190. N. López-Gil, H. C. Howland, B. Howland, N. Charman, and R. Applegate, "Generation of third-order spherical and coma aberrations by the use of radially symmetrical fourth-order lenses," *J. Opt. Soc. Am. A* **15**, 2563–2571 (1998).
191. C. Huang, L. Li, E. Allen, and Y. Yi, "Design and fabrication of a micro Alvarez lens array with a variable focal length," *Microsyst. Technol.* **15**, 559–563 (2009).
192. S. Barbero, "The Alvarez and Lohmann refractive lenses revisited," *Opt. Express* **17**, 9376–9390 (2009).
193. C. J. R. Sheppard and Z. S. Hegedus, "Axial behavior of pupil-plane filters," *J. Opt. Soc. Am. A* **5**, 643–647 (1988).
194. C. J. R. Sheppard, "Synthesis of filters for special axial properties," *J. Mod. Opt.* **43**, 525–536 (1996).
195. T. G. Jabbour and S. M. Kuebler, "Axial field shaping under high-numerical-aperture focusing," *Opt. Lett.* **32**, 527–529 (2007).
196. J. A. Davis, C. S. Tuvey, O. López-Coronado, J. Campos, M. J. Yzuel, and C. Iemmi, "Tailoring the depth of focus for optical imaging systems using a Fourier transform approach," *Opt. Lett.* **32**, 844–846 (2007).
197. B. R. Frieden, "The extrapolating pupil, image synthesis, and some thought applications," *Appl. Opt.* **9**, 2489–2496 (1970).
198. J. Ojeda-Castañeda and L. R. Berriel-Valdos, "Arbitrarily high focal depth with finite apertures," *Opt. Lett.* **13**, 183–185 (1988).
199. J. Ojeda-Castañeda and C. M. Gómez, "Plane-wavefronts: novel representations," *Microw. Opt. Technol. Lett.* **7**, 9–12 (1994).
200. J. Ojeda-Castañeda, J. E. A. Landgrave, and H. M. Escamilla, "Annular phase-only mask for high focal depth," *Opt. Lett.* **30**, 1647–1649 (2005).
201. J. Ojeda-Castañeda, S. Ledesma, and C. M. Gómez-Sarabia, "Tunable axial bursts using annularly distributed phase masks," *Photon. Lett. Poland* **4**, 155–157 (2012).
202. J. Dyson, "Circular and spiral diffraction gratings," *Proc. R. Soc. Lond. A* **248**, 93–106 (1958).
203. A. C. S. van Heel, "Modern alignment devices," in *Progress in Optics*, E. Wolf, ed. (Springer-Verlag, 1961), Vol. 1, pp. 289–329.
204. S. Bara-Viñas, Z. Jaroszewicz, A. Kolodziejczyk, and M. Sypek, "Zone plates with black focal spots," *Appl. Opt.* **31**, 192–198 (1992).
205. J. Ojeda-Castañeda, M. Martínez-Corral, and P. Andrés, "Zero axial irradiance by annular screens with angular variation," *Appl. Opt.* **31**, 4600–4602 (1992).
206. J. Ojeda-Castañeda and G. Ramírez, "Zone plates for zero axial irradiance," *Opt. Lett.* **18**, 87–89 (1993).
207. G. Indebetouw, "Optical vortices and their propagation," *J. Mod. Opt.* **40**, 73–87 (1993).
208. A. W. Lohmann, J. Ojeda-Castañeda, and P. Rodríguez-Montero, "Axial irradiance shaping with binary polar curves," *Opt. Commun.* **108**, 42–46 (1994).
209. Z. Jaroszewicz, A. Kolodziejczyk, D. Mouriz, and C. Gomez-Reino, "Spiral zone plates with arbitrary diameter of the dark spot in the centre of their focal point," *Opt. Commun.* **114**, 1–8 (1995).
210. A. W. Lohmann, J. Ojeda-Castañeda, and G. Ramírez, "Zone plates encoding limaçon variations," *Opt. Commun.* **114**, 30–36 (1995).
211. J. Arlt and M. J. Padgett, "Generation of a beam with a dark focus surrounded by regions of higher intensity: the optical bottle beam," *Opt. Lett.* **25**, 191–193 (2000).

212. G. A. Swartzlander, Jr., "Peering into darkness with a vortex spatial filter," *Opt. Lett.* **26**, 497–499 (2001).
213. S. S. R. Oemrawsingh, J. A. W. van Houwelingen, E. R. Eliel, J. P. Woerdman, E. J. K. Verstegen, J. G. Kloosterboer, and G. W. 't Hooft, "Production and characterization of spiral phase plates for optical wavelengths," *Appl. Opt.* **43**, 688–694 (2004).
214. D. Yelin, B. E. Bouma, and G. J. Tearney, "Generating an adjustable three-dimensional dark focus," *Opt. Lett.* **29**, 661–663 (2004).
215. G. Foo, D. M. Palacios, and G. A. Swartzlander, Jr., "Optical vortex coronagraph," *Opt. Lett.* **30**, 3308–3310 (2005).
216. G. A. Swartzlander, Jr., "Achromatic optical vortex lens," *Opt. Lett.* **31**, 2042–2044 (2006).
217. J. Lin, X.-C. Yuan, J. Bu, B. P. S. Ahluwalia, Y. Y. Sun, and R. E. Burge, "Selective generation of high-order optical vortices from a single phase wedge," *Opt. Lett.* **32**, 2927–2929 (2007).
218. A. S. Ostrovsky, C. Rickenstor-Parrao, and V. Arrizon, "Generation of the 'perfect' optical vortex using a liquid-crystal spatial light modulator," *Opt. Lett.* **38**, 534–536 (2013).
219. O. Bryngdahl, "Radial- and circular-fringe interferograms," *J. Opt. Soc. Am.* **63**, 1098–1104 (1973).
220. S. Fürhapter, A. Jesacher, S. Bernet, and M. Ritsch-Marte, "Spiral interferometry," *Opt. Lett.* **30**, 1953–1955 (2005).
221. A. W. Lohmann, "Variable Fresnel zone pattern," *IBM Tech. Disclos. Bull.* **10**, 407–410 (1967).
222. G. L. Rogers and L. C. G. Rogers, "The interrelations between moiré patterns, contour fringes, optical surfaces and their sum and difference effects," *Opt. Acta* **24**, 15–22 (1977).
223. J. M. Burch and D. C. Williams, "Varifocal moiré zone plates for straightness measurement," *Appl. Opt.* **16**, 2445–2450 (1977).
224. A. W. Lohmann and D. P. Paris, "Variable Fresnel zone pattern," *Appl. Opt.* **6**, 1567–1570 (1967).
225. G. Haesler, "A method to increase the depth of focus by two step image processing," *Opt. Commun.* **6**, 38–42 (1972).
226. M. Mino and Y. Okano, "Improvement in the OTF of a defocused optical system through the use of shaded apertures," *Appl. Opt.* **10**, 2219–2225 (1971).
227. J. Ojeda-Castañeda, L. R. Berriel-Valdos, and E. Montes, "Ambiguity function as a design tool for high focal depth," *Appl. Opt.* **27**, 790–795 (1988).
228. E. R. Dowski and T. W. Cathey, "Extended depth of field through wave-front coding," *Appl. Opt.* **34**, 1859–1865 (1995).
229. C. E. Cook and M. Bernfeld, *Radar Signals: An Introduction to Theory and Applications* (Artech House, 1993), pp. 59–108.
230. J. Ojeda-Castañeda, E. Yépez-Vidal, and E. García-Almanza, "Complex amplitude filters for extended depth of field," *Photon. Lett. Poland* **2**, 162–164 (2010).
231. M. J. Bastiaans, "Local frequency description of optical signals and systems," *Research Rep.* (Eindhoven University of Technology, 1988).
232. K. B. Wolf, *Geometric Optics on Phase Space* (Springer, 2004).
233. A. Torre, *Linear Ray and Wave Optics in Phase Space* (Elsevier, 2005).
234. M. Testorf, B. Hennelly, and J. Ojeda-Castañeda, *Phase-Space Optics: Fundamentals and Applications* (McGraw-Hill, 2010).
235. R. J. Marks, J. F. Walkup, and T. F. Krile, "Ambiguity function display: an improved coherent processor," *Appl. Opt.* **16**, 746–750 (1977).
236. H. O. Bartelt, K.-H. Brenner, and A. W. Lohmann, "The Wigner distribution function and its optical production," *Opt. Commun.* **32**, 32–38 (1980).

237. K.-H. Brenner and A. W. Lohmann, "Wigner distribution function display of complex 1-D signals," *Opt. Commun.* **42**, 310–314 (1982).
238. R. Bandler and H. Gluender, "The Wigner distribution function of two-dimensional signals: generation and display," *Opt. Acta* **30**, 1789–1803 (1983).
239. N. Subotic and B. E. A. Saleh, "Generation of the Wigner distribution function of two-dimensional signals by parallel optical processor," *Opt. Lett.* **9**, 471–473 (1984).
240. K. H. Brenner and J. Ojeda-Castañeda, "Ambiguity function and Wigner distribution function applied to partially coherent imagery," *Opt. Acta* **31**, 213–223 (1984).
241. A. Castro, J. Ojeda-Castañeda, and A. W. Lohmann, "Bow-tie effect: differential operator," *Appl. Opt.* **45**, 7878–7884 (2006).
242. A. Castro and J. Ojeda-Castañeda, "Asymmetric phase masks for extended depth of field," *Appl. Opt.* **47**, 1–6 (2004).
243. A. Saucedo-Carvajal and J. Ojeda-Castañeda, "High focal depth with fractional power wavefronts," *Opt. Lett.* **29**, 560–562 (2004).
244. J. Ojeda-Castañeda, S. Ledesma, and C. M. Gómez-Sarabia, "Hyper Gaussian windows with fractional wavefronts," *Phot. Lett. Poland* **5**, 23–25 (2013).
245. H. H. Hopkins, "Wave and ray aberrations," in *Wave Theory of Aberrations* (Oxford, 1950), pp. 12–16.
246. J. Ojeda-Castañeda, J. E. A. Landgrave, and C. M. Gómez-Sarabia, "The use of conjugate phase plates in the analysis of the frequency response of optical systems designed for an extended depth of field," *Appl. Opt.* **47**, E99–E105 (2008).
247. J. Ojeda-Castañeda, E. Aguilera Gómez, H. P. Mora, M. T. Cisneros, E. R. L. Orozco, A. L. Martínez, J. S. P. Santamaría, J. G. M. Castro, and R. C. S. Segoviano, "Optical system with variable field depth," U.S. patent 8,159,573 (April 17, 2012).
248. M. Demenikov, G. Muyo, and A. R. Harvey, "Experimental demonstration of continuously variable optical encoding in a hybrid imaging system," *Opt. Lett.* **35**, 2100–2102 (2010).
249. V. N. Le, S. Chen, and Z. Fan, "Optimized asymmetrical tangent phase mask to obtain defocus invariant modulation transfer function in incoherent imaging systems," *Opt. Lett.* **39**, 2171–2173 (2014).
250. J. Ojeda-Castañeda, M. M. Rodriguez, and R. Naranjo, "Tunable phase masks for extended depth of field," in *Proceedings of Progress in Electromagnetics Research Symposium (PIERS)*, Cambridge Mass., 2010, pp. 5–8.
251. H. Zhao and J. Wei, "Tunable wavefront coded imaging system based on detachable phase mask: Mathematical analysis, optimization and underlying applications," *Opt. Commun.* **326**, 35–42 (2014).
252. J. Ojeda-Castañeda, E. Yépez-Vidal, E. García-Almanza, and C. M. Gómez-Sarabia, "Tunable Gaussian mask for extending the depth of field," *Photon. Lett. Poland* **4**, 115–117 (2012).
253. A. W. Lohmann and J. Ojeda-Castañeda, "Spatial periodicities in partially coherent fields," *Opt. Acta* **30**, 475–479 (1983).
254. W. D. Montgomery, "Self-imaging objects of infinite aperture," *J. Opt. Soc. Am.* **57**, 772–775 (1967).
255. J. Durnin, "Exact solutions for nondiffracting beams. I. The scalar theory," *J. Opt. Soc. Am. A* **4**, 651–654 (1987).
256. J. Ojeda-Castañeda, S. Ledesma, and C. M. Gómez-Sarabia, "Tunable apodizers and tunable focalizers using helical pairs," *Photon. Lett. Poland* **5**, 20–22 (2013).
257. E. Acosta and S. Bará, "Variable aberration generators using rotated Zernike plates," *J. Opt. Soc. Am. A* **22**, 1993–1996 (2005).

258. P. Mouroulis and J. Macdonald, *Geometrical Optics and Optical Design* (Oxford University, 1997), pp. 270–289.
259. G. Smith and D. A. Atchison, *The Eye and Visual Optical Instruments* (Cambridge University, 1997), pp. 263–264.
260. A. D. Clark, *Zoom Lenses*, Vol. 7 of Monographs on Applied Optics (Adam Hilger, 1973), pp. 4–5.
261. C. C. Allen, “Optical objective,” U.S. patent 696,788 (April 1, 1902).
262. E. W. Dowski, S. Tachihara, and R. H. Cormack, “Zoom lenses with wavefront coding,” U.S. patent application 20070247725 A1 (October 25, 2007).
263. J. Ojeda-Castañeda, C. M. Gómez-Sarabia, and S. Ledesma, “Novel zoom systems using a vortex pair,” *Asian J. Phys.* **23**, 415–424 (2014).
264. J. Ojeda-Castañeda, C. M. Gómez-Sarabia, and S. Ledesma, “Compact telephoto objectives with zero Petzval sum using varifocal lenses,” *Asian J. Phys.* **23**, 535–542 (2014).
265. E. I. Betenky, M. H. Kreitzer, and J. Moskovich, “Zoom lenses with short back focal length,” U.S. patent 4,936,661 (June 26, 1990).
266. A. Cox, *Photographic Optics* (Focal, 1974), pp. 264–277.
267. J. W. Hardy, *Adaptive Optics for Astronomical Telescopes* (Oxford University, 1998).
268. G. Rousset, *Adaptive Optics in Astronomy* (Cambridge University, 1999).
269. B. Berge and J. Peseux, “Variable focal lens controlled by an external voltage: an application of electrowetting,” *Eur. Phys. J. E* **3**, 159–163 (2000).
270. H. W. Ren, Y. H. Fan, S. Gauza, and S. T. Wu, “Tunable-focus flat liquid crystal spherical lens,” *Appl. Phys. Lett.* **84**, 4789–4791 (2004).
271. D. Y. Zhang, N. Justis, and Y. H. Lo, “Fluidic adaptive zoom lens with high zoom ratio and widely tunable field of view,” *Opt. Commun.* **249**, 175–182 (2005).
272. B. H. W. Hendriks, S. Kuiper, M. A. J. Van As, C. A. Renders, and T. W. Tukker, “Electrowetting-based variable-focus lens for miniature systems,” *Opt. Rev.* **12**, 255–259 (2005).
273. F. S. Tsai, S. H. Cho, Y. H. Lo, B. Vasko, and J. Vasko, “Miniaturized universal imaging device using fluidic lens,” *Opt. Lett.* **33**, 291–293 (2008).
274. M. Duocastella, B. Sun, and C. B. Arnold, “Simultaneous imaging of multiple focal planes for three dimensional microscopy using ultra-high-speed adaptive optics,” *J. Biomed. Opt.* **17**, 050505 (2012).
275. M. Duocastella and C. B. Arnold, “Enhanced depth of field laser processing using an ultra-high-speed axial scanner,” *Appl. Phys. Lett.* **102**, 061113 (2013).
276. T. Martinez, D. V. Wick, D. M. Payne, J. T. Baker, and S. R. Restaino, “Non-mechanical zoom system,” *Proc. SPIE* **5234**, 375–378 (2004).
277. Z. Wang, Y. Xu, and Y. Zhao, “Aberration analyses for liquid zooming lenses without moving parts,” *Opt. Commun.* **275**, 22–26 (2007).
278. A. Mikš and J. Novák, “Analysis of two-element zoom systems based on variable power lenses,” *Opt. Express* **18**, 6797–6810 (2010).
279. A. Mikš and J. Novák, “Three-component double conjugate zoom lens system from tunable focus lenses,” *Appl. Opt.* **52**, 862–865 (2013).
280. A. Mikš and J. Novák, “Paraxial imaging properties of double conjugate zoom lens system composed of three tunable-focus lenses,” *Opt. Lasers Eng.* **53**, 86–89 (2014).
281. J. Ojeda-Castañeda, C. M. Gómez-Sarabia, and S. Ledesma, “Novel free-form optical pairs for tunable focalizers,” *J. Opt.* **43**, 85–91 (2014), Springer-Verlag.
282. K. Khare, “PSF engineering,” in *Fourier Optics and Computational Imaging* (Wiley, 2016), Chap. 7.
283. J. Ojeda-Castañeda, A. L. Barragán-Chávez, and C. M. Gómez-Sarabia, “Aberration generators in tandem,” *Photon. Lett. Poland* **7**, 8–10 (2015).



**Jorge Ojeda-Castañeda**, Ph.D. (Applied Optics), J. J. Thomson Lab, University of Reading, United Kingdom (1976); Supervisor H. H. Hopkins, Rumford Laureate M. Sc. Management of Technology, M.I.T. (2002); B. Sc. National Autonomous University of Mexico (1972). Jorge has written more than 155 papers in peer-reviewed academic journals and more than 100 papers in conference proceedings. He is a member of the editorial boards of the Journal of Optics (Optical Society of India), Microwave and Optical Technology Letters (John Wiley), and Optical Memory and Neural Networks (Allerton Press). He has co-edited the following books: *Phase-Space Optics: Fundamentals and Applications*, McGraw-Hill, 2010; Milestone volumes 128 (*Zone Plates*) and 181 (*Phase-Space Optics*), SPIE; the special issue on Phase-Space Optics in *Applied Optics* (August 1, 2008); SPIE Proceedings Vol. 8833, from the tribute meeting to H. J. Caulfield (October, 2013); and SPIE Proceedings Vol. 9142, Conference on Photo-Electronic Technology. Jorge is a Fellow member of the Optical Society of India (OSI, 2006), The Optical Society (OSA, 1993), the Society of Photo-Instrumentation Engineers (SPIE, 1991), the Alexander von Humboldt Foundation (1982-1984, 2004), The Electromagnetism Academy (MIT, 1989), and the Mexican Academy of Science (1985). He has served as General Director, Instituto Nacional de Astrofísica, Óptica y Electrónica México (1984-1988, 1988-1992); Vice President of the International Commission for Optics, affiliated to the IUPAP (1996-1999, 1999-2002); and Dean of the School of Science, Universidad de las Americas, Puebla, Mexico (1996-2001). Currently, he is Full Professor at the University of Guanajuato, Mexico.



**Cristina Margarita Gómez-Sarabia**, Ph.D. Instituto Nacional de Astrofísica, Óptica y Electrónica (INAOE), México (1998); M. Sc. INAOE, México (1994); B. Sc. National Autonomous University of Puebla, México (1992). Cristina Margarita has contributed in more than 30 papers in peer-reviewed academic journals. She has taught several courses in physics and mathematics for undergraduates, and she is currently a Full Professor in the Digital Arts and Business Department at the University of Guanajuato, Campus Irapuato-Salamanca, Mexico.